The effect of AC magnetic fields on liquid-metal free surfaces in industrial MHD.

A thesis

submitted in fulfilment

of the requirements for the Degree

of

Doctor of Philosophy

at the

University of Waikato

by

K. J. Spragg

THE UNIVERSITY OF
WAIKATO
Te Whare Wānanga o Waikato

University of Waikato

2009

Abstract

In this thesis we investigate free-surface instabilities which occur in various industrial processes involving liquid metal. Specifically, we examine a number of simple problems with a view to developing a plausible theoretical description based on MHD. Of particular interest is the behaviour of the free surface of a pool of liquid metal when it is submitted to an alternating magnetic field.

The first problem we examine considers the effect of a low-frequency magnetic field on a pool of liquid metal. An initially circular pool is deformed into radially oscillating "starfish" modes at certain critical magnetic field strengths. We study these azimuthal modes theoretically by investigating the behaviour of an isolated mode. We also consider the influence of geometry in our studies of a related problem invloving a rectangular "strip" of liquid metal. At certain critical magnetic field strengths, an elongated pool is deformed into transverse modes. Aside from complicated mode coupling, the behaviour of these transverse modes is similar to the "starfish". Both the "starfish" and transverse modes are caused by a Mathieu-type subharmonic instability.

We next consider the effect of a medium-frequency magnetic field on an initially circular pool of liquid metal. Experimentally we study the effect of a vertical alternating medium-frequency magnetic field on an initially circular pool. We observe two types of behaviour: slow radial oscillation of the pool perimeter and rotation of the pool about its centre. The physics of this problem are significantly more complicated than the "starfish" and "strip" problems. Accordingly a description in terms of the previous theory is not possible.

The final problem we consider is the effect of a high-frequency magnetic field the surface of a conductor. Using a phase-field approach we consider two simple problems: the first is to calculate the rest shape of an infinite strip of liquid resting on a substrate in a vertical gravitational field; the second is to calculate the equilibrium shape of the cross-section of a column of a liquid conductor submitted to a high-frequency magnetic field whose field lines are parallel far from the conductor. Our numeric solutions compare well with previously known analytic solutions.

Acknowledgements

I would like to thank Prof. Alfred Sneyd for his guidance and friendship throughout my doctoral work. I also wish to thank Prof. Yves Fautrelle for his help and patience. His help and support were of great assistance during various difficult periods of my stay in France.

I wish to thank both my second supervisor Prof. Ian Craig and Dr Yuri Litvinenko for the time and effort they invested in proof reading my thesis manuscript.

I have been fortunate in that I have been able to work in two countries: New Zealand and France. Without financial support from the University of Waikato, EGIDE, EPM-SIMAP and NZIMA this would not have been possible.

Finally I wish to thank the entire EPM-SIMAP team for welcoming me into their laboratory where I worked in France.

Contents

List of Tables

List of Figures

Chapter I

Resume de thése

Plan de these

1. Introduction
2. Le problème de « l'étoile de mer »
3. Expériences sur une bande de métal liquide sous champ magnétique basse fréquence
4. Théorie de la stabilité de la bande mince
5. Expériences sur des gouttes sous champ magnétique à moyenne fréquence
6. Méthode du champ de phase appliquée au calcul des déformations de surfaces libres
7. Conclusions

Chapitre 1 - Introduction

En métallurgie d'élaboration des matériaux à l'état liquide, la surface libre du métal liquide a une grande importance pratique. C'est là que se produisent les réactions d'oxydation conduisant à l'apparition d'inclusions dans le métal liquide, ce qui constitue un défaut majeur pour le matériau. D'autre part, la surface libre est aussi le lieu où sont réalisées diverses opérations métallurgiques telles que l'addition d'éléments pour constituer l'alliage (« la mise à la nuance »), l'affinage consistant à éliminer les éléments indésirables comme le soufre, l'oxygène dans l'acier liquide. La surface libre est très souvent sujette à des instabilités. Celles-ci sont indésirables lorsqu'elles favorisent l'oxydation de la surface libre. Par contre, elles peuvent être bénéfiques en accélérant les réactions de surface d'affinage. Les problèmes de surface libre en métallurgie se rencontrent dans les procédés à induction mettant en jeu des métaux liquides comme l'acier, l'aluminium le cuivre. Les procédés utilisent les forces électromagnétiques pour agiter le métal liquide. Les forces électromagnétiques

agissent aussi sur la surface libre de différentes façons selon la fréquence des courants inducteurs.

Les forces électromagnétiques peuvent déformer la surface libre d'une manière statique pour créer les dômes de surface que l'on observe dans les fours à induction ou léviter une boule de métal liquide. Ces cas correspondent aux situations où la fréquence du champ magnétique est assez élevée. Les champs magnétiques à moyenne ou haute fréquence peuvent être utilisés pour contrôler les formes de surface libre, par exemple les jets ou la lévitation d'une boule de métal liquide. Cependant par exemple dans le cas de la lévitation, lorsque l'on cherche à léviter des masses importantes en augmentant l'intensité du champ magnétique de nombreuses in stabilités de surface apparaissent, ce qui empêche le développement de tels procédés.

Lorsque la fréquence du champ magnétique appliqué est basse, la partie oscillante des forces électromagnétiques devient prépondérante. Dans ce cas le liquide et sa surface libre sont soumis à une force oscillante. Il en résulte une agitation de surface lorsque les forces excitent par effet de résonance les modes propres d'oscillation de la surface libre. Il s'agit d'un problème original d'agitation électromagnétique de surface libre. Le couplage entre écoulement et courants induits est aussi fort. Ce phénomène peut être mis à profit pour accélérer les réactions de transfert aux interfaces.

La compréhension et la modélisation de ces phénomènes sont très complexes. En effet, les courants électriques induits dans la charge sont fortement modifiés par les déformations de surface libre du domaine liquide, ce qui rend le couplage très fort. De nombreuses études ont été réalisées jusque là. Cependant l'analyse des instabilités demeure toujours un problème non résolu. Ceci fait l'objet de la présente thèse.

Le mémoire comprend cinq chapitres outre l'introduction et la conclusion. Le Chapitre 2 traite des effets des champs magnétiques oscillant à basse fréquence sur une goutte de métal liquide circulaire. L'objectif de ce chapitre est d'analyser

théoriquement les oscillations de surface observées auparavant. Un modèle heuristique est développé à partir d'une méthode originale basée sur une approche Lagrangienne. Les Chapitres 3 et 4 reprennent le même cas des basses fréquences mais dans une géométrie plus simple, celle d'une bande de métal liquide. Le modèle est confronté à des expériences que nous avons réalisées. Le chapitre 5 est consacré à l'analyse du cas des fréquences élevées pour une géométrie de goutte circulaire de métal liquide. Ce cas est beaucoup plus complexe car le champ magnétique inducteur est significativement modifié par la présence de la charge. Nous avons choisi de réaliser des expériences montrant les diverses instabilités de morphologie qui se produisent. Enfin le Chapitre 6 est consacré à une première approche pour modéliser les déformations de surface dans la configuration de fréquence élevée. Il s'agit de mettre en œuvre une approche originale en transposant les méthodes dites de champ de phase à la présente situation.

Chapitre 2 - le Problème de « l'étoile de mer » - modèle mathématique

Ce chapitre est consacré à l'analyse des effets d'un champ magnétique oscillant à basse fréquence (quelques Hertz) sur une goutte circulaire de métal liquide posée sur un substrat. Lorsque l'on applique un champ magnétique oscillant à très basse fréquence sur un volume de métal liquide, la goutte est sujette à des oscillations de surface. Ces oscillations ont été déjà observées expérimentalement dans des travaux antérieurs. Elles comportent deux types d'oscillations: des ondes directement forcées et des oscillations résultant d'instabilités de type paramétrique de fréquence égale à la moitié de celles des forces électromagnétiques. Ces instabilités se présentent sous la forme d'ondes stationnaires azimutales, d'où le nom d'instabilité en étoile de mer. Ceci est illustré dans la figure I.1.

L'approche choisie consiste à élaborer un modèle heuristique permettant

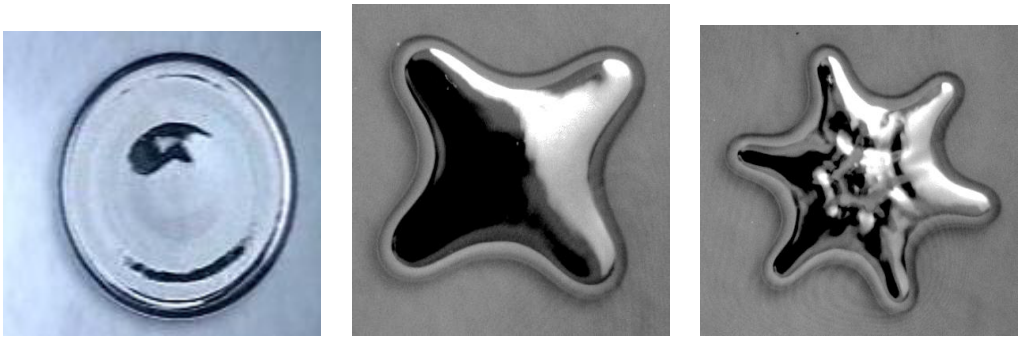

(a) régime axisymétrique, mercure $f = 1,354$ Hz, $B_0 = 0,1105$ T.

(b) mode 4, mercure $f = 1,2$ Hz, $B_0 = 0,2210$ T.

(c) mode 6, mercure $f = 2,10$ Hz, $B_0 = 0.153$ T.

Figure I.1: Illustration des formes de gouttes oscillantes sous champ magnétique très basse fréquence.

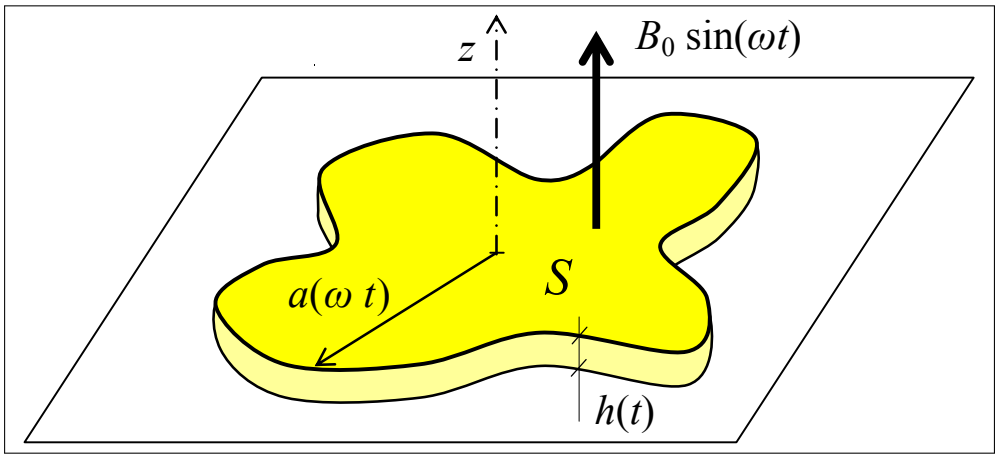

Figure I.2: Illustration de la géométrie simplifiée du modèle

de comprendre les phénomènes observés expérimentalement. La géométrie du modèle est illustrée dans la figure I.2. Nous avons choisi une approche Lagrangienne. Cette méthodologie est envisageable car dans le cas des très basses fréquences la force électromagnétique dérive d'un potentiel scalaire. Il est donc possible de construire une fonction représentant l'énergie potentielle E_{em} des forces électromagnétiques. Les autres forces dérivent aussi de potentiels scalaires représentant les différentes énergies du système: par exemple l'énergie de gravité E_g, l'énergie de surface E_s et l'énergie cinétique E_k. Les paramètres à déterminer sont les amplitudes des modes d'oscillation. Dans le cas présent, nous avons choisi un modèle à deux modes, à savoir l'épaisseur de

la goutte $h(t)$ et l'amplitude $a_m(t)$ des perturbations du rayon $a(t)$ de la goutte pour un seul mode azimutal noté m (illustration en figure I.1(b) et I.1(c)). En supposant que l'écoulement de la goutte est à potentiel, il est possible d'établir une expression analytique de l'écoulement. Alors on peut calculer toutes les énergies et construire une fonction de Lagrange $L(h, \dot{h}, a_m, \dot{a}_m)$ comme suit:

$$L(h, \dot{h}, a_m, \dot{a}_m) = E_k - E_s - E_g - E_{em} \tag{I.1}$$

On obtient alors deux équations de Lagrange:

$$\frac{d}{dt}\frac{\partial L}{\partial \dot{h}} - \frac{\partial L}{\partial h} = 0 \qquad \text{et:} \qquad \frac{d}{dt}\frac{\partial L}{\partial \dot{a}_m} - \frac{\partial L}{\partial a_m} = 0. \tag{I.2}$$

Ce sont deux équations différentielles ordinaires non-linéaires régissant les variables hauteur $h(t)$ et l'amplitude des perturbations $a_m(t)$. Les deux équations sont détaillées en (2.35) et (2.35) dans le texte principal. Ces deux équations ont été résolues par une méthode de Runge-Kutta 4. Les seuils d'instabilités ont été déterminés par une méthode de bisection.

L'analyse de ce système est réalisée en deux temps. Tout d'abord en dessous du seuil d' instabilité, l'amplitude de la perturbation est nulle et le système se réduit à une équation différentielle gouvernant la hauteur $h(t)$, la goutte restant de forme axisymétrique (cf. figure I.1(a)). C'est une équation de pendule non-linéaire forcée par la force électromagnétique oscillant à la fréquence $2f$ double de celle du champ magnétique. L'évolution temporelle est illustrée dans la figure 2.3 du texte principal. Ce comportement est observé dans les expériences.

Lorsque l'amplitude du champ magnétique dépasse un certain seuil, les expériences montrent qu'une instabilité azimutale se déclanche, montrant l'apparition de mode azimutal dont la valeur de m dépend de la fréquence (cf. figures I.1(b), I.1(c)). Ce mode oscille à la fréquence f, soit la moitié de celle des forces électromagnétiques. Ce comportement est typique de l'instabilité dite paramétrique. Le présent modèle mathématique prédit le même comporte-

ment. La frontière de stabilité dans l'espace des paramètres (B_0, f) est constituée de «langues» d'instabilité centrée autour des fréquences propres des modes libres d'oscillation de la surface libre (cf. figures 2.4 à 2.6 du texte principal). Le modèle permet de retrouver tout au moins qualitativement les phénomènes observés dans les expériences.

Chapitre 3 - Expériences sur une bande de métal liquide sous champ magnétique basse fréquence

Ce chapitre est consacré à la réalisation d'expériences consistant à analyser les oscillations d'une goutte de métal liquide placée dans un champ magnétique alternatif à très basse fréquence. Cette partie est complémentaire du chapitre précédent. Dans le cas présent la géométrie est plus simple en principe puisqu'elle est constituée par une bande de liquide. C'est une tentative pour réaliser un problème bidimensionel. La goutte a pour masse 120g de l'alliage eutectique Ga-In-Sn, ce qui correspond à une dimension de 120mm par 30mm environ. Les mesures consistent à filmer les mouvements de la goutte et à réaliser les traitements des images. Le traitement nous avons réalisé un logiciel de capture dynamique de l'interface. Les images ainsi capturées sont analysées en terme de détermination des modes doscillations par analyse spatiale de Fourier. Un exemple est fourni dans les figures 3.4.2 et 3.4.3 du texte principale.

La figure I.3 illustre les morphologies de surfaces libres observées. Ceci est détaillé dans les figures 3.7 à 3.14 dans le texte principal. On observe deux types de mode: les modes «sinueux» et «variqueux». La surface libre comporte des modes dont la longueur d'onde dépend de la fréquence. Comme dans le cas de la goutte circulaire, les observations montrent que, lorsque l'on augmente le champ magnétique pour une fréquence fixée, il se produit les phénomènes suivants:

- champ magnétique faible: la goutte oscille de manière symétrique par rapport à son grand axe avec une fréquence $2f$. Ce sont des oscillations forcées directement par les forces électromagnétiques.

- champ magnétique modéré: il apparaît une instabilité conduisant à l'apparition de modes non-symétriques oscillant à la fréquence f. Ces modes sont le résultat d'une instabilité de type paramétrique.

- champ magnétique fort: les formes de surface libre deviennent déstructurées et chaotiques.

Les frontières de stabilité dans le plan de phase (B_0, f) sont montrées dans les figures 3.16 et 3.17 du texte principale. Elles se composent de langues d'instabilités centrées sur les fréquences propres des modes libres d'oscillation de la surface libre. Ceci confirme la nature paramétrique de l'instabilité.

Chapitre 4. Théorie de la stabilité de la bande mince

Ce chapitre est consacré à l'analyse des effets d'un champ magnétique oscillant à basse fréquence (quelques Hertz) sur une goutte allongée de métal liquide, une bande mince, posée sur un substrat. Nous reprenons la théorie utilisée dans le chapitre 2 pour la transposer sur le cas d'une goutte infiniment allongée. Lorsque l'on applique un champ magnétique oscillant à très basse fréquence sur un volume de métal liquide, la goutte est sujette à des oscillations de surface. Ces oscillations ont été mises en évidence expérimentalement dans le chapitre 3 précèdent.

L'approche choisie consiste à élaborer un modèle heuristique permettant de comprendre les phénomènes observés expérimentalement. La géométrie du modèle est illustrée dans la figure I.4 ci-dessous. Notons que comme dans les expériences, il existe deux types de mode: les modes sinueux et variqueux.

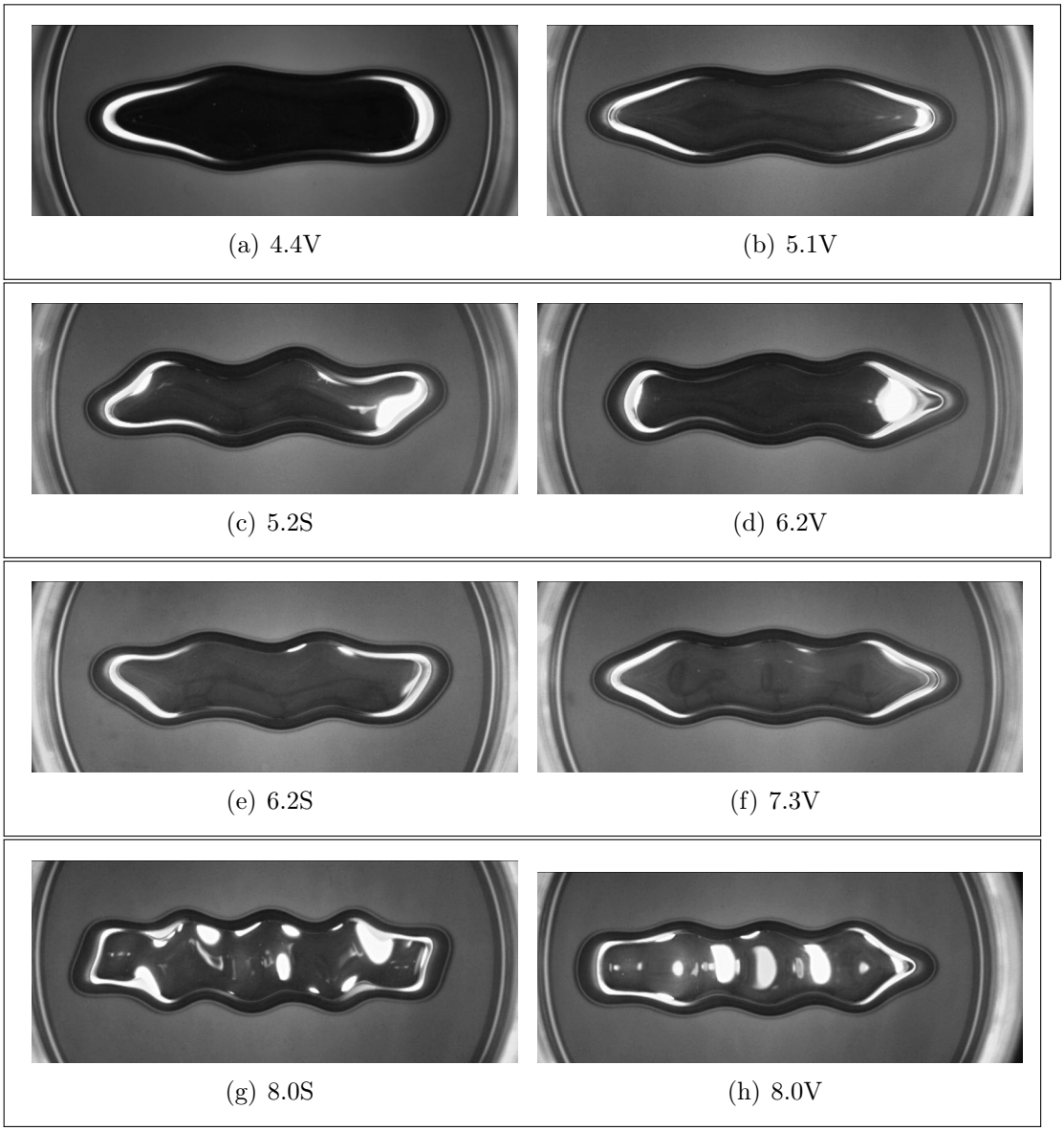

(a) 4.4V (b) 5.1V

(c) 5.2S (d) 6.2V

(e) 6.2S (f) 7.3V

(g) 8.0S (h) 8.0V

Figure I.3: Vue de la surface libre expérimentale d'une goutte d'alliage de gallium pour diverses fréquence du champ magnétique appliqué, entre 1,7 et 4Hz. Le champ magnétique a pour amplitude 0,1T environ ce qui est suffisant pour se placer dans le régime paramétrique.

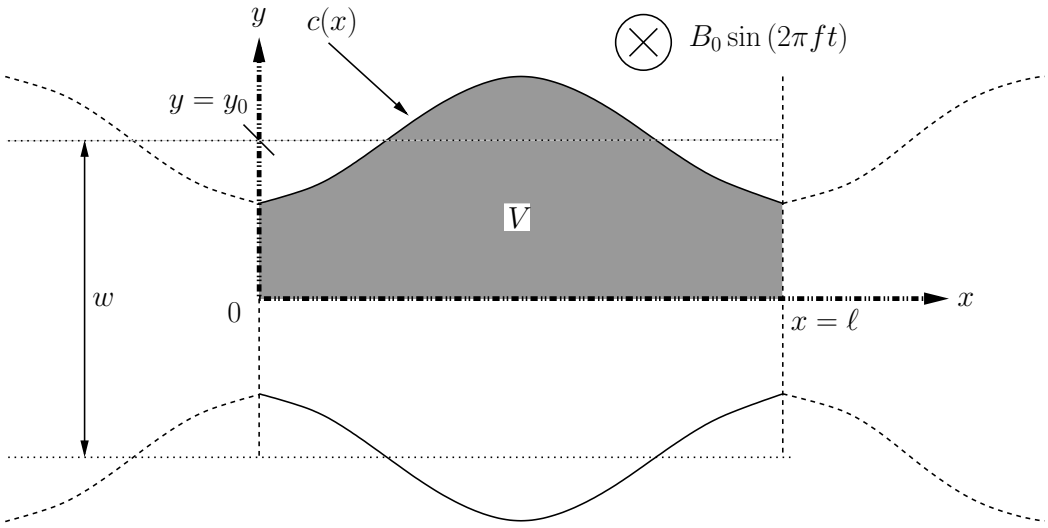

(a) Vue de dessus

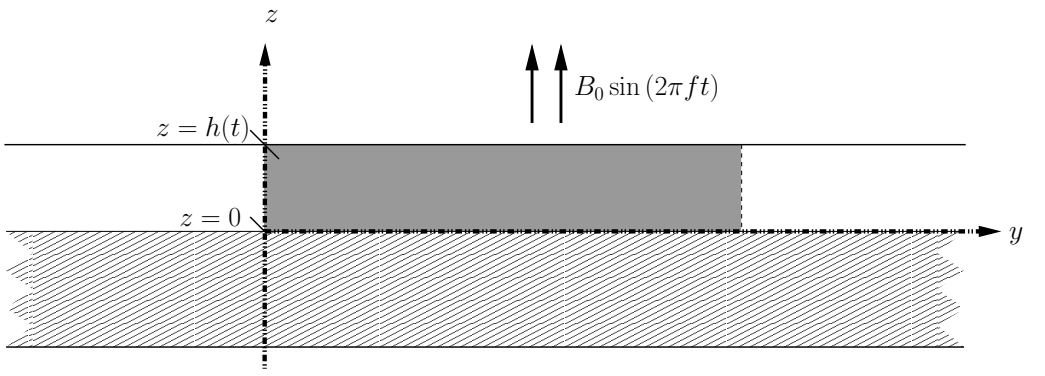

(b) Vue en coupe latérale

Figure I.4: schéma de la géométrie simplifiée du modèle. La configuration illustrée est celle du mode sinueux.

La démarche utilisée est identique à celle du chapitre 2. On peut décrire le problème par deux paramètres inconnus du problème qui sont la hauteur de la surface $h(t)$ ainsi que l'amplitude de la perturbation $b(t)$ de la largeur de la bande $c(x)$. Nous avons choisi aussi une approche Lagrangienne. De la même façon pour une longueur d'onde donnée, on peut calculer toutes les énergies et construire une fonction de Lagrange $L(h, \dot{h}, a_m, \dot{a}_m)$ comme suit:

$$L(h, \dot{h}, b, \dot{b}) = E_k - E_s - E_g - E_{em}. \tag{I.3}$$

On obtient alors deux équations de Lagrange:

$$\frac{d}{dt}\frac{\partial L}{\partial \dot{h}} - \frac{\partial L}{\partial h} = 0 \qquad \text{et:} \qquad \frac{d}{dt}\frac{\partial L}{\partial \dot{b}} - \frac{\partial L}{\partial b} = 0. \tag{I.4}$$

Ce sont deux équations différentielles ordinaires non-linéaires régissant les variables hauteur $h(t)$ et l'amplitude des perturbations $b(t)$. Les deux équations sont détaillées en (4.43) par exemple dans le texte principal. Ces deux équations ont été résolues par une méthode de Runge-Kutta 4. Les seuils d'instabilités ont été déterminés par une méthode de bisection.

Le comportement des deux équations est semblable à celui obtenu dans le cas de la goutte circulaire. L'équation pour $h(t)$ est celle d'un pendule non-linéaire forcée par la force électromagnétique oscillant à la fréquence $2f$ double de celle du champ magnétique. En ce qui concerne l'équation régissant $b(t)$, lorsque l'amplitude du champ magnétique dépasse un certain seuil, le modèle montre qu'une instabilité azimutale se déclanche, montrant l'apparition de mode azimutal dont la valeur de m dépend de la fréquence. Ce mode oscille à la fréquence f, soit la moitié de celle des forces électromagnétiques. Ce comportement est typique de l'instabilité dite paramétrique. Le présent modèle mathématique prédit le même comportement que celui observé dans les expériences du chapitre 3.

La frontière de stabilité calculée par le modèle dans l'espace des paramètres (B_0, f) est constituée de «langues» d'instabilité centrée autour des fréquences

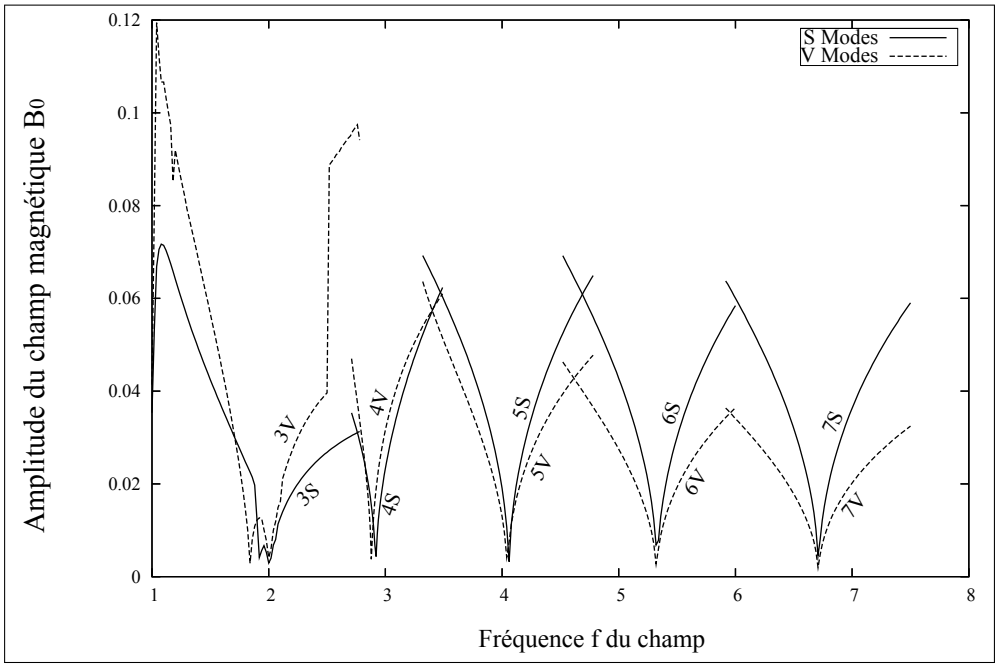

Figure I.5: diagramme de stabilité calculé par le modèle pour les deux types de mode (S = sinueux, V = variqueux) dans les plan de phase des paramètres amplitude du champ magnétique B_0 et sa fréquence f.

propres des modes libres d'oscillation de la surface libre. Les résultats du modèle sont illustrés par la figure I.5 ci-dessous (les détails sont fournis dans les figures 4.5 à 4.10 du texte principal). Le modèle permet de retrouver tout au moins qualitativement les phénomènes observés dans les expériences. Il est à noter que les résultats du modèle dans cette configuration sont en concordance avec les expériences que dans le cas de la goutte circulaire. Ceci a été attribué aux effets d'extrémité qui sont présent pour la bande mince. L'hypothèse de la goutte infiniment longue est sans doute trop restrictive.

Chapitre 5. Expériences sur des gouttes sous champ magnétique à moyenne fréquence

Ce chapitre est consacré à l'étude expérimentale de l'effet d'un champ de fréquence élevée sur une goutte de métal liquide. Cette configuration est proche de celle de la lévitation électromagnétique. L'effet de sustentation est

dans le cas présent réalisé par le contact avec le substrat. Cependant, comme on le montrera, cette configuration fait apparaître des instabilités originales observées aussi en lévitation.

Le problème consiste à placer une goutte de métal liquide (alliage ternaire eutectique Ga-In-Sn) posée sur un substrat dans l'entrefer d'une bobine alimentée par des courants alternatifs à moyenne fréquence $f = 7.8$ kHz. La géométrie est illustrée dans la figure I.6 ci-dessous. Le problème est très complexe car, contrairement au cas des basses fréquences, le champ magnétique inducteur est fortement modifié par la présence de la goutte. Celui-ci tend à être expulsé de la charge pour être confiné dans la peau électromagnétique δ d'épaisseur telle que

$$\delta = \left(\frac{1}{\pi \mu_0 \sigma f} \right)^{1/2}, \tag{I.5}$$

μ_0, σ et f désignant respectivement la perméabilité du vide, la conductivité électrique de la goutte et la fréquence du champ magnétique. Lorsque l'on utilise l'alliage de gallium, l'épaisseur de peau électromagnétique à la fréquence de travail de 7,8 kHz est égale à 3mm, ce qui est comparable à l'épaisseur de la goutte de 6mm environ.

L'installation expérimentale est illustrée dans les figures 5.1, 5.2 et 5.3 du texte principal. Elle est constituée par une cuve entourée par une enveloppe refroidie par de l'eau pour évacuer la chaleur dissipée par effet Joule dans la goutte (1kW environ). L'oxydation de la goutte est minimisée en immergeant la goutte dans une solution d'eau acidifiée par HCl. Le volume de la goutte varie entre 5 et 10 ml, ce qui correspond à des diamètres de l'ordre de 40 mm environ. Les mesures consistent à augmenter le champ magnétique par palier de 0 jusqu'au maximum possible compatible avec le refroidissement de la goutte, soit 110mT environ. La fréquence du champ magnétique est fixée à 7,8 kHz. Le paramètre sans dimension pertinent dans ce problème est le nombre de Bond magnétique B_m défini comme le rapport entre les forces élec-

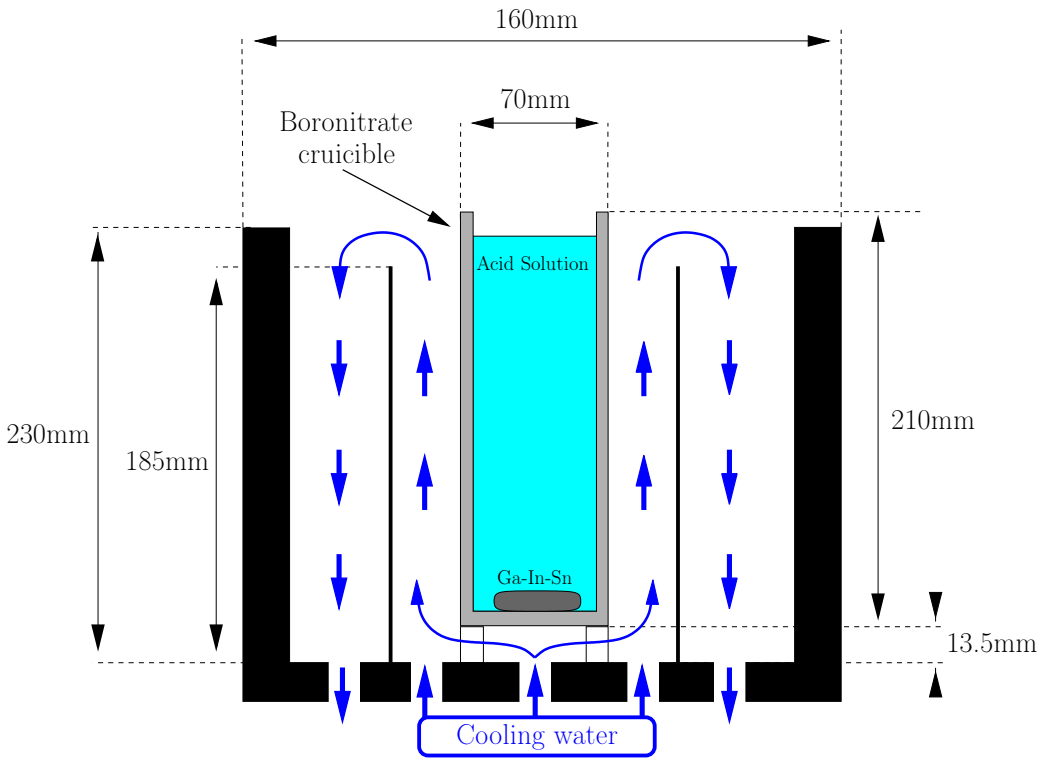

Figure I.6: schéma de l'installation utilisée montrant la goutte d'alliage de gallium immergée dans une solution eau+acide. L'ensemble est entouré par un inducteur alimenté en courant moyenne fréquence

tromagnétiques et les forces capillaires, soit

$$B_m = \frac{aB_0^2}{\mu_0 \gamma} \tag{I.6}$$

a, γ désignant respectivement le rayon de la goutte et sa tension interfaciale.

Les observations sont illustrées dans les figues 5.5 à 5.20 du texte principal. Elles montrent que:

- pour des champs magnétiques faibles (faible nombre de Bond magnétique) la goutte se déforme de manière statique en restant axisymétrique. Il se produit un léger effet de dôme observé fréquemment dans les poches à induction.

- lorsque l'on augmente l'amplitude du champ magnétique (ou le nombre de Bond), il apparaît sur la périphérie de la goutte des ondulations de faible amplitude.

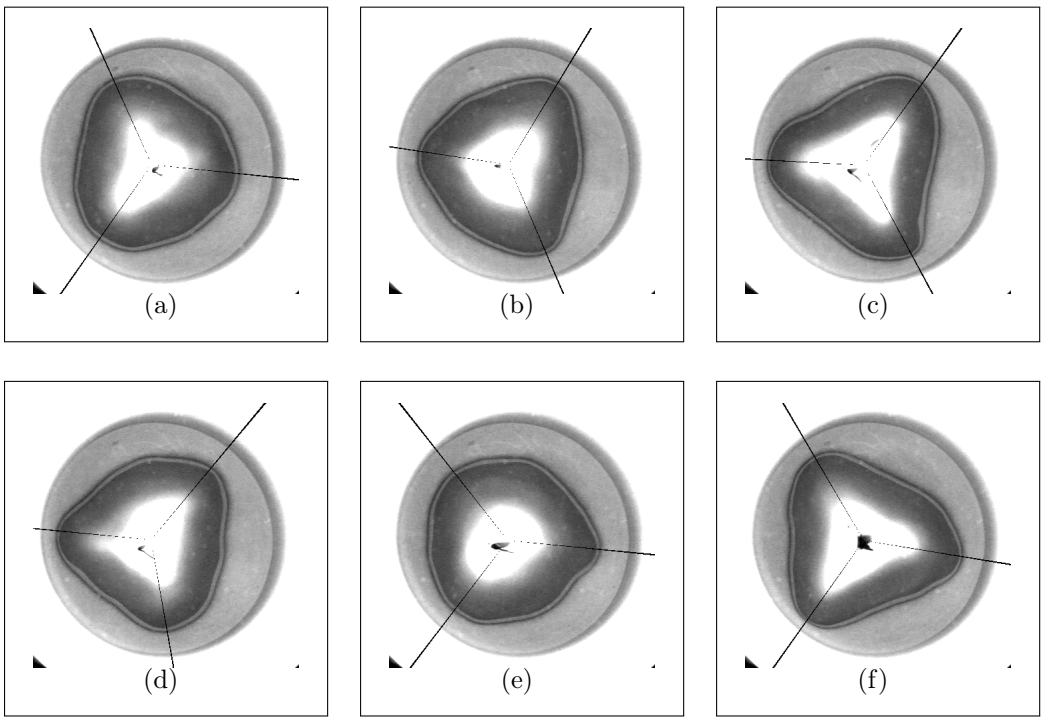

Figure I.7: Morphologie des instabilités de surface: oscillations en rotation du mode 3 pour une goutte de 10ml, nombre de Bond magnétique $B_m = 50{,}2$. Séquences enregistrées à des intervalles de 0.075s

- A partir d'un seuil de nombre de Bond critique, la goutte prend une forme elliptique (mode 2) puis triangulaire (mode 3). Elle oscille radialement à une fréquence autour de 2Hz. Le nombre de Bond critique dépend du mode excité (cf. Tableau 5.1 du texte principal).

- Au-delà du seuil, la goutte est soumise à un mouvement de rotation rapide à une fréquence angulaire autour de 6 à 10rad/s. Il est étonnant de constater que la rotation s'effectue dans les deux sens changeant de manière aléatoire.

Un exemple de résultat est montré dans la figure I.7.

Chapitre 6. Méthode du champ de phase appliquée au calcul des déformations de surfaces libres

Ce chapitre est dédié à l'analyse théorique des phénomènes mis en évidence dans le Chapitre 5 précédent. L'objectif consiste à développer une méthode numérique capable de modéliser le comportement d'une goutte dont la surface libre subit de grandes déformations. Il s'agit d'un problème très difficile en raison du couplage très fort entre le champ magnétique imposé et l'établissement des courants électriques induits et la déformation de surface qui les perturbe. Il existe différentes méthodes pour traiter les problèmes d surfaces libres, tels les méthodes Volume of Fluid (VOF), suivi d'interface (Front Tracking), Arbitrarian Lagrangian-Eulerian (ALE), LEVEL SET, Champ de Phase (Phase Field). Parmi les différentes méthodes de traitement d'un tel problème, nous avons la dernière, à savoir la méthode du champ de phase. Cette méthode est plus complexe que les autres sur le fond car elle résulte d'un principe de minimisation d'une fonctionnelle d'énergie. Cependant elle permet de traiter des cas de surface libre très déformée. La formulation utilisée est celle d'Allen and Cahn [1979].

L'application de la méthode consiste à définir une fonction de phase $\psi(\mathbf{x}, t)$ dont la valeur est comprise entre -1 et $+1$ (par exemple), soit

$\psi(\mathbf{x}, t) = +1$ dans le métal liquide,

$\psi(\mathbf{x}, t) = -1$dans les régions isolantes électriquement.

Ceci est illustré dans la figure I.8 ci-dessous. L'équation pour $\psi(\mathbf{x}, t)$ est obtenue à partir de la minimisation d'une fonctionnelle de l'énergie généralisée $\mathcal{F}(\psi)$ de la forme

$$\frac{\partial \psi}{\partial t} = -\frac{\partial \mathcal{F}}{\partial \psi}. \tag{I.7}$$

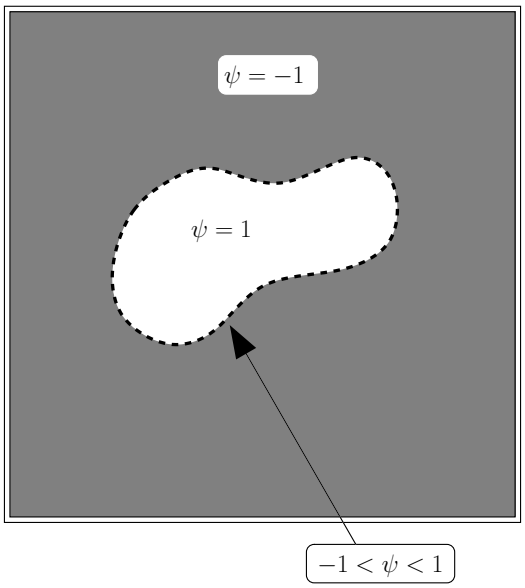

Figure I.8: Figure montrant le domaine liquide (en blanc) dans un milieu (atmosphère) et la fonction de phase $\psi(\mathbf{x}, t)$ permettant de délimiter la phase.

La construction de la fonctionnelle est montrée en (6.8), (6.9) par exemple dans le texte principal. Elle comprend quatre contributions:

- une fonction d'énergie construite de façon à placer ses minima aux points -1 et +1,
- une fonction d'énergie de surface,
- une fonction d'énergie gravitationnelle,
- une fonction d'énergie électromagnétique, qui dépend de la distribution du champ magnétique.

Il faut aussi dans les équations gouvernant le champ magnétique introduire la fonction de phase dans la conductivité électrique. Ceci nécessite de réécrire et de résoudre les équations de Maxwell en incluant la présence de $\psi(\mathbf{x}, t)$. On note que le couplage est alors double: à la fois par la forme géométrique de la frontière mais aussi à travers la conductivité électrique intervenant dans les équations de Maxwell. La résolution numérique du système nécessite une

discrétisation à haute résolution des opérateurs aux dérivées partielles au 4ème ordre en raison de la présence d'un opérateur bi-Laplacien dans le système (schéma à neuf points de Mehrstellen).

eul deux tests ont pu être mené à bien. Le premier consiste à traiter le cas d'une goutte au repos posée sur un substrat sans champ magnétique appliqué. L'objectif consiste à tester la solution numérique à la solution classique de l'équation de Young-Laplace. Les résultats sont illustrés dans la figure 6.7 du texte principal. L'accord entre les deux solutions est très satisfaisant. Le deuxième test numérique fait intervenir le champ magnétique. Il s'agit d'un problème bidimensionnel d'une goutte soumise à un effet de striction sous l'effet d'un champ magnétique alternatif dans le plan de la goutte. Dans ce cas, les forces électromagnétiques ont tendance à aplatir la goutte dans le sens des lignes de force du champ magnétique. Il existe une solution analytique obtenue par Shercliff [1981] qui a servi de référence pour la comparaison. Les résultats sont montrés dans les figures I.9 ou 6.8 et 6.9 du texte principal. Les déformations obtenues numériquement sont proches de celles fournies par la solution analytique. Avec le maillage utilisé, l'erreur est inférieure à 10%.

En raison du manque de temps, il n'a pas été possible de réaliser d'autres tests et de traiter le cas des expériences du chapitre 5. Cependant les premiers résultats montre la faisabilité de la méthode dont l'adaptation à notre problème est complètement originale. Elle ouvre une voie intéressante pour traiter les problèmes de surface libre sous champ magnétique, par exemple ceux des instabilités en lévitation électromagnétique.

Chapitre 7. Conclusions

Au cours de ce travail nous avons traité différents aspects des effets d'un champ magnétique alternatif sur une surface libre. Nous avons montré tout d'abord qu'un champ alternatif oscillant à basse fréquence pouvait générer non seulement des oscillations forcées d'une surface libre mais pouvait aussi

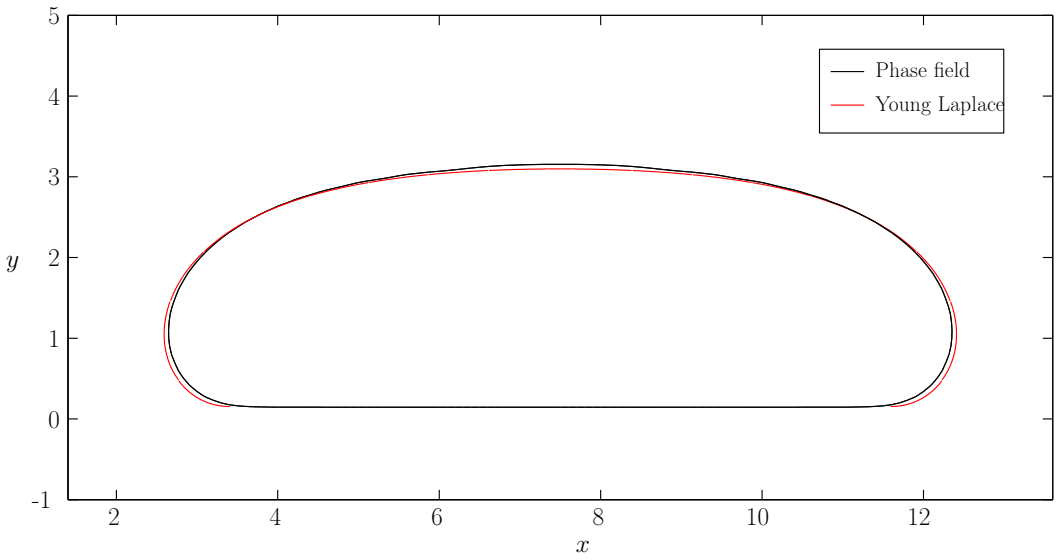

(a) Cross-section of a liquid column resting on a substrate at $y = 0$ subject to gravitation and surface tension. The surface tension parameter $\kappa = 10.4\mathrm{N\,m^{-}1}$ and density $\rho = 0.45\mathrm{kg\,m^{-3}}$.

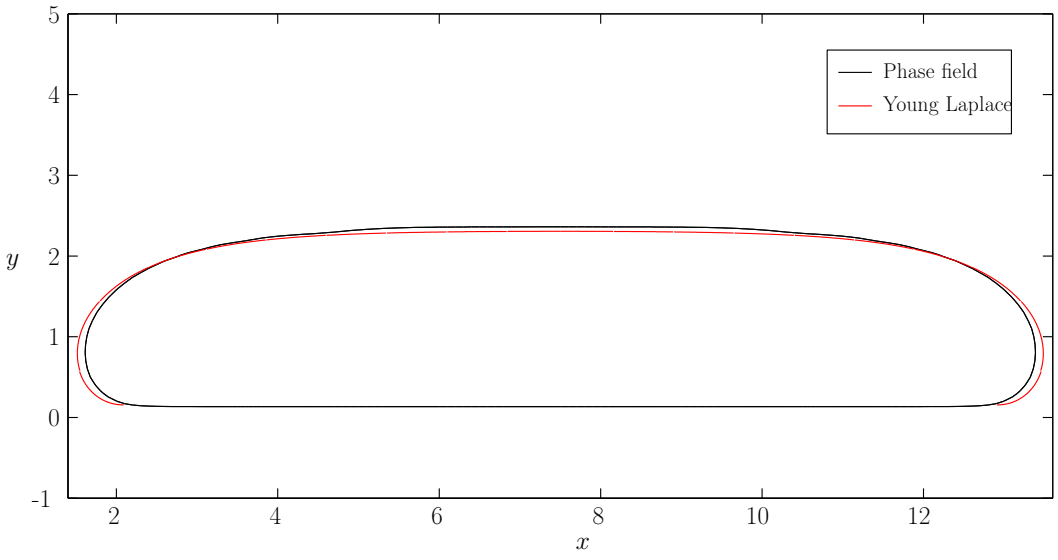

(b) Cross-section of a liquid column resting on a substrate at $y = 0$ subject to gravitation and surface tension. The surface tension parameter $\kappa = 10.4\mathrm{N\,m^{-}1}$ and density $\rho = 9\mathrm{kg\,m^{-3}}$.

Figure I.9: forme d'une goutte posée sur un substrat à grand nombre de Bond gravitaire. Comparaison entre les résultats du modèle de champ de phase et la solution analytique du problème de Young-Laplace

déclancher des instabilités de surface de type paramétrique. Deux configurations géométriques ont été analysées: la goutte circulaire et la goutte allongée. Une théorie heuristique basée sur une approche originale, une méthode lagrangienne, permis de mieux comprendre les phénomènes observés sur des expériences en métal liquide froid réalisées par Daugan (Fautrelle et al. [2005]), Ingwiller (Ingwiller [2000],Ingwiller et al. [2001]) et moi-même de le présent et travail. Ensuite nous avons considéré les cas des champs magnétiques oscillant à haute fréquence. Nous avons réalisé des expériences sur une goutte de gallium, géométrie simulant en partie celle de la lévitation électromagnétique. De nouvelles instabilités de surface libre ont été mises en évidence, faisant apparaître des morphologies de gouttes très particulières. Pour tenter de mieux analyser ces dernières instabilités, nous avons développé un modèle numérique basé sur la méthode du champ de phase. Les résultats obtenus sont préliminaires et il n'a pas été possible de simuler la géométrie de l'expérience. Seul deux cas de validation ont pu être réalisés. Cependant la méthode semble prometteuse pour traiter des cas de surface libre très déformée.

Chapter 1

Introduction

Free surface instabilities pose significant problems in many industrial processes which use magnetic fields in the processing of liquid metal. Of interest in this thesis are free-surface instabilities which are driven by the effect of alternating magnetic field on liquid metals.

There are many industrial processes where undesirable free surface instabilities occur. Induction furnaces, continuous casting and levitation melting are examples. In particular the induction furnace is commonly used in the processing of iron, steel and copper. This process exploits the action of an alternating magnetic field to heat and stir a molten metal. The magnetic field also deforms the free surface into a dome shape (Fautrelle et al. [2003]) which may subject to instabilities which cause unwanted deformation of the dome.

In continuous casting (Etay [1980], Gagnoud et al. [1986]) a high-frequency magnetic field is used to control the free surface of a liquid metal as it solidifies. This process may be subject to free-surface instabilities which lead to the formation of waves on the free surface. These waves may distort the shape of the solidified metal. Additional processing would then be required to correct the shape of the solidified metal.

Both levitation melting (patented by Muck [1923] and first studied by Okress et al. [1952]) and cold crucible processing (Schippereit et al. [1961]) use high-frequency magnetic fields to melt the metal sample and control the free surface the molten metal. As the liquid metal does not come into contact with the crucible walls contamination is avoided and reactive metal alloys may be processed. However, these processes are subject to stability problems (Sneyd and Moffatt [1982], Mestel [1982], Felici [1995]). In particular levitation melting is often limited by stability problems which cause unwanted deformation of the free surface of the molten metal. This limits the process to small samples of around 50 to 100g.

Understanding the underlying physics of these problems is a difficult as they are caused by complicated coupled phenomena. A free boundary problem

must be solved to determine the equilibrium shape and stability condition of a molten metal with respect to the electromagnetic and hydrodynamic aspects of the system. It is therefore useful to study these effects in a simple geometry which simplifies their analysis.

In this thesis we consider simple problems which exhibit free surface behaviour that is similar to industrial MHD processes.

The bulk of the work, Chapters 2 to 5, considers problems which have a similar simple geometry. In these chapters we consider the effect of low-frequency and medium-frequency alternating magnetic fields on a pool of liquid metal. The final chapter considers a different problem. We present a preliminary investigation of a Phase-field method that models the effect of a high-frequency magnetic field on the surface of a conductor in a simple 2D Cartesian geometry.

Before we outline the structure of this thesis we examine the electromagnetic phenomena present in the problems we study. The magnetic Renoylds number

$$Re_m = UL\mu_0\sigma \tag{1.1}$$

where σ is the electrical conductivity of the fluid (typically of $\mathrm{O}(10^6)$ in liquid metals), U is a typical fluid velocity and L a typical length scale of the geometry of the liquid metal. This parameter is an important measure of the distorting effect of the of the velocity of the fluid flow inside the liquid metal on the magnetic field. In all of the phenomena we study $Re_m << 1$ so the internal fluid flow does not have any effect on the externally applies magnetic field. A second magnetic Renoylds number, based on the magnetic field frequency, namely

$$R_f = 2L^2\delta_{mag}^2 \tag{1.2}$$

where

$$\delta_{mag} = (\mu_0\sigma\pi f) \tag{1.3}$$

is a measure of the effect of the geometry of the liquid metal on the magnetic field. This parameter is also known and the screen or shield parameter. The skin depth δ_{mag} is an order of magnitude estimate of the penetration depth of the magnetic field into the liquid metal.

If $R_{mag} >> 1$ then $\delta_{mag} << 0$. In this case the magnetic field, induced current and the electromagnetic force are confined to a thin skin close to the surface of the liquid metal. In this case the electromagnetic force acts like a magnetic pressure on the surface of the liquid metal. As such the geometry of the field and the liquid metal are strongly coupled. To analyse this high-frequency case develop an numerical phase-field method which we present in Chapter 6.

If $R_{mag} << 1$ then $\delta_{mag} >> L$. In this case the magnetic field penetrates the liquid metal completely to induce a current throughout the liquid metal which gives rise to an oscillating electromagnetic force of period $2f$ i.e. twice that of the magnetic field. In this case the geometry of the liquid metal has little effect on the magnetic field and the constant pressure part of the electromagnetic field is negligible. This is the case in both the "starfish" and "strip" problems studied in Chapters 2 to 4. As the external magnetic field is not influenced by the presence of the liquid metal pool, the electromagnetic calculation is simplified allowing us to derive a Lagrangian model for both the "starfish" and the "strip" problems .

However when $R_{mag} \approx 1$ then $\delta_{mag} \approx L$. In this intermediate case the magnetic field partially penetrates the liquid metal and the electromagnetic force acts as both a pressure and oscillatory force. The pressure acts on the liquid-metal surface and the oscillatory force acts to stir internal fluid flow. Although the coupled electromagnetic and fluid-flow physics of this regime are complicated and outside the scope of our Lagrangian theory, we study this experimentally in Chapter 5.

The structure of this thesis is as follows: In Chapter 2 we consider the so called "starfish problem" (Etay et al. [2003]). Submitting an initially circular pool of mercury to a vertical low-frequency magnetic magnetic field (less that 10Hz), Fautrelle et al. [2005] observe the formations of "azimuthal" modes on the pool perimeter. We consider the influence of geometry both experimentally and theoretically in Chapters 3 to 4. We replace the circular pool with an elongated "strip" like pool and investigate the behaviour of the pool when when it is subject to low-frequency magnetic fields. The behaviour of the "transverse" modes we observe is similar to the "starfish" modes. In Chapter 5 we consider a problem similar to the starfish problem but at higher frequency. The initially circular pool of liquid metal is submitted to a medium-frequency magnetic field. As the field strength is increased, two types of behaviour are observed; the first is radial oscillation of the pool perimeter, the second is rotation of the pool. In Chapter 6 we consider a problem which is somewhat different from the work we present in the previous chapters. Considering the effect of high-frequency magnetic fields on a liquid metal, we present preliminary work using an Allen-Cahn Allen and Cahn [1979] phase-field method. We use this model to calculate the equilibrium shape of an infinitely long pool submitted to gravity and a liquid metal column submitted to a parallel field.

The novel feature of our phase-field method is that we have adapted the Allen-Cahn phase-field method to model the effects of a high-frequency magnetic field on the surface conductor.

The novel feature of the work with pools of liquid metal is that we are able to reproduce and model free surface instabilities which are present in industrial MHD processes. Using a Lagrange method, we obtain semi-analytic models for both the starfish problems. We show that the azimuthal and transverse modes observed in both problems are due to a Mathieu-type subharmonic instability. One curious feature of this part of our work is that in our strip experiment we observe a complicated mode combination. This gives rise to a stability diagram which is more complicated than that of the starfish problem.

Chapter 2

The Starfish problem, mathematical model and comparison with experimental results

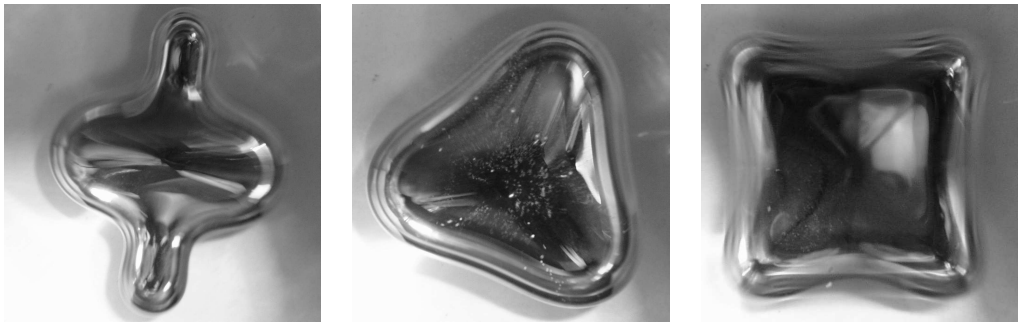

(a) Mode 2; 0.756Hz, 125A (b) Mode 3; 1.205Hz, 40A (c) Mode 4; 1.505Hz, 27A

Figure 2.1: Free surface patterns of a Ga-In-Sn pool observed by Ingwiller [2000]. This work has not been widely published so we summarise his main observations in appendix A. The figures show the various free-surface deformations which vary according to the field frequency and intensity. The proportionality factor between the magnetic field strength (maximum value in Tesla) and the coil intensity I (r.m.s. value in Ampere) is 0.0024T/A. The patterens above were observed to oscillate with frequency equal to that of the magnetic field.

2.1 Introduction

Alternating magnetic fields are commonly used in metallurgy in various industrial processes to control the free-surface behaviour of liquid metals. Examples include magnetic levitation, magnetic stirring, casting and cold crucible processes. The electric currents induced by the external a.c. field interact to create the Lorentz or electromagnetic forces. These may be responsible for free–surface deformations and vigorous fluid motion in the liquid metal.

Control of the free surface using electromagnetic forces is of interest when excessive free-surface deformations due to parametric instabilities are undesirable. These instabilities may be exploited in other processes, magnetic stirring for example, to agitate the free surface or to promote free surface transfers (Debray and Fautrelle [1994]). Indeed the application of a low-frequency magnetic field has been shown (Galpin and Fautrelle [1992] and Galpin et al. [1992]) to cause large deformations on the free surface of a circular tank of liquid mercury.

Such industrial processes generally have complicated geometry and magnetic field configurations which complicate their theoretical study. In this chapter we examine a problem which exhibits interesting free surface behaviour but has a simple geometry and magnetic field configuration - the so called "starfish" experiment (Etay et al. [2003]). In this experiment first presented in S. Daugan and Etay [1999], and later published by Fautrelle et al. [2005] (referred from now on as FED), they investigate the behaviour of a circular pool of liquid mercury (see Table 2.1 for physical properties) submitted to a low-frequency vertical alternating magnetic field. FED observe axisymmetric and azimuthal motion of the pool's free surface.

The dimensionless measure of the field strength B_0 is the magnetic interaction parameter

$$\mathcal{N} = \frac{\sigma B_0^2}{2\pi f \rho}. \tag{2.1}$$

Here ρ and σ are the density and conductivity of the liquid metal considered and f is the magnetic field frequency in hertz. The parameter $\mathcal{N}$ may be interpreted as the ratio between two typical time scales, namely the period of the magnetic field oscillations $1/f$ divided by the time of electromagnetic effect

$$\left(\frac{\sigma B_0^2}{\rho}\right)^{-1}.$$

Depending on the values of $\mathcal{N}$ and frequency f, various types of motion have been observed. For weak magnetic fields, initially the top surface moves vertically up and down, while the pool perimeter expands and contracts while remaining circular. This motion is driven directly by the Lorenz force; its oscillation frequency is thus $2f$.

For a given value of f, if a certain critical value $\mathcal{N}_{crit}$ of $\mathcal{N}$ is exceeded, a symmetry break occurs. The pool is no longer circular and periodic waves develop on the circumference which oscillate with frequency f. These azimuthal "starfish" modes are characterised by the number m of peaks on the pool's perimeter. Examples of azimuthal modes are given in Figure 2.1. They

are most easily excited near the resonance point corresponding to the natural frequencies of the pool. This behaviour is similar to parametric instability already observed by Galpin and Fautrelle [1992] and studied theoretically by Galpin et al. [1992]. Such phenomena may be applied to cause emulsion, i.e. cause a large volume of liquid metal to separate into smaller droplets. FED observe this phenomenon. In their experiment a pool of liquid metal may eject droplets when submitted to a sufficiently strong low-frequency magnetic field. A further experimental study of the same phenomena using a Ga-In-Sn alloy instead of mercury has been conducted by Ingwiller [2000]. For brevity, we shall refer to this paper as Ing from now on. As this work is not easily available we summarise his observations in Appendix A. The physical properties of both liquid metals are given in Table 2.1. Ingwiller considers a larger range of external magnetic field frequencies than FED. Thus more azimuthal modes are observed. Both investigations measure $\mathcal{N}_{crit}$ at various frequencies obtaining stability diagrams for a number of azimuthal modes.

We aim to explain the behaviour of the parametric instability which is responsible for these azimuthal "starfish" modes. We extend the model proposed by Etay et al. [2003] to consider a single azimuthal mode m on the pool's circular perimeter, and perform a linear stability analysis to determine $\mathcal{N}_{crit}$ for a number of modes m and frequencies f.

2.2 Mathematical model

We now derive a mathematical model of the pool to model the dynamics of the so-called "starfish" modes. We begin by explaining the simplified geometry.

The prior experiments (FED and Ing) were performed using a circular liquid–metal pool in the presence of a uniform vertical magnetic field

$$\mathbf{B} = B_0 \sin(2\pi f t)\widehat{\mathbf{z}}. \tag{2.2}$$

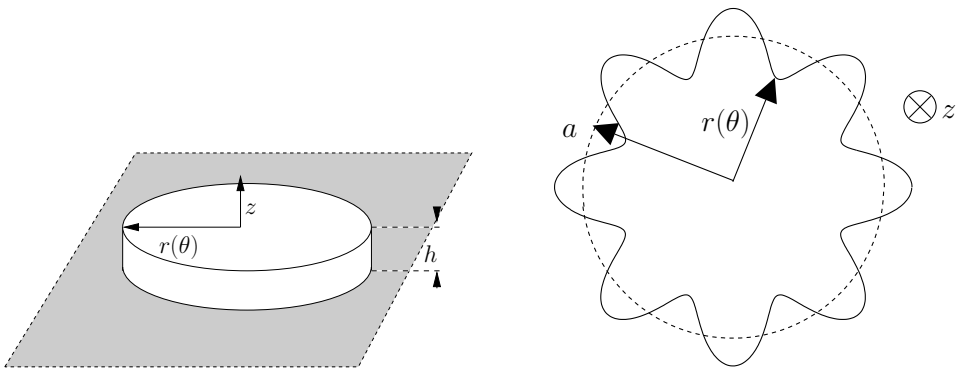

(a) Axisymmetric mode (b) Azimuthal mode

Figure 2.2: Diagram of oblique and top views of the pool geometry used in our mathematical model; the pool is cylindrical with straight vertical sides, z is the vertical coordinate. The circumference r is perturbed by a Fourier mode following the relationship $r^2 = a^2 + \epsilon a_m \cos(m\theta)$. In this case $m = 8$.

Here B_0 is the field strength, f is the frequency of the magnetic field and $\widehat{\mathbf{z}}$ a vertical unit vector.

The pool geometry is depicted in Figure 2.2. We assume that the sides of the pool remain straight and parallel to the z-axis and that its height $h(t)$ is uniform but time dependant.

We define the mean radius $a(t)$ in terms of cylindrical co-ordinates by setting

$$a(t) = \frac{1}{2\pi} \int_0^{2\pi} r_E(\theta) \mathrm{d}\theta,$$

where r_E is the cylindrical coordinate of the pool edge. We suppose that the circular edge of the pool is perturbed by an azimuthal wave of mode m say, so that the equation of the pool edge is

$$r^2 = {r_E}^2 = a(t)^2 + \epsilon a_m(t) \cos(m\theta), \tag{2.3}$$

where m is a positive integer, ϵa_m is the amplitude of the azimuthal wave and ϵ an arbitrary small parameter. The pool volume V, its radius $a(t)$ and its

height $h(t)$ are related by

$$V = \pi a^2(t)h(t) = \text{constant}. \tag{2.4}$$

Note we write equation (2.3) which describes the pool edge in terms of r^2 in order to satisfy $V =$ constant in a convenient manner.

We now derive a mathematical model describing the coupled behaviour of the axisymmetric mode and a *single* azimuthal mode. The axisymmetric mode is characterised by vertical oscillations of the pool height h, while the pool radius a remains circular, expanding and contracting. The azimuthal mode m is subject to an instability, leading to rapid growth in a_m, the amplitude of a small Fourier mode on the pool radius.

In order to simplify the analysis we ignore the detailed fluid mechanics and characterise the system in terms of two generalised coordinates: h and a_m. We then derive a Lagrangian of the system by calculating various energies of the system. The equations for $\dot{h}$ and $\dot{a}_m$ then follow from the Euler-Lagrange equations.

To justify the approximations used in our model we now discuss various dimensionless parameters. We then show that viscous damping is minor and will not significantly effect the pool's dynamics.

2.2.1 Dimensionless parameters

The equilibrium shape of the pool is defined by a balance between the surface tension force and the gravitational body force. The gravitational Bond number

$$B_g = \frac{\rho g a_0^2}{\gamma} \tag{2.5}$$

expresses the ratio of these forces where γ is the surface tension parameter and g the usual value of gravatiational acceleration. This value is moderately

large in both Daugan's and Ingwiller's experiments – 247 and 105 respectively. This indicates that the gravitational body force will tend to dominate the equilibrium shape of the pool. The pool radius at rest a_0 will tend to be much larger than its depth h_0, the upper surface being approximately flat. Thus we may consider the pool surface to be plane and horizontal. The depth h_0 can be estimated (Paddey [1969]) in terms of the capillary length ℓ_c,

$$h_0 = 2\ell_c, \text{ where } \ell_c = \sqrt{\frac{\gamma}{\rho g}}. \tag{2.6}$$

By considering the combined gravitational and surface energies of a wide flat pool, this result may be easily obtained by a minimum energy argument. This gives $h_e = 3.82$mm and 5.85mm for mercury and Ga-In-Sn respectively. These compare well with the experimentally measured values of 3.42mm and 6.11mm for mercury and Ga-In-Sn respectively.

The screen parameter R_f that measures the magnetic field created by the induced currents compared to the applied magnetic field $\mathbf{B}$ is given by

$$R_f = 2\pi\mu_0\sigma f h^2,$$

where μ_0 and σ are the magnetic permeability and electrical conductivity of the liquid metal, and h is the depth of the pool. In Daugan's experiments R_f is $O(10^{-2})$ and in Ingwiller's, $O(10^{-1})$. These values are small, thus the applied magnetic field $\mathbf{B}$ is only weakly perturbed by the presence of the pool and we may assume that the external magnetic field is unaffected by the liquid metal.

The electromagnetic forces tend to make the pool perimeter contract and expand while the surface tension and gravitational forces tend to restore the pool to its equilibrium shape. Fluid inertia tends to slow the pool oscillations. The ratio of electromagnetic and inertial forces is given by the magnetic interaction parameter $\mathcal{N}$ defined in equation (2.1). In both experiments the values of $\mathcal{N}$ at which an azimuthal mode is excited are typically $O(1)$; i.e. the magnetic and inertia forces are comparable. For very low magnetic field frequencies,

$f \leq 1$, however $\mathcal{N}$ may exceed 10, indicating that the Lorentz force becomes more dominant and that the azimuthal modes are more difficult to excite.

2.2.2 Boundary layers and viscous friction

Due to the low kinematic viscosity of both Ga-In-Sn and mercury, we may assume that the main contribution to the viscous stresses is the vertical gradients of the horizontal velocity. By making the usual boundary layer assumptions the Stokes type boundary layer thickness has the classical expression (see Batchelor [1967]),

$$\delta_\nu = \sqrt{\nu/2\pi f}. \tag{2.7}$$

Here ν is the kinematic viscosity.

When $\mathcal{N}$ is large, the Lorenz force balances the viscous term and we may expect the development of a Hartmann layer. The Hartmann number Ha given by:

$$Ha^2 = \frac{2\pi f h^2}{\nu}$$

is moderately large in both experiments, $Ha \approx 30$. Thus we may expect the development of a Hartmann type boundary layer along the bottom wall. The expression for the boundary-layer thickness δ_B(Moreau [1990]) is

$$\delta_B = \frac{1}{B_0}\sqrt{\frac{\rho\nu}{\sigma}}. \tag{2.8}$$

The Hartmann layer thickness is comparable with the viscous boundary layer thickness in both experiments. The viscous boundary layer thicknesses δ_ν in both Daugan's and Ingwiller's experiments are $O(10^{-3})$mm and the values of δ_B are comparable. These thicknesses are smaller than pool depth h. This is not surprising as the Reynolds number based on the pool depth

$$Re = \frac{2\pi f a h}{\nu}$$

Table 2.1: Physical properties of mercury and Ga-In-Sn

	Ga-In-Sn	Mercury
Density $\rho(\mathrm{kg\,m^{-3}})$	6361	13590
Electric conductivity $\sigma(\omega^{-1}\mathrm{m}^{-1})$	3.27×10^6	10^6
Surface tension parameter $\gamma(\mathrm{N\,m^{-1}})$	0.533	0.485
Kinematic viscosity $\nu(\mathrm{m^2 s^{-1}})$	3.40×10^{-7}	10^{-7}

is large; $O(10^5)$ in Daugan's experiments and $O(10^4)$ in Ingwiller's. Viscous effects remain weak near the edge of the meniscus as the capillary number

$$Ca = \frac{\rho \nu U}{\gamma}$$

is small, of $O(10^{-3})$ in both experiments. Note that $U = 2\pi f a$ is a typical meniscus velocity. Thus viscous forces and electromagnetic damping play only a small role in determining the pool dynamics. As such we may approximate the fluid flow with a flow potential ϕ say.

2.2.3 The Lorentz force

Before we evaluate the various energy terms it is necessary to discuss the Lorentz force.

Due to the simple geometry considered, and the fact that the screen parameter R_f is small, the electromagnetic force has a simple form. Fautrelle and Sneyd [2005] find that, for a volume of liquid metal of any shape with straight vertical sides and flat horizontal upper and lower surfaces, the Lorenz force $\boldsymbol{F}$ takes the following irrotational form:

$$\boldsymbol{F} = \sigma \pi f B_0^2 \sin(4\pi f t) \nabla \tau, \tag{2.9}$$

where B_0 is the amplitude the vertical alternating magnetic field of frequency f. The function τ is the torsion function for the interior of the pool perimeter,

C say. It is defined by

$$\nabla^2 \tau = -1, \qquad \tau = 0 \text{ on } C. \tag{2.10}$$

Since this result and its derivation may not be well known we briefly repeat the derivation here.

Consider Faraday's and Ohm's law,

$$\nabla \times \boldsymbol{E} = -\frac{\partial \mathbf{B}}{\partial t}, \qquad \boldsymbol{J} = \sigma \left(\boldsymbol{E} + \mathbf{v} \times \mathbf{B} \right). \tag{2.11}$$

Since the screen parameter R_f is small we may neglect the induced current $\sigma \mathbf{v} \times \mathbf{B}$. The electric current $\boldsymbol{J}$ then satisfies:

$$\nabla \times \boldsymbol{J} = -2\pi\sigma f B_0 \cos(2\pi f t)\widehat{\mathbf{z}}. \tag{2.12}$$

If we make the usual MHD approximation that $\boldsymbol{J}$ is solenoidal, and assume that the currents are confined within the liquid metal; i.e that none of the pool surface is in contact with conductors, then $\boldsymbol{J}$ must also satisfy,

$$\nabla \cdot \boldsymbol{J} = 0, \qquad \boldsymbol{J} \cdot \widehat{\mathbf{n}} = 0 \text{ on } \partial V, \tag{2.13}$$

where ∂V is the closed surface bounding the volume V of liquid metal, and $\widehat{\mathbf{n}}$ is an outward unit normal vector to ∂V.

In this case the induced current is purely horizontal and independent of the vertical co-ordinate z, so there is no charge build up on the upper and lower free surfaces. It also follows that $\boldsymbol{J}$ can be represented by a flux function G:

$$\boldsymbol{J} = \nabla G \times \widehat{\mathbf{z}}, \text{ G constant on C}, \tag{2.14}$$

where C is the curve in the (r, θ) plane corresponding to the pool perimeter. Since the quantities of interest depend only on the gradient of G, we can choose the constant to be zero provided that the region is simply connected.

The form of 2.14 that satisfies 2.12 and 2.13 identically will satisfy,

$$\nabla^2 G = 2\pi\sigma f B_0 \cos(2\pi f t). \tag{2.15}$$

The solution may then be written in the following form

$$G = -2\pi f \sigma B_0 \cos(2\pi f t)\tau[r,\theta], \tag{2.16}$$

where τ is the torsion function of the interior of the closed curve C.

The resulting Lorenz force is thus:

$$\boldsymbol{F} = \boldsymbol{J} \times \mathbf{B} = (\nabla G \times \widehat{\mathbf{z}}) \times B_0 \sin(2\pi f t)\widehat{\mathbf{z}} = \frac{1}{2} 2\pi\sigma f B_0^2 \sin(4\pi f t)\nabla\tau. \tag{2.17}$$

Note that $\boldsymbol{F}$ is irrotational.

2.2.4 Kinetic energy

The electromagnetic force (2.17) is irrotational and all body forces are conservative so the flow in the pool is irrotational (except in narrow boundary layers adjacent to the upper and lower surfaces). The flow can therefore be represented by a harmonic velocity potential say ϕ. It remains to determine the boundary conditions on the pool's edge boundary $r = r_E$ as given by (2.3).

2.2.4.1 Boundary conditions

We define a function b by setting

$$b = r^2 - r_E^2 = r^2 - a^2 - \epsilon a_m(t)\cos(m\theta). \tag{2.18}$$

Now by considering the moving curve with equation

$$b(x, y, t) = 0.$$

the following boundary condition may be derived:

$$\nabla\phi \cdot \nabla b = -\dot{b} \tag{2.19}$$

from the material derivative

$$\frac{\mathrm{D}b}{\mathrm{D}t} = 0. \tag{2.20}$$

Equation (2.19) when evaluated at $r = r_E$ gives us the required boundary condition needed to satisfy Laplace's equation. Using (2.18) for f, (2.3) and (2.19), we obtain the boundary condition,

$$2r_E \left(\frac{\partial\phi}{\partial r}\right)_{r=r_E} + \epsilon \frac{m a_m \sin(m\theta)}{a^2} \left(1 - \epsilon \frac{a_m \cos(m\theta)}{a^2}\right) \left(\frac{\partial\phi}{\partial\theta}\right)_{r=r_E} = 2a\dot{a} + \epsilon \dot{a}_m \cos(m\theta). \tag{2.21}$$

2.2.4.2 Velocity potential

We expand the velocity potential ϕ in the form,

$$\phi = \phi_0 + \epsilon\phi_1 + \epsilon^2\phi_2$$

where ϵ is the same arbitrary small number used in defining the pool edge 2.3. Because the liquid metal is incompressible,

$$\nabla^2\phi = 0.$$

We note that the boundary conditions on the upper and lower surfaces are

$$\left(\frac{\partial\phi}{\partial z}\right)_{z=0} = 0, \qquad \left(\frac{\partial\phi}{\partial z}\right)_{z=h} = \dot{h}$$

respectively. It follows that the zeroth-order velocity potential

$$\phi_0 = \alpha(z^2 - \frac{1}{2}r^2), \tag{2.22}$$

where

$$\alpha = \dot{h}/2h.$$

Now substituting the formula for ϕ_0 given by (2.22) into (2.21) and taking terms of order ϵ we find that

$$2a\left(\frac{\partial\phi_1}{\partial r}\right)_{r=a} = \dot{a}_m\cos(m\theta) + 2\alpha a_m\cos(m\theta).$$

Since ϕ_1 is an harmonic function,

$$\phi_1 = \frac{\beta}{2m}\left(\frac{r}{a}\right)^m\cos(m\theta), \tag{2.23}$$

where

$$\beta = \dot{a}_m + 2\alpha a_m.$$

Now using the formulae for ϕ_0 and ϕ_1 given by (2.22) and (2.23) in (2.21) we find that:

$$-2a^3\left(\frac{\partial\phi_2}{\partial r}\right)_{r=a} = \beta m a_m\cos(2m\theta).$$

Since ϕ_2 is an harmonic function it follows that:

$$\phi_2 = -\frac{\beta a_m\cos(2m\theta)}{8a^2}\left(\frac{r}{a}\right)^{2m}. \tag{2.24}$$

2.2.4.3 Kinetic energy

The kinetic T energy of the flow is given by

$$T = \frac{1}{2}\rho\int_V \nabla\phi\cdot\nabla\phi\,\mathrm{d}V$$

where V is the pool volume. Evaluating this integral to order ϵ^2 we find that

$$T = \rho\frac{\pi a^2\dot{h}^2}{8h}\left(\frac{4h^2}{3}+\frac{a^2}{2}\right)$$

$$+\epsilon^2\pi\rho\left(a_m\dot{a}_m\dot{h}\left(\frac{1}{4m}-\frac{1}{8}\right)+\dot{a}_m^2\frac{h}{8m}+a_m^2\dot{h}^2\left(\frac{3}{32h}+\frac{1}{8mh}\right)\right). \tag{2.25}$$

Note that the kinetic energy involves no terms of order ϵ.

2.2.5 Electromagnetic energy

The first step is to calculate the torsion function $\tau(r, \theta, t)$ for the pool, which must satisfy

$$\nabla^2 \tau = -1, \qquad \tau(r_E, \theta, t) = 0,$$

(Fautrelle and Sneyd [2005]). The strategy is to expand τ in the form,

$$\tau = \tau_0 + \epsilon\tau_1 + \epsilon^2\tau_2 \ldots .$$

To order zero in ϵ the torsion function is just that of a circle:

$$\tau_0 = \frac{1}{4}(a^2 - r^2).$$

Then the higher-order corrections to the value of τ_0 at $r = r_E$ allow us to find successively the values of τ_1 and τ_2 on the boundary. Since τ_1 and τ_2 must each satisfy Laplace's equation these functions can be determined uniquely. Thus to order 2 in ϵ

$$\begin{aligned}\tau =& \frac{1}{4}(a^2 - r^2) + \frac{1}{4}\epsilon(r/a)^m \cos(m\theta)a_m \\ & -\epsilon^2 m \frac{a_m^2}{16a^2}\big[1 + (r/a)^{2m}\cos(2m\theta)\big].\end{aligned} \tag{2.26}$$

Using 2.17 it follows that the magnetic energy per unit volume is:

$$U = -2\pi^2\rho f^2 \mathcal{N} \sin(4\pi f t)\tau.$$

The total electromagnetic energy say E_m is

$$E_m = -2\pi^2 h\rho f^2 \mathcal{N} \sin(4\pi f t) \int_0^{2\pi} \mathrm{d}\theta \int_0^{r_E} r\tau \mathrm{d}r.$$

Evaluating the integral we find that

$$E_m = -\frac{\pi^3}{8} h\rho f^2 \mathcal{N} \sin(4\pi f t)\big[2a^4 - \epsilon^2 a_m^2(1+m)\big]. \tag{2.27}$$

2.2.6 Surface tension energy

The surface tension energy is just $\gamma \times$ the surface area, where γ is surface tension coefficient. The upper and lower surfaces have a combined area of $2\pi a^2$ and the area of the pool edge (assuming this to be vertical) is

$$h \int_0^{2\pi} \left[r_E^2 + \left(\frac{\mathrm{d}r_E}{\mathrm{d}\theta} \right)^2 \right]^{1/2} \mathrm{d}\theta.$$

The total surface tension energy E_S say is given to order ϵ^2 by:

$$E_S = 2\pi a\gamma(a+h) + \frac{\epsilon^2 \pi \gamma h\, a_m^2}{8a^3}(m^2 - 1). \tag{2.28}$$

2.2.7 Gravitational energy

The gravitational energy of a column of fluid of unit cross-section area is

$$\int_0^h \rho g z \mathrm{d}z = \frac{1}{2}\rho g h^2.$$

The total gravitational energy say E_g is therefore given by

$$E_g = \frac{1}{2}\rho g h V \tag{2.29}$$

where V is the volume of the pool.

2.2.8 Lagrange's Equations

Substituting the energies (2.25), (2.27), (2.28) and (2.29) into the Lagrangian

$$L = T - E_g - E_s - E_m \tag{2.30}$$

we find that

$$L = \left(Q_1 + \epsilon^2 Q_2\right)\dot{h}^2 - P_1 + \epsilon^2\left(R\dot{h}\dot{a}_m + S\dot{a}_m^2 - P_2\right), \tag{2.31}$$

where:

$$\begin{aligned} Q_1 =& \rho V\left(\frac{1}{6} + \frac{V}{16\pi h^3}\right), & Q_2 =& \pi\rho a_m^2\left(\frac{3}{32h} + \frac{1}{8mh}\right), \\ R =& \pi\rho a_m\left(\frac{1}{4m} - \frac{1}{8}\right), & S =& \pi\rho\frac{h}{8m}, \end{aligned} \tag{2.32}$$

$$\begin{aligned} P_1 =& \frac{1}{2}\rho g h V + 2\pi a\gamma\left(a + h\right) - \pi^3\rho f^2\mathcal{N}\sin\left(4\pi f t\right)\frac{h a^4}{4}, \text{ and} \\ P_2 =& \pi\gamma\frac{h a_m^2}{8a^3}\left(m^2 - 1\right) - \pi^3\rho f^2\mathcal{N}\sin\left(4\pi f t\right)\frac{h a_m^2}{8}\left(1 - m\right). \end{aligned} \tag{2.33}$$

To obtain the equations governing the behaviour of our two generalised coordinates, pool height $h(t)$ and azimuthal wave amplitude $a_m(t)$ we apply the Euler-Lagrange equations

$$\begin{aligned} \frac{d}{dt}\frac{\partial L}{\partial \dot{h}} - \frac{\partial L}{\partial h} &= 0, \\ \frac{d}{dt}\frac{\partial L}{\partial \dot{a}_m} - \frac{\partial L}{\partial a_m} &= 0 \end{aligned} \tag{2.34}$$

to the Lagrangian (2.31) of our system to obtain the following set of coupled second order ordinary differential equations which govern the behaviour of pool height $h(t)$ and azimuthal wave amplitude $a_m(t)$:

$$2Q\ddot{h} + Q_h\dot{h}^2 + 2Q_{a_m}\dot{h}\dot{a}_m + \epsilon^2\left(R\ddot{a}_m + R_{a_m}\dot{a}_m^2 - S_h\dot{a}_m^2\right) + P_h = 0, \tag{2.35}$$

$$2S\ddot{a}_m + S_{a_m}\dot{a}_m^2 + 2S_h\dot{h}\dot{a}_m + R\ddot{h} - Q_{2,a_m}\dot{h}^2 + P_{2,a_m} = 0. \tag{2.36}$$

The subscripts $Q_h, Q_{a_m}, Q_{1,h}$ etc denote partial derivatives with respect to the generalised coordinates h and a_m and

$$Q = Q_1 + \epsilon^2 Q_2, \qquad P = P_1 + \epsilon^2 P_2. \tag{2.37}$$

We now go on to consider the two basic modes of oscillation.

2.2.9 Axisymmetric deformation

Before the critical value $\mathcal{N}_{crit}$ is reached Ing and FED observe that the pool edge remains circular, moving in and out as the top surface performs vertical nonlinear oscillations at the Lorenz force frequency $2f$.

If we suppress the azimuthal oscillations by taking $\epsilon = 0$ in (2.31) we obtain the Lagrangian for a circular pool:

$$L_{hc} = \rho V \left(\frac{\dot{h}^2}{6} - \frac{1}{2} g h \right) - \gamma \left(\frac{2V}{h} + 2\sqrt{\pi V h} \right) + \frac{\rho V^2 \pi}{4h} \left(\mathcal{N} f^2 \sin(4\pi t) + \frac{\dot{h}^2}{4\pi^2 h^2} \right). \tag{2.38}$$

The pool height $h(t)$ is the only generalised co-ordinate.

Applying the Euler-Lagrange equations (2.34) we obtain the following ordinary differential equation:

$$V\ddot{h} \left(\frac{V}{4h^3} + \frac{2\pi}{3} \right) - \dot{h}^2 \frac{3V^2}{8h^4} + \pi g V - 4\frac{\gamma \pi V}{\rho h^2} \left(1 - \sqrt{\frac{\pi h^3}{4V}} \right) + \frac{\pi^2 \mathcal{N} V^2 f^2}{2h^2} \sin(4\pi f t) = 0, \tag{2.39}$$

which governs the oscillation of the pool's upper surface at h excited by an alternating magnetic field of frequency f. An example of the non-linear axisymmetric pool deformations governed by (2.39) is given in Figure 2.3. By taking $\mathcal{N} = 0$, $\dot{h}$ and $\ddot{h} = 0$ we obtain the equilibrium condition for a pool at

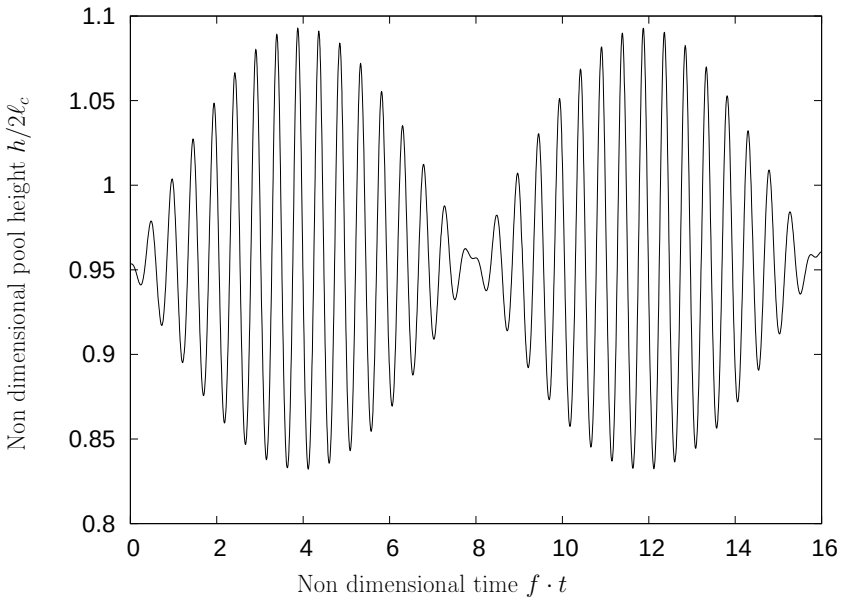

Figure 2.3: Axisymmetric oscillations of pool height h. Parameters used: $\mathcal{N} = 0.08$, $f = 1.6$ Hz.

rest:

$$\pi g V - 4\gamma \frac{\pi V}{h_0^2 \rho}\left(1 - \frac{h_0}{2a_0}\right) = 0, \tag{2.40}$$

which defines the rest pool height h_0. Unlike the simple estimate (2.6) this includes the surface tension on the pool edge in our simplified geometry. This h_0 is used as an initial condition on equations (2.35) and (2.36).

For a physical interpretation of (2.39), it is of interest to consider small-amplitude oscillations of pool height h. These correspond to small values of the interaction parameter $\mathcal{N}$. For small oscillations

$$h(t) = h_0 + \xi(t). \tag{2.41}$$

We assume that $\mathcal{N}$ is a small parameter of the same order as ξ.

Substituting (2.41) into (2.39), linearising and retaining only the terms of $O(\mathcal{N})$, we obtain the following equation governing pool motion:

$$\ddot{\xi} + \Omega_h^2 \xi = -\frac{12\pi^2 h_0 V \mathcal{N} f^2}{16\pi h_0^3 + 6V} \sin(4\pi f t), \tag{2.42}$$

where

$$(\Omega_h)^2 = \frac{\gamma\pi\left(96V - 12h_0^{3/2}\sqrt{\pi V}\right)}{\rho V\left(8h_0^3\pi + 3V\right)}. \tag{2.43}$$

Ω_h is the natural frequency of the pool oscillations. The amplitude of ξ is governed by an electromagnetically forced oscillator equation, where the forcing frequency is that of the Lorentz force: i.e twice the magnetic field frequency f. The natural frequency of the free oscillations is $F = \Omega_h/(2\pi)$. These oscillations will be most easily excited by the magnetic field at the resonant frequency:

$$f_h = F/2 = \Omega_h/(4\pi). \tag{2.44}$$

2.2.10 Azimuthal "starfish" modes

In the azimuthal regime FED note that the pool motion is purely horizontal with $h = h_0$. Thus it is of interest to investigate this regime to provide an estimate of the resonance frequencies of the various modes observed, i.e. the frequency at which an observed azimuthal mùode is most easily excited. If we assume that $h = h_0$ is constant — i.e. that the height of the pool does not vary — the remaining generalised co-ordinate a_m, the amplitude of the azimuthal mode m, has a relatively simple evolution equation:

$$\ddot{a}_m + a_m\left(\Omega_m^2 + \pi^2 m(m-1)f^2\mathcal{N}\sin(4\pi ft)\right) = 0, \tag{2.45}$$

where

$$\Omega_m^2 = \frac{\gamma m(m^2-1)}{\rho a^3}.$$

Equation (2.45) is a Mathieu equation. The solutions will grow in time when $\mathcal{N}$ exceeds a critical value. It is a well known result that the first subharmonic oscillations of a_m are the least stable. Such solutions are most unstable near the system's resonant frequency:

$$f_m = \frac{\Omega_m}{2\pi}, \tag{2.46}$$

which we call the Mathieu frequency.

We anticipate the motion to be a combination of vertical pool oscillations and azimuthal modes, the stability of the pool radius being governed by a Mathieu equation.

2.3 Results

For small $\mathcal{N}$ the azimuthal modes are not excited and the pool motion is axisymmetric. This motion is governed by equation (2.42), a simple oscillator forced directly by the Lorentz force frequency $2f$. We have also derived the resonant frequency f_h (see (2.44)) at which these oscillations are most easily excited.

For larger values of $\mathcal{N}$, when a certain critical value $\mathcal{N}_{crit}$ is exceeded, the azimuthal modes are excited. Our Mathieu approximation (see (2.45)) predicts that the strongest instability is subharmonic. For a given mode m, the Mathieu approximation also predicts that a graph of critical values $\mathcal{N}_{crit}$ versus magnetic field frequency f will have a vee shape, centred around a minimum at the eigenfrequency f_m (see (2.46)). A table of theoretical and experimentally determined values of f_m is given in Table 2.2. Critical values $\mathcal{N}_{crit}$ obtained from the Mathieu approximation are denoted by a solid line in Figures 2.4 to 2.6. Critical values $\mathcal{N}_{crit}$ obtained from the complete mathematical model (equation 2.35 and 2.36) are denoted using crosses.

Concerning the transition between the axisymmetric and azimuthal modes, we obtain predictions of the $\mathcal{N}_{crit}$ from the full model for various modes m at various frequencies. These results are graphed as solid triangles in Figures 2.4 to 2.6. These critical values are calculated to an absolute error of 1×10^{-3} using a bisection method. To determine if a value of $\mathcal{N}$ is unstable the ordinary differential equations (2.35) and (2.36) were solved using the Runge Kutta 4 method with automatic time-step control (Press et al. [1992]) with a relative

Table 2.2: Frequencies f_m for various azimuthal modes determined experimentally and using the Mathieu approximation.

Mode	f_m (Hz)			
	Ga-In-Sn		Mercury	
	Theoretical	Experimental	Theoretical	Experimental
Axi-symmetric	1.70		1.41	
Mode 2	0.66	0.95	0.44	
Mode 3	1.33	1.46	0.88	
Mode 4	2.10	1.85	1.38	1.40
Mode 5	2.96	2.50	1.96	1.60
Mode 6	3.92	3.30	2.59	1.98
Mode 7	4.96		3.28	2.33

error per step of 10^{-5}. The run was limited to 1000 periods of the magnetic field. If during a run the absolute value of the azimuthal wave amplitude a_m increases by 3 orders of magnitude larger from its initial value of 10^{-4}, the solution is considered unstable. To ensure that the values of $\mathcal{N}_{crit}$ obtained using this method were not influenced by the parameters chosen, all of the parameters mentioned above were varied by at least one order of magnitude. Results were not significantly changed.

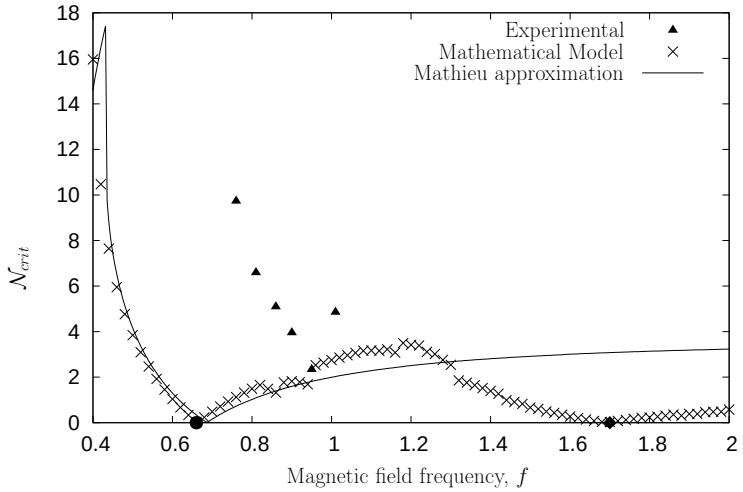

(a) Comparison of stability diagrams obtained using the full model, the Mathieu approximation and experimental results obtained by Ing for azimuthal mode $m = 2$.

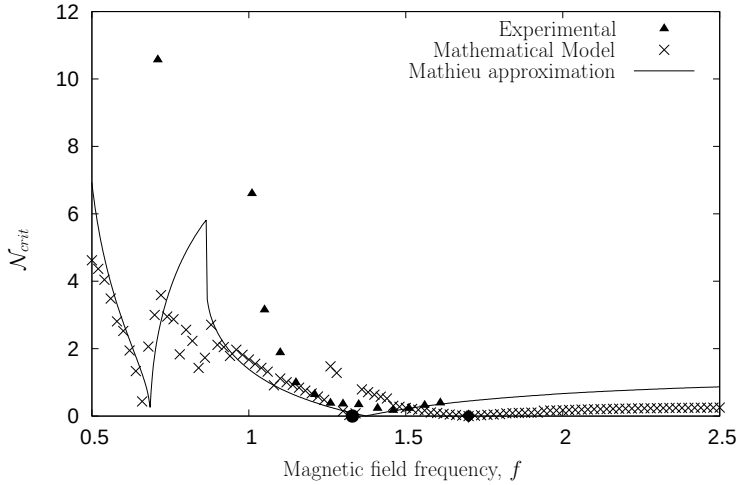

(b) Comparison of stability diagrams obtained using the full model, the Mathieu approximation and experimental results obtained by Ing for azimuthal mode $m = 3$.

Figure 2.4: Comparison between theory and experiment for azimuthal modes $m = 2$ in Figure 2.4(a) and mode $m = 3$ in Figure 2.4(b). Considering a pool of Ga-In-Sn of 3cm radius, the predicted critical values of the magnetic interaction parameter $\mathcal{N}_{crit}$ at various magnetic field frequencies f obtained from the mathematical model and the Mathieu approximation are plotted with experimental results obtained by Ing. The solid diamond marks the position of the resonant frequency f_h of the axisymmetric oscillations predicted by our theory. The solid circle marks the position of the first subharmonic resonant frequency of the azimuthal oscillations f_m predicted by the Mathieu approximation. From Mathieu theory this is expected to be the strongest resonance if the axisymmetric modes are ignored.

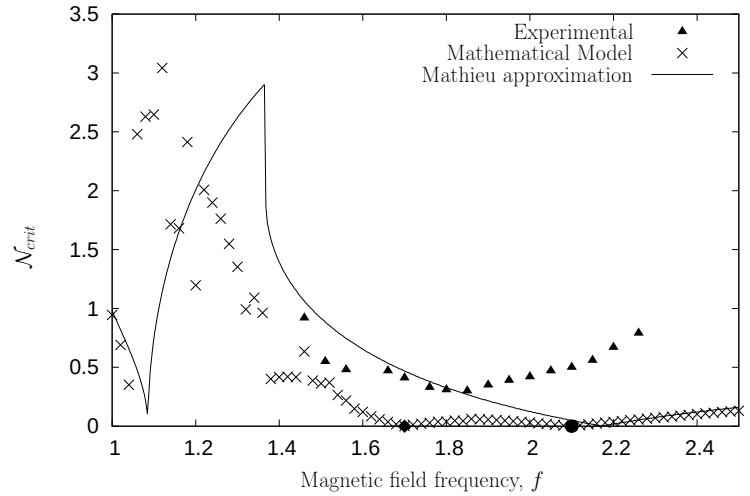

(a) Comparison of stability diagrams obtained using the full model, the Mathieu approximation and experimental results obtained by Ing for azimuthal mode $m = 4$.

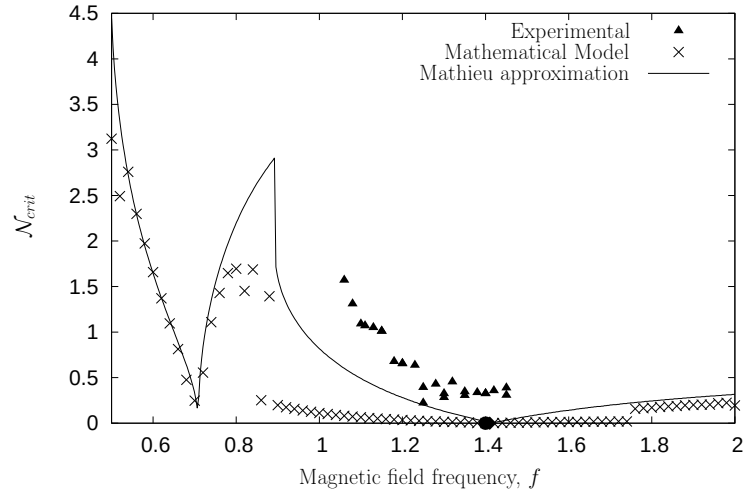

(b) Comparison of stability diagrams obtained using the full model, the Mathieu approximation and experimental results obtained by FED for azimuthal mode $m = 4$.

Figure 2.5: Comparison between theory and experiment for azimuthal mode $m = 4$ of a pool 3cm radius. In Figure 2.5(a) a pool of Ga-In-Sn is considered while a pool of mercury is considered in Figure 2.5(b). The predicted critical values of the magnetic interaction parameter $\mathcal{N}_{crit}$ at various magnetic field frequencies f obtained from the mathematical model and the Mathieu approximation are plotted with experimental results obtained by Ing using Ga-In-Sn or FED using mercury. The solid diamond marks the position of the resonant frequency f_h of the axisymmetric oscillations predicted by our theory. The solid circle marks the position of the first subharmonic resonant frequency of the azimuthal oscillations f_m predicted by the Mathieu approximation. From Mathieu theory this is expected to be the strongest resonance if the axisymmetric modes are ignored.

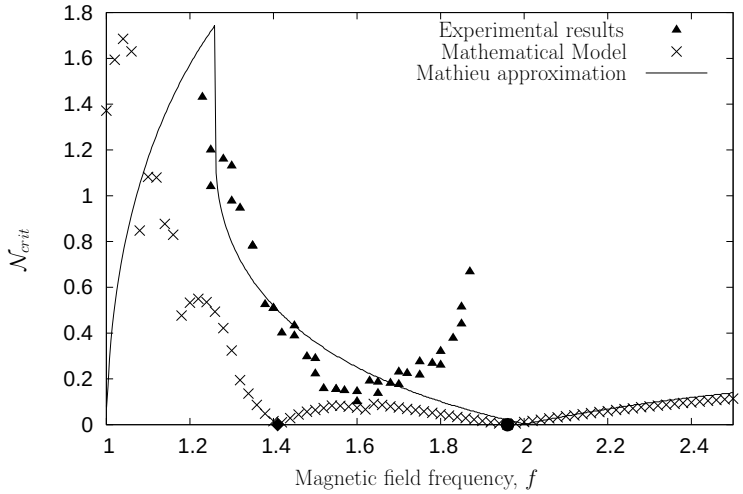

Figure 2.6: Comparison between theory and experiment for azimuthal mode $m = 5$ of a pool of mercury of 3cm radius. The predicted critical values of the magnetic interaction parameter $\mathcal{N}_{crit}$ at various magnetic field frequencies f obtained from the full mathematical model and the Mathieu approximation are plotted with experimental results obtained by FED. The solid diamond marks the position of the resonant frequency f_h of the axisymmetric oscillations predicted by the our theory. The solid circle marks the position of the first subharmonic resonant frequency of the azimuthal oscillations f_m predicted by the Mathieu approximation. From Mathieu theory this is expected to be the strongest resonance if the axisymmetric modes are ignored.

2.4 Discussion

We have compared our model with the experimental results of FED and Ing. We feel that the comparison is not exact but reasonable given the following analytical simplifications:

- treatment of the fluid flow is simplified as we ignore damping,
- we assume a uniform applied magnetic field,
- we assume that the shield parameter (R_f) is small,
- we use a single fundamental mode to describe the axisymmetric deformations,
- we consider a small azimuthal mode in isolation.

We feel that the last two assumptions are the most important source of discrepancy between the experimental and theoretically calculated stability diagrams.

From Figures 2.4 to 2.6, we observe that the stability diagrams obtained from the Mathieu approximation and the full model have the same basic structure as those obtained experimentally. That is to say, the experimentally obtained values of $\mathcal{N}_{crit}$ have the same vee shape as the theoretically determined values; i.e. a minimum centred on the eigenfrequency f_m of the mode under consideration. The important difference between the experimental and theoretical stability diagrams is that the experimentally determined curves are displaced from the theoretically predicted ones by as much as 50%; i.e. the theoretically determined eigenfrequencies for the azimuthal modes differ largely from those determined experimentally (see Table 2.2). This discrepancy is likely due to the analytical simplifications made to derive our theory. Indeed, first the meniscus near the edges of the drop is not taken into account, and second the real interaction between the drop and substrate is not treated. In particular, the mobility of the free surface beneath the drop is not treated in detail. In the experimental cases the kinematic boundary conditions at the bottom part

of the drop were not fully controlled. Miles (Miles [2006]) has shown in the case of a tank with a horizontal free surface having a fixed triple point, that the theoretical eigenfrequencies were overestimated.

At low magnetic field strengths corresponding to small $\mathcal{N}$, FED and Ing observe that the pool's motion is simple, the pool remains circular and its perimeter moving in and out as the upper surface oscillates up and down at $2f$, the Lorenz force frequency. Our theory predicts similar behaviour. We obtain the simple oscillator (2.42), forced electromagnetically at $2f$, governing pool height h when $\mathcal{N}$ is small.

Once a certain threshold value of $\mathcal{N}$ is exceeded, FED and Ing observe the growth of wave like indentation which oscillates at f, *half* the frequency of the Lorenz force. We have named these deformations azimuthal modes and have modelled them in terms of a single Fourier mode imposed on the pool edge as shown in Figure 2.2. We then derive a model governing the evolution of the amplitude a_m of these modes. As in the experiments, we observe that a_m grows by several order of magnitude when a certain critical value of $\mathcal{N}_{crit}$ is exceeded.

Although the positions of the stability curves predicted using our theory are displaced from those obtained experimentally, the qualitative behaviour is similar, indicating that the "starfish" azimuthal modes are due to a Mathieu type subharmonic parametric instability, where the governing parameters are the magnetic field frequency f and the magnetic interaction parameter $\mathcal{N}$.

It is clear in the experiments that the amplitude of the azimuthal waves which are observed is not small. Thus there is almost certainly some mode coupling. Indeed Ing has observed mode coupling in his experiments. This effect is not taken into account by the current theory, which considers only an isolated mode of small amplitude and it is not clear what error this introduces. Possible future work on this problem could consist of a theoretical study of the interactions between different azimuthal modes.

Chapter 3

Experimental investigation of free-surface parametric instabilities of a strip of liquid metal excited by low-frequency magnetic field

3.1 Introduction

In this chapter we continue investigating the effect of low-frequency magnetic field on pool liquid metal. In particular we study the effect of geometry by investigating the behaviour of an elongated "strip" of liquid metal – a Ga-In-Sn eutectic – which is submitted to a vertical low-frequency magnetic field. What follows in this chapter is our experimental investigation of the "strip". We analyse our results using the Lagrangian theory in Chapter 4.

We observe a variety of pool behaviour which we present in Section 3.5.1, and we are primarily concerned with the onset of standing waves on the pool perimeter. Such waves develop when a certain critical value $\mathcal{N}_{crit}$ say of the magnetic interaction parameter

$$\mathcal{N} = \frac{\sigma B_0^2}{2\pi f \rho}$$

is exceeded. Here B_0 and f are the magnetic field amplitude and frequency, and ρ is the density of the liquid metal.

Various transverse modes are excited as shown in Figures 3.18 to 3.22. They may be grouped in two categories: varicose "V" modes, which are symmetric about a line running through the centre of the drop; and sinuous of "S" modes which are antisymmetric.

For various field frequencies f, we determine the values of $\mathcal{N}_{crit}$, i.e. the critical value of $\mathcal{N}$ at which a transverse modes is first excited. Due to the more complicated pool geometry, measurement of the wavelengths λ of the transverse modes observed is not as straightforward as in the case of the "starfish" experiment of Fautrelle et al. [2005] (see Chapter 2). To measure λ we analyse short films, which were recorded for each observed transverse mode. The experimental apparatus and protocol used is explained in the following section. Our observations and measurements are given in Section 3.5. A detailed analysis of the behaviour of the transverse modes is described in Chapter 4.

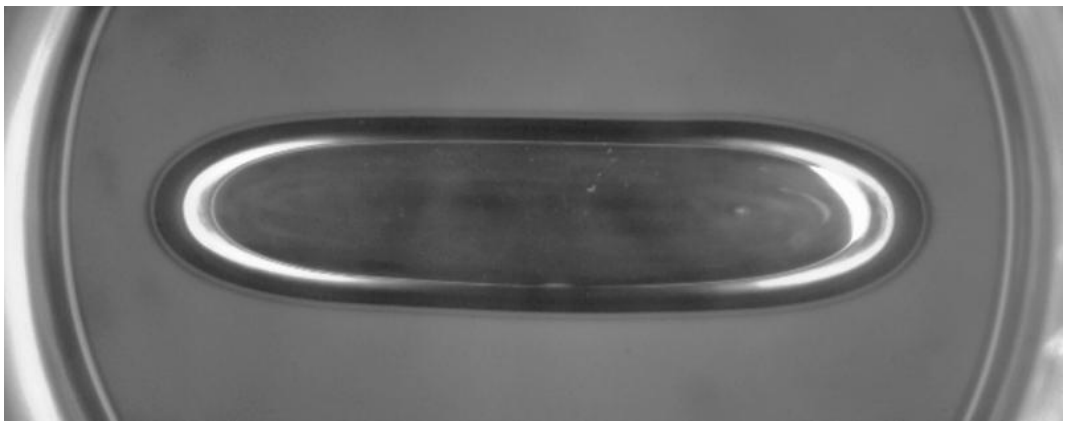

Figure 3.1: View from above of pool at rest.

3.2 Experimental apparatus

We use an apparatus which is similar to that used by Fautrelle et al. [2005] with a few modifications. Due to its low toxicity we use Ga-In-Sn instead of mercury. This alloy oxidises much more quickly than mercury, requiring that it be immersed in an alcohol-acid solution. A small volume of liquid metal $\mathcal{V}$, in this case $\mathcal{V} = 18.9$ml, is placed on a substrate surrounded by a coil carrying an electric current. On a flat or concave substrate, the pool assumes a circular perimeter due to surface tension. Our substrate has a vee shaped profile as shown in Figure 3.3, which stretches the pool into an elongated "cigar" shape at rest as shown in Figure 3.1.

By photographic analysis, we were able to measure the length ℓ and the area of the upper pool surface A of the pool at rest i.e in the absence of a magnetic field. They are

$$\ell = 120\text{mm} \qquad \text{and} \qquad A = 3630\text{mm}^2. \tag{3.1}$$

From these we may calculate the average pool depth $h_0 = 5.2$mm and average pool width $w = 30$mm. This is close to the pool width at its centre $w_c = 31$mm. The coil produces a uniform vertical alternating magnetic field,

$$\mathbf{B} = B_0 \sin(2\pi f t)\widehat{\mathbf{z}} \tag{3.2}$$

of frequency f around the liquid metal where $\widehat{\mathbf{z}}$ is the vertical unit vector. The proportionality constant of the magnetic field intensity B_0 in the centre of the coil and the RMS (root mean square) value of current in the coil is 0.00255 T/Amp. The RMS current I_{rms} in the coil is related to the tension U_{rms} across the coil which is provided by the generator by

$$I_{rms} = \frac{U_{rms}}{Z}. \tag{3.3}$$

Here Z is the impedance of the coil in Ohms. The impedance Z is a linear function of f, and

$$Z = (0.2155f + 0.3132). \tag{3.4}$$

Thus the magnetic field strength at the centre of the coil is given by

$$B_0 = \frac{0.00255U_{rms}}{0.2155f + 0.3132}. \tag{3.5}$$

The liquid metal used is a Ga-In-Sn eutectic. Its physical properties are given in Table 2.1. The acid solution used is a weak HCl-ethanol solution which has a density $\rho_e = 789\,\mathrm{kg\,m^{-3}}$. This is significantly smaller than the density of Ga-In-Sn, reducing coupling between the two liquids. In addition, to minimise coupling of the pool deformation with the alcohol-air free surface, the depth of the solution is 10cm. This is much larger than the depth of the pool which is close to 5mm. During the experiments deformation of the alcohol/air surface were observed only for values $\mathcal{N}$ which were significantly larger than $\mathcal{N}_{crit}$. Thus for the purposes of theoretical analysis of the pool's behaviour, the effect of the surrounding alcohol-acid solution may be ignored.

To reduce oxidation both the Ga-In-Sn and the alcohol solution are contained in a cylindrical PVC vessel, the Ga-In-Sn resting on a substrate at the bottom. The top is covered by a clear polished plexiglass lid, and a seal between the lid and vessel is maintained by a large rubber O-ring seal. The apparatus is depicted in Figure 3.2.

The combination of the alcohol-acid solution and the seal allowed the same Ga-In-Sn sample to be used for 6 hours continuously. Oxidation, when it occurred, was manifested by the rapid formation of a grey "crust" on the liquid-metal surface, and by a drastic reduction of the mobility of the liquid-metal-substrate-alcohol triple point i.e the point where all 3 are in contact. Steps taken to avoid oxidation are explained further in Section 3.3.

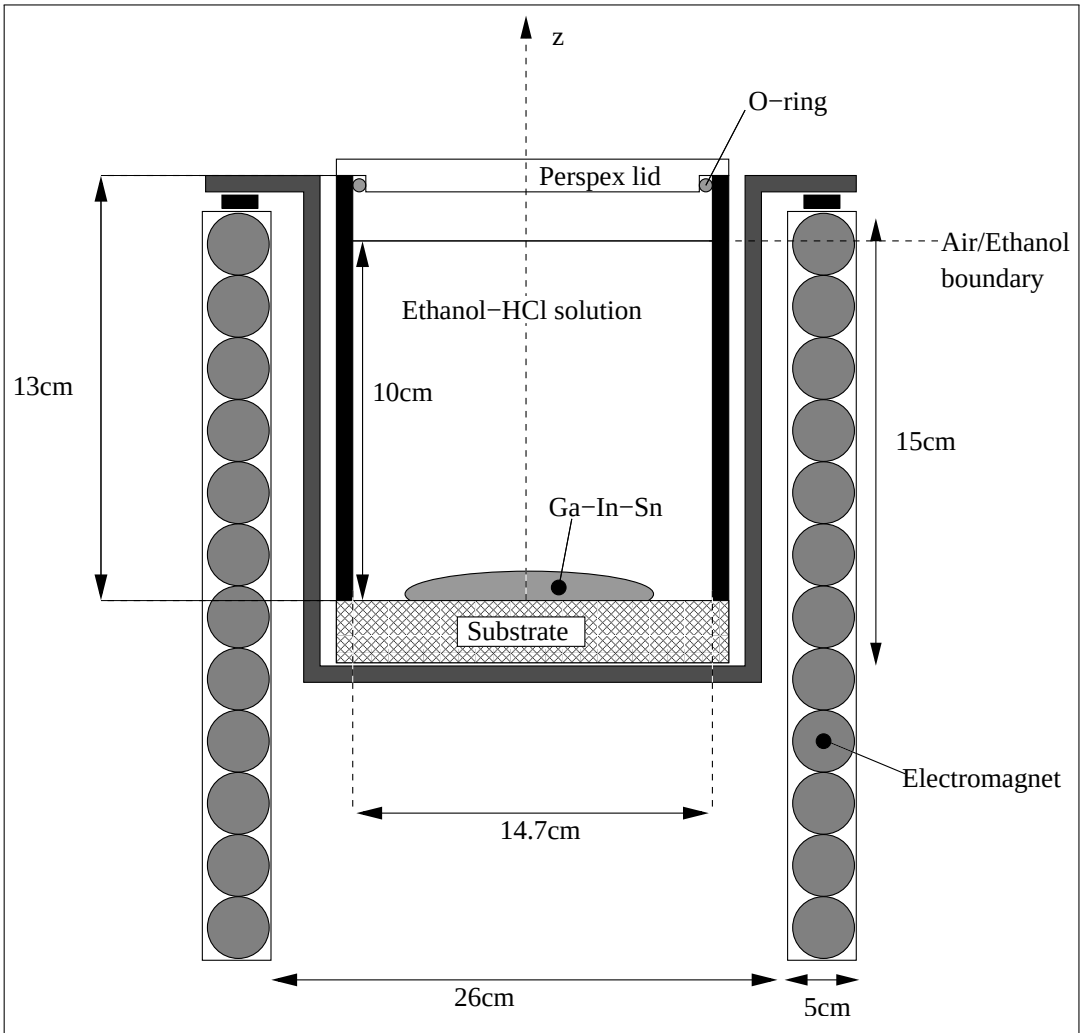

Figure 3.2: Side view of experimental apparatus

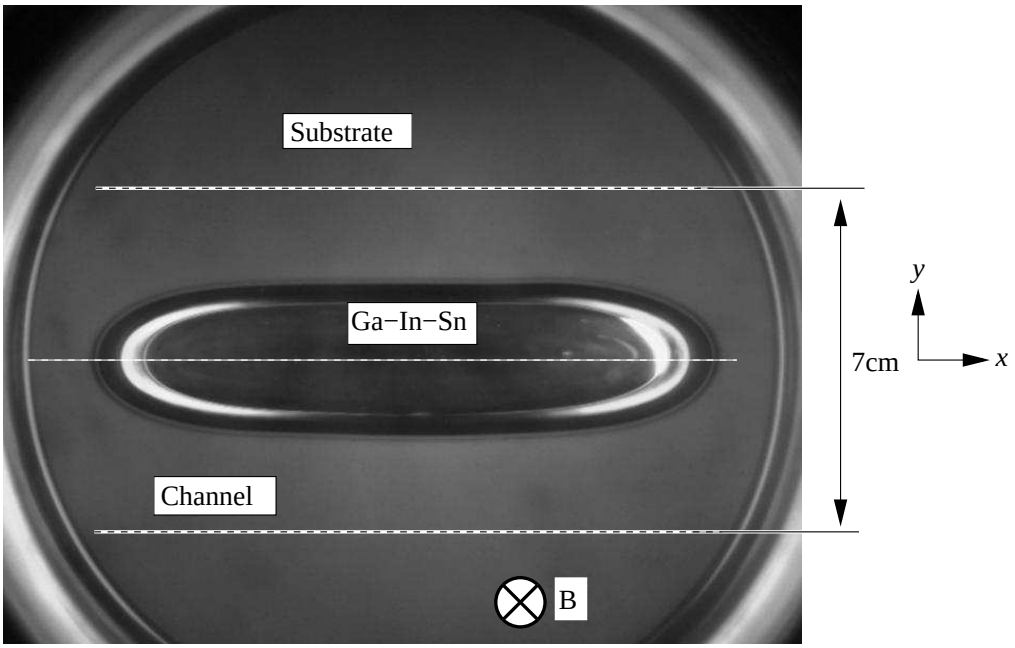

(a) Top view of Ga-In-Sn pool and substrate, indicating the position and size of the V shaped channel.

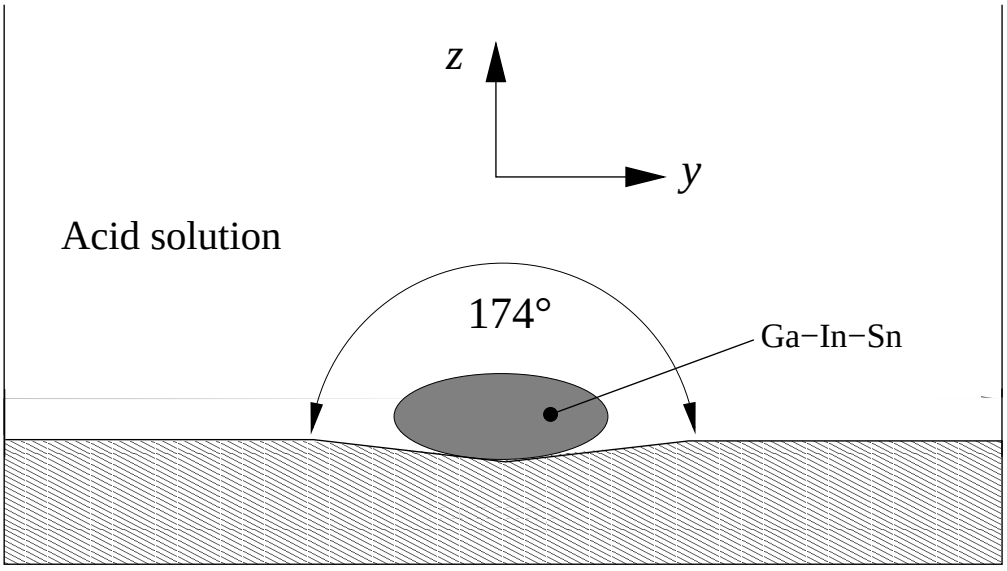

(b) Side view of substrate showing the slope of the channel.

Figure 3.3: Top and side view of Ga-In-Sn drop and substrate in the experimental apparatus.

3.3 Experimental protocol

While various types of pool behaviour were observed, the main objective of our experimental study is to obtain a stability diagram for the transverse "S" and "V" modes. Thus the experimental protocol is primarily concerned with

accurately measuring $\mathcal{N}_{crit}$ at various frequencies at which transverse waves are first excited.

3.3.1 Preparation of the experimental apparatus

Between experiments the Ga-In-Sn was stored under an HCl-ethanol solution to reduce oxidation. Nonetheless some oxidation of the liquid metal surface would occur. This was removed simply by replacing the surrounding solution with a fresh one; the HCl would then react with the oxide removing it from the Ga-In-Sn surface.

To ensure consistency between experimental runs, the volume of Ga-In-Sn used had to be measured accurately before it was placed in the PVC container. This was done by weighing the sample on electronic scales. The mass used was 120g and could be determined to within 0.1g by the scales to give a relative error in mass and thus volume to just under 0.1%.

The Ga-In-Sn was then placed in the PVC container with the alcohol-acid solution and the lid was placed on top. During the course of the experiment ethanol from the alcohol solution would condense on the bottom surface of the lid. This would obscure our view of the Ga-In-Sn pool, requiring the lid to be removed and cleaned. This condensation would also react with the lid, and eventually the lower lid surface would become cloudy and small cracks would form on it. Thus the lid was checked at the beginning of each run and was re-polished if necessary.

3.3.2 Measurement of critical values $\mathcal{N}_{crit}$

The amplitude B_0 of the magnetic field produced by coil was varied by changing the tension provided by the generator U_{rms}. The generator allowed both the frequency f and tension U_{rms} to be varied. For convenience we vary B_0 by varying U_{rms} in fixed steps of 2 volts.

Experimental runs were conducted over the course of 2 hours, after which the Ga-In-Sn pool was checked for signs of oxidation. Additionally the two measurements performed at the start of the run were repeated. In the event of a discrepancy, we replace the Ga-In-Sn sample and acid-alcohol solution and repeat the entire run. Although not a common occurrence, we have found that such discrepancies were due to slight oxidation on the Ga-In-Sn surface.

As we have observed hysteresis (see Section 3.5.5) in our preliminary measurements of $\mathcal{N}_{crit}$, for consistency we always measure $\mathcal{N}_{crit}$ by increasing $\mathcal{N}$ from a value which is less than an initial estimate of $\mathcal{N}_{crit}$. To obtain an experimental estimate of $\mathcal{N}_{crit}$ for a transverse mode which is excited at a given frequency f say, we slowly increase the tension provided by the generator in steps of 2 volts until a transverse mode is excited. According to equation (3.5) this corresponds to changes of B_0 of 8×10^{-3} T at 1.5Hz to 2.5×10^{-3} T at 8Hz.

The transverse modes were sometimes difficult to excite and could take a considerable time to appear when $\mathcal{N}$ is close to $\mathcal{N}_{crit}$. We have observed that a mode may appear after an interval as long as 5 minutes. Because of the large number of necessary observations, we waited for only 2 minutes in practice before increasing U_{rms}. At first a quick measurement is performed. We raise the U_{rms} from zero rapidly to obtain a crude estimate of $\mathcal{N}_{crit}$. Then we repeat twice, starting at 6 volts and then 4 volts below our initial estimate. We use two different starting tensions as we have observed that if we start with a value of $\mathcal{N}$ which is too close to $\mathcal{N}_{crit}$ we may not obtain the same value as if we had started at $\mathcal{N} = 0$. In cases where the two measurement do not agree we discard both and perform two measurements, starting with $U_{rms} = 0$ in both cases.

In the course of our experiments we observe that some modes are particularly difficult to excite, particularly when $f > 6$Hz. In this case we observed large variations as large as 50% in our measurements of $\mathcal{N}_{crit}$, so we performed four measurements in place of the usual two.

3.4 Image analysis

To identify the various transverse modes observed and to calculate their wavelength, a short film is taken of each observed mode. These films were recorded using a PixeLINK PL-B742F camera at 25fps (frames per second) at a resolution of 1280×1024 pixels. Typically these films consisted of approximately 300 images recorded over 10 to 12 seconds. In cases where mode combination was observed, longer films containing footage of all the modes observed were made. These films were captured and saved electronically in avi file format using the Streampix software from NorPix. The films were then processed using Matlab to calculate the wavelength of the observed transverse mode.

The method used to calculate the wavelengths of the azimuthal modes observed is complicated, and is performed in three steps:

- Preprocessing
- Pool boundary extraction
- Measurement of transverse wave wavelength λ

These are explained below. The Matlab codes written to perform these steps is given in Appendix B

3.4.1 Preprocessing

The films obtained during the experiments were of the entire substrate and some of the surrounding area. The section of interest is the pool, so we can discard much of the surroundings by cropping the films to an area 1280 pixels long and 500 pixels high. An example of a cropped frame is shown in Figure 3.4(a). We must take care to include the left and right ends of the pool substrate as the diameter of the substrate provides the length-scale of the image.

3.4.2 Pool boundary extraction

Before we can calculate the wavelength of a given transverse mode, we first must isolate the pool contour in each frame of the film F say.

We represent the film F as a series of images, $I^1, I^2, \ldots, I^m, \cdots, I^n$. These correspond to observations made at equally spaced time intervals Δt. As these are colour images each I^m may be represented as three two dimensional matrices $R^m_{i,j}$, $G^m_{i,j}$ and $B^m_{i,j}$ which represent the intensity at pixel (i, j) of the red, green and blue colours respectively.

To trace the contour of the pool we use the Canny edge detection algorithm (Canny [1986]) implemented in Matlab. Initially we used a white substrate and applied the Canny algorithm to a single red channel but were unable to obtain consistent results for all of the images in a film. This appeared to be due to the reflective nature of the Ga-In-Sn, which made it difficult to distinguish the pool from the substrate. Better results were obtained by using a red substrate and by applying the Canny algorithm to the ratio

$$C^m_{i,j} = R^m_{i,j}/B^m_{i,j} \tag{3.6}$$

of red to green. As the substrate is red, $C^m_{i,j}$ is generally larger for the substrate than for the silver drop. An example of the image corresponding to $C^m_{i,j}$ is given in Figure 3.4(b). As can be seen in Figure 3.4(b) the resulting image is quite noisy, this is removed using Matlab's medfilt2 function which implements a second order statistic filtering (Huang et al. [1979]), an example of a filtered image is given in Figure 3.4(c). We then apply the Canny edge detection algorithm to the filtered $C^m_{i,j}$ to detect the pool perimeter (see Figure 3.4(d)). From this we can isolate the pool profile $P^m_{i,j}$ as shown in Figure 3.4(e). So using this method, for each frame m in film F, we extract the pool profile $P^m_{i,j}$ and save these as a film (H say) from which we measure the wavelengths of the transverse mode observed.

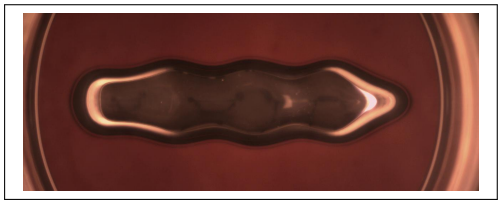

(a) Cropped image

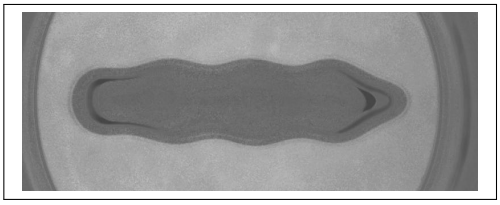

(b) Image of $C_{i,j}^m$

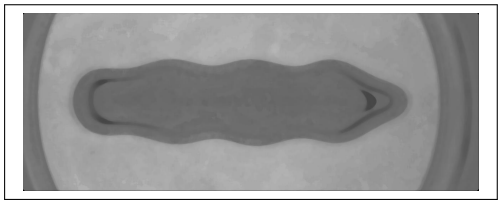

(c) Image of filtered $C_{i,j}^m$

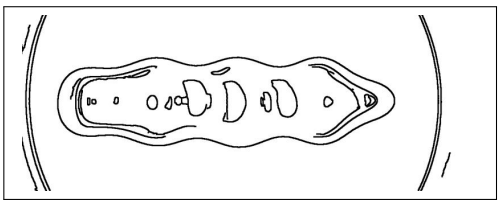

(d) Image edges detected using Canny algorithm

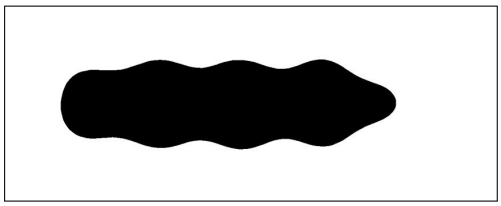

(e) Pool isolated using the edges detected

Figure 3.4: Images of the steps taken during the image processing of the film of mode 8.0V taken during the experiments.

3.4.3 The transverse mode wavelength λ

Considering the film H of pool profiles we now explain our algorithm for measuring the transverse mode wavelength λ.

First for each frame m in film H, we trace the upper half of the pool perimeter as a curve D^m as shown in Figure 3.5(a). These curves correspond to forms of the pool perimeter observed at various times $t^m = m\Delta t$. We filter this data by taking a FFT (fast Fourier transform) in time of all the D_m, and we keep only the Fourier components that are close to f, which happens to be the frequency of oscillation of the azimuthal mode as we will show in Section 3.5.1.1. We take the inverse transform of the result (see Figure 3.5(b) for an example) and estimate the wavelength of the azimuthal mode by fitting a sine wave of the form:

$$g^m(x) = \sin\left(k^m x + \phi\right) \tag{3.7}$$

to the resulting waveforms.

The wavelength $\lambda^m = 2\pi/k^m$ is calculated for each fitted wave. We then examine the distribution of the λ^m by taking a histogram which sorts the λ^i in 1mm sized bins. Generally one bin contains a larger proportion (exceeding 50%) of the wavelengths λ^m. The bin with the largest number of wavelengths λ^m is taken as the most likely wavelength and the best estimate of the wavelength λ for the transverse mode observed.

3.5 Results

In the present experiments the parameter space consists of two quantities:

1. the magnetic field strength B_0 or equivalently interaction parameter $\mathcal{N}$;
2. the magnetic field frequency f or equivalently angular frequency $\omega = 2\pi f$.

3.5.1 Surface patterns

For relatively small values of $\mathcal{N}$ we observe only a simple deformation of the pool, its perimeter expanding and contracting while the upper surface moves up and down at the Lorentz force frequency $2f$ as shown in Figure 3.7.

3.5.1.1 Transverse deformation

For larger values of $\mathcal{N}$ we observe that pool perimeter is deformed in a regular pattern. Regularly spaced indentations oscillate in a direction perpendicular to the sides of the pool. These we call "transverse" modes. Examining the power spectrum

$$p = |\mathcal{F}|^2 \tag{3.8}$$

of the FFT in *time* of the pool perimeter, we see that the FFT component $\mathcal{F}_i$ which has the greatest power is the component at frequency f. Example powers

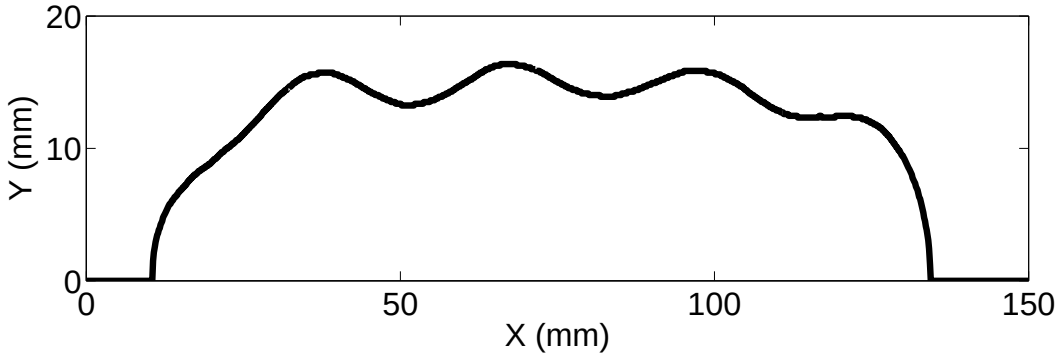

(a) Upper half of pool waveform.

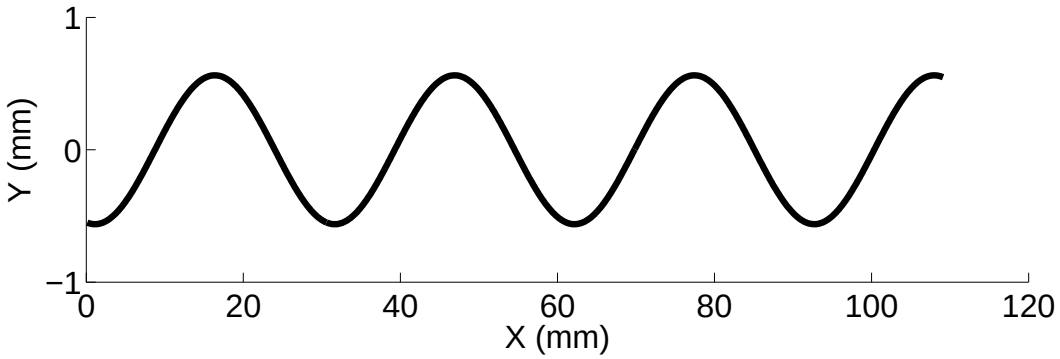

(b) Waveform obtained from inverted FFT.

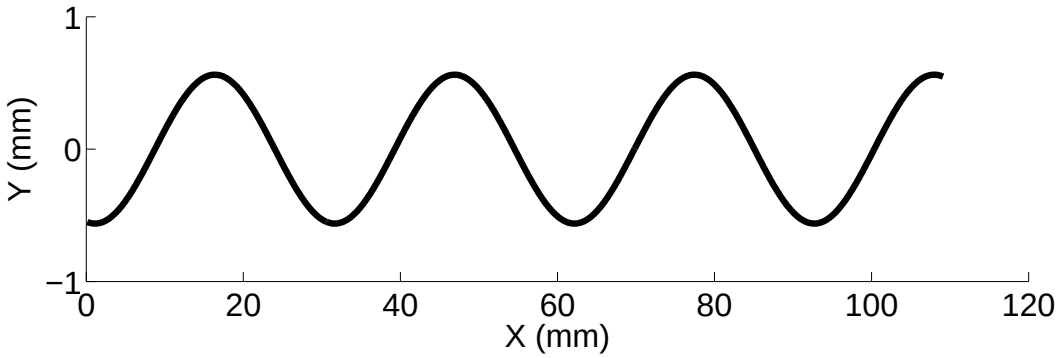

(c) Sine wave fitted to waveform obtained from inverted FFT.

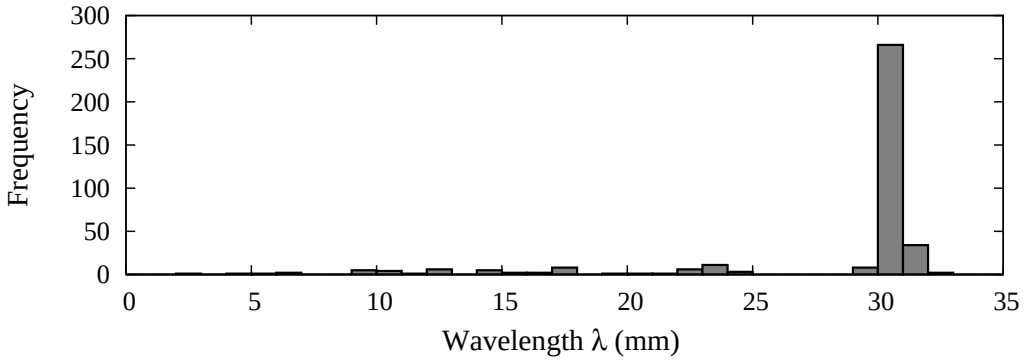

(d) Histogram of wavelength λ^i of fitted waveforms.

Figure 3.5: Figures illustrating the algorithm used to calculate the wavelength of the 8.0V transverse mode.

spectra are given in Figure 3.15. The transverse modes are *subharmonic* as they oscillate with frequency f which is half the frequency of the Lorentz force. These subharmonic transverse modes may be classified into two types: varicose (V) and sinuous (S) modes. The deformation of the pool perimeter due to varicose modes is symmetric about a centre-line running though the middle of the pool. Conversely the deformation due to sinuous modes is antisymmetric.

The number m say used to name an observed mode is simply the ratio:

$$m = \frac{\ell}{2\lambda} \tag{3.9}$$

rounded to the nearest tenth. Here ℓ is the pool length at rest, i.e in the absence of a magnetic field and λ is the wavelength of the transverse mode which is measured using the method outlined in Section 3.4. As there are two mode types: varicose and sinuous, we append the letter V to the name of varicose modes and S to sinuous modes. Thus using our nonclementure, the mode 8.0V say is the varicose transverse mode which has $m = 8.0$. Figure 3.8 shows one period of oscillation of the $8.9V$ mode and examples of each transverse mode observed are displayed in Figures 3.18 to 3.22.

3.5.2 Elliptic deformation of the pool perimeter

If we continue increasing $\mathcal{N}$ beyond $\mathcal{N}_{crit}$ we observe a third type of deformation. In addition to the transverse mode, the pool's length contracts and expands causing the pool's width to contract and expand maintaining an ellipse-like shape. This "elliptic" mode oscillates slowly, superimposed on an azimuthal mode as shown in Figure 3.9. The frequency of oscillation of this mode appears to be regular, but does not appear to depend on f alone, because for the same f, different oscillation frequencies are observed for different $\mathcal{N}$.

3.5.3 Mode combination

At larger $\mathcal{N}$ the elliptic deformation is not observed. The pool deformation reverts to the transverse regime. We observe that the number of indentations on the pool perimeter and their spacing changes as the pool oscillates suggesting that secondary transverse modes are excited and are interacting with the first transverse mode excited. The onset of this mode combination is shown in Figure 3.10. For larger $\mathcal{N}$ we observe a greater variation in the number of indentations and their spacing (see Figure 3.11), but symmetry (or antisymmetry) across a centre-line through the pool is preserved.

3.5.3.1 Chaotic deformation

For $\mathcal{N}$ of order 1, the pool deformations become increasingly complicated and the symmetry across a centre-line through the pool is broken. Both the spacing between indentations and their amplitude became irregular as shown in Figures 3.12 and 3.13. Continuing to increase $\mathcal{N}$ causes the amplitude of the indentations to grow forming long thin "fingers" as shown in Figure 3.13. Increasing $\mathcal{N}$ sufficiently will cause these fingers to separate from the pool forming droplets as shown in Figure 3.14.

3.5.4 The onset of transverse modes

Following the protocol outlined in Section 3.3.2 we measure $\mathcal{N}_{crit}$ at evenly spaced intervals of 0.05Hz. The stability diagram is complicated and $\mathcal{N}_{crit}$ is larger for smaller f. The stability diagram is shown in Figures 3.16 and 3.17. The stability diagram is divided into two parts: The first for frequencies in the range 1.5Hz to 5Hz and the second for frequencies 5 to 8Hz. Note that Figure 3.16 shows the results of two repeated measurements which were identical. This is not the case in Figure 3.17. Generally the two measurements differed by a small amount. However over the interval $f = 6$Hz to 7Hz measurements

of $\mathcal{N}_{crit}$ were more difficult to perform owing to the difficulty in exciting a transverse mode. So we perform 4 measurements instead of the usual 2.

3.5.5 Hysteresis effects

In our preliminary measurement of the value of $\mathcal{N}$ at various frequencies we observed hysteresis. The estimate of $\mathcal{N}_{crit}$ obtained by increasing $\mathcal{N}$ from zero until a transverse mode was excited was different from the estimate obtained by decreasing $\mathcal{N}$ from a value at which a transverse mode was excited to where it ceased to be observed.

Although we have not performed an in-depth investigation of this phenomenon we have looked at one particular case, $f = 3.4$Hz. For a range of $\mathcal{N}$ close to $\mathcal{N}_{crit}$ we filmed the pool motion at each $\mathcal{N}$ and measured the average pool perimeter P and upper surface area A over a period of 10 seconds. In all cases the pool perimeter does not vary more than 3% so may be regarded as constant. The ratio

$$R = P/\sqrt{A} \tag{3.10}$$

is a therefore a convenient non-dimensional measure of the amplitude of the transverse waves. When no transverse mode is excited, R remains constant regardless of $\mathcal{N}$. Thus $\mathcal{N}_{crit}$ corresponds to the point where R begins to increase as $\mathcal{N}$ increases. Two sets of measurement were performed: one by increasing $\mathcal{N}$; the other by decreasing $\mathcal{N}$ as shown in Figure 3.6. Increasing $\mathcal{N}$ we find $\mathcal{N}_{crit} = 0.105$, but when we decrease $\mathcal{N}$ we find $\mathcal{N}_{crit} = 0.095$. Thus for consistency we measure $\mathcal{N}_{crit}$ by increasing $\mathcal{N}$ for all of our measurements.

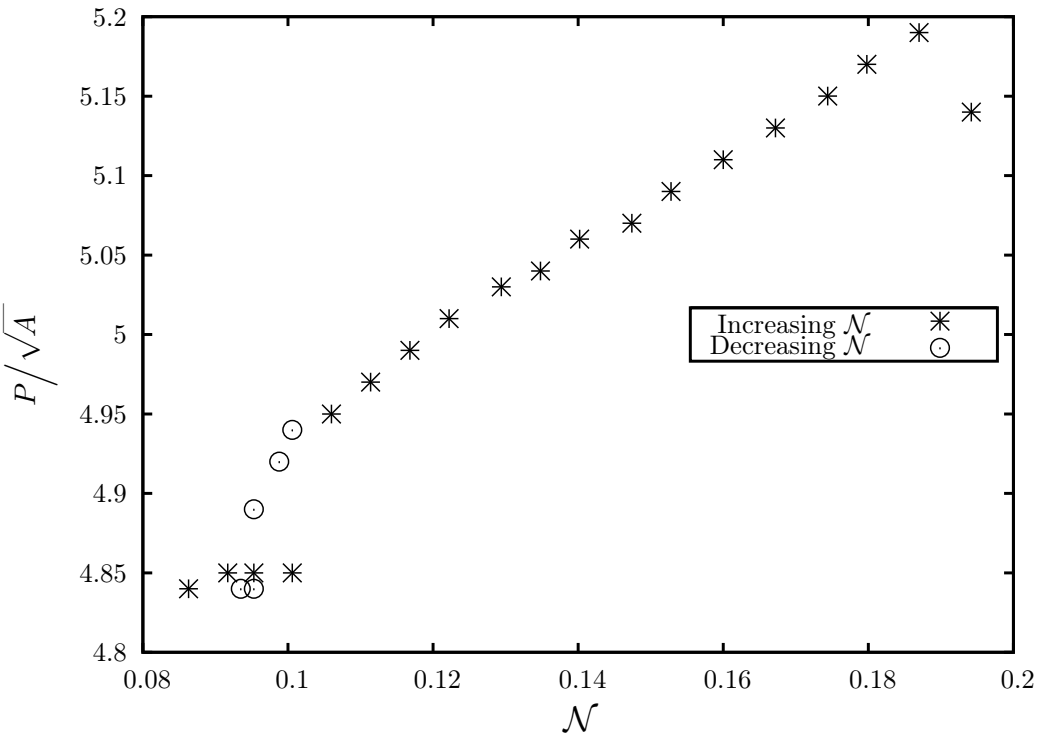

Figure 3.6: Figure demonstrating the hysteresis effects observed in determining $\mathcal{N}_{crit}$. We excite pool motion at various $\mathcal{N}$ using $f = 3.4$Hz. The ratio $P/\sqrt{A}$ is plotted, where P and A are the average pool perimeter and upper surface area respectively. The first series of data is obtained by increasing $\mathcal{N}$ from zero, the second by decreasing $\mathcal{N}$.

Mode	Wavelength λ_m (mm)	Mode	Wavelength λ_m (mm)
3.5S	70.5	8.9V	27.5
4.4V	55.5	8.9S	27.5
4.4S	55.5	9.2S	26.5
5.1V	47.5	9.6V	25.5
5.2S	46.5	10.0S	24.5
6.2V	39.5	10.8V	22.5
6.2S	39.5	11.3V	21.5
6.3S	38.5	11.9V	20.5
7.1S	34.5	11.9S	20.5
8.0V	30.5	12.5V	19.5
8.0S	30.5	13.2V	18.5

Table 3.1: Table of transverse mode wavelengths λ measured from films recording during our experiments using the algorithm presented in section 3.4.

3.6 Wavelengths

We use wavelength λ of an observed transverse mode to name it as explained in Section 3.5.1.1. Using the algorithm explained in Section 3.4 we measure λ of each mode observed. These results are given in table 3.1.

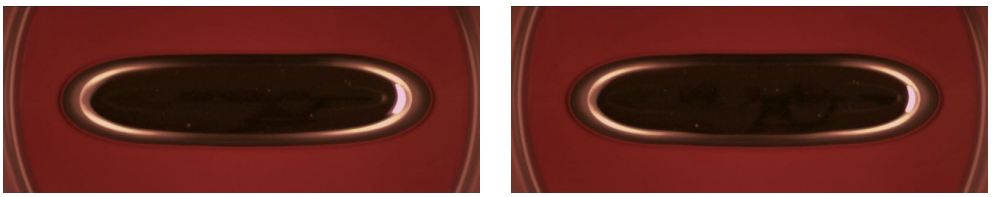

(a) (b)

Figure 3.7: Examples of pool behaviour in the simple regime $f = 4.55\text{Hz}$ $\mathcal{N} = 8.63 \cdot 10^{-2}$. The upper pool surface moves up and down with frequency f while the pool perimeter expands and contracts. Figure 3.7(a) is taken at a time t when the pool perimeter is contracted the most, and figure 3.7(b) is taken half a period of oscillation later when the pool is perimeter is most dilated. Generally these oscillations are small and thus there is little difference between Figures 3.7(a) and 3.7(b).

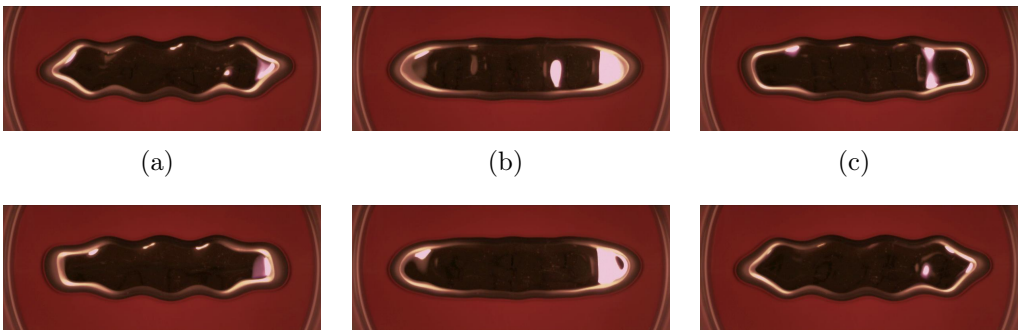

(a) (b) (c)

(d) (e) (f)

Figure 3.8: Examples of pool behaviour observed in the transverse regime $f = 4.55\text{Hz}$, $\mathcal{N} = 2.409 \cdot 10^{-1}$. Indentations form on the pool's perimeter which oscillate perpendicular to the pool's perimeter at frequency $2f$ when $\mathcal{N}$ exceeds $\mathcal{N}_{crit}$. Figures 3.8(a) to 3.8(f) show the progression of the mode $8.9V$ over one period of oscillation.

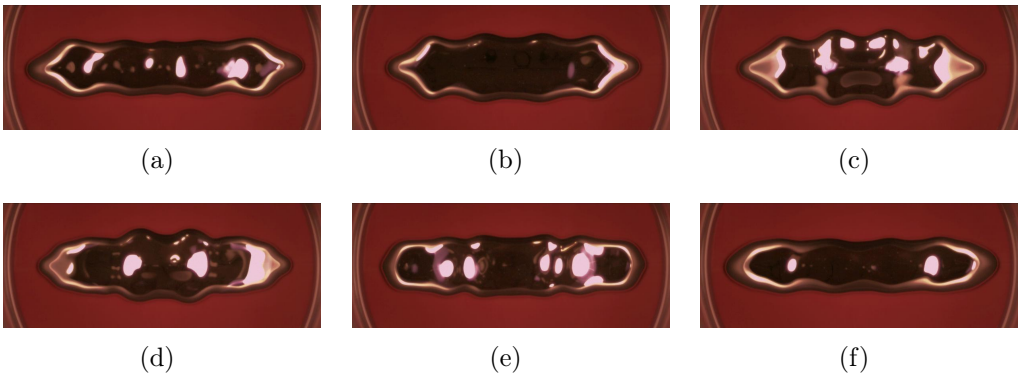

(a) (b) (c)

(d) (e) (f)

Figure 3.9: Examples of pool behaviour observed in the elliptic regime $f = 4.55\text{Hz}$, $\mathcal{N} = 4.73 \cdot 10^{-1}$. Continuing to increase $\mathcal{N}$ beyond $\mathcal{N}_{crit}$ we observe a transverse mode oscillating at f with a superimposed lower frequency elliptic deformation. As the indentations oscillate perpendicular to the pool's perimeter the pool's ends squeeze in and out as its width grows and shrinks.

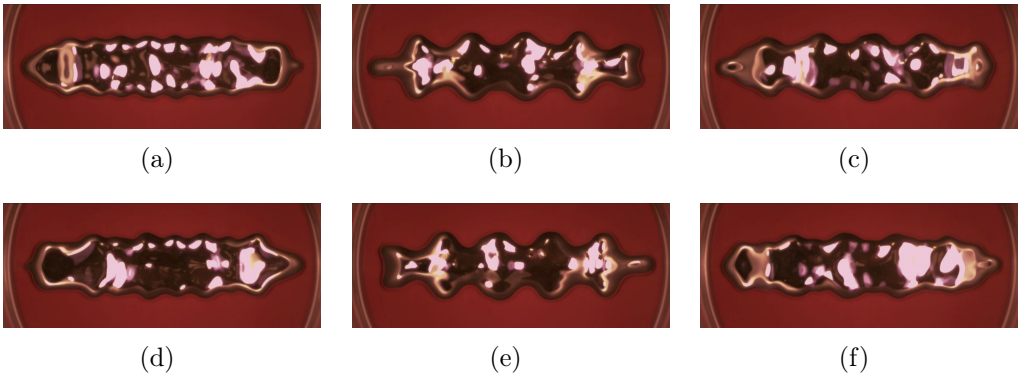

(a) (b) (c)

(d) (e) (f)

Figure 3.10: Examples of pool behaviour observed in the mixed regime $f = 4.55\text{Hz}$, $\mathcal{N} = 6.19 \cdot 10^{-1}$. Continuing to increase $\mathcal{N}$, the elliptic deformation stops and the only transverse deformation is observed. Multiple modes appear to be excited however. We observe that the number and spacing of indentations on the pool's perimeter changes. In Figures 3.10(b), 3.10(c) and 3.10(e) we observe the same number of indentations which are roughly regularly spaced around the pool perimeter. In Figures 3.10(a), 3.10(d) and 3.10(f) we observe more indentations and their spacing is no longer regular.

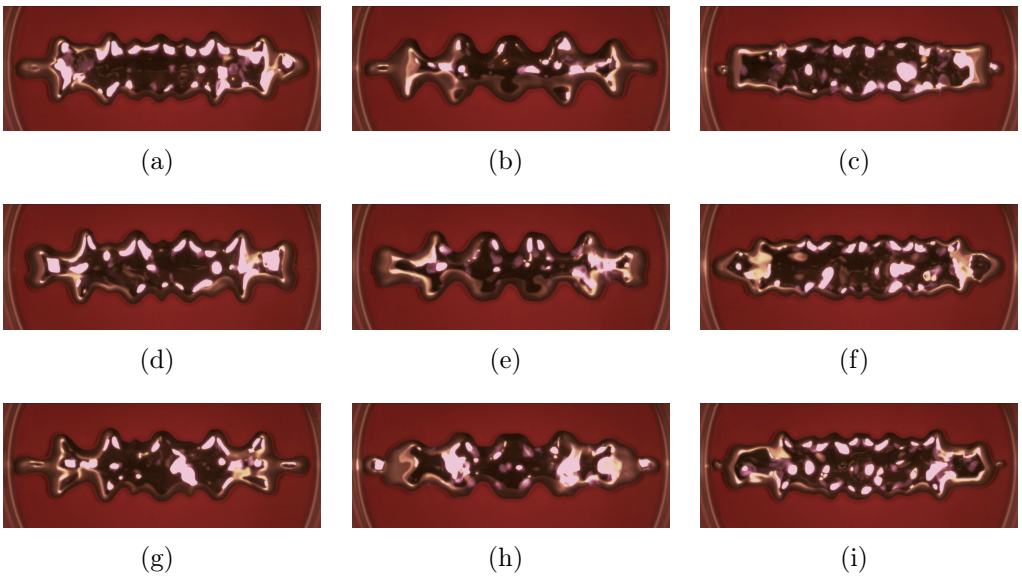

(a) (b) (c)

(d) (e) (f)

(g) (h) (i)

Figure 3.11: Examples of pool behaviour observed in the mixed regime: $f = 4.55\text{Hz}$, $\mathcal{N} = 9.66 \cdot 10^{-1}$. As $\mathcal{N}$ increases we still observe that the pool motion is primarily azimuthal, but the more complicated forms are observed and the number of indentations varies more as shown in Figures 3.11(a) to 3.11(i).

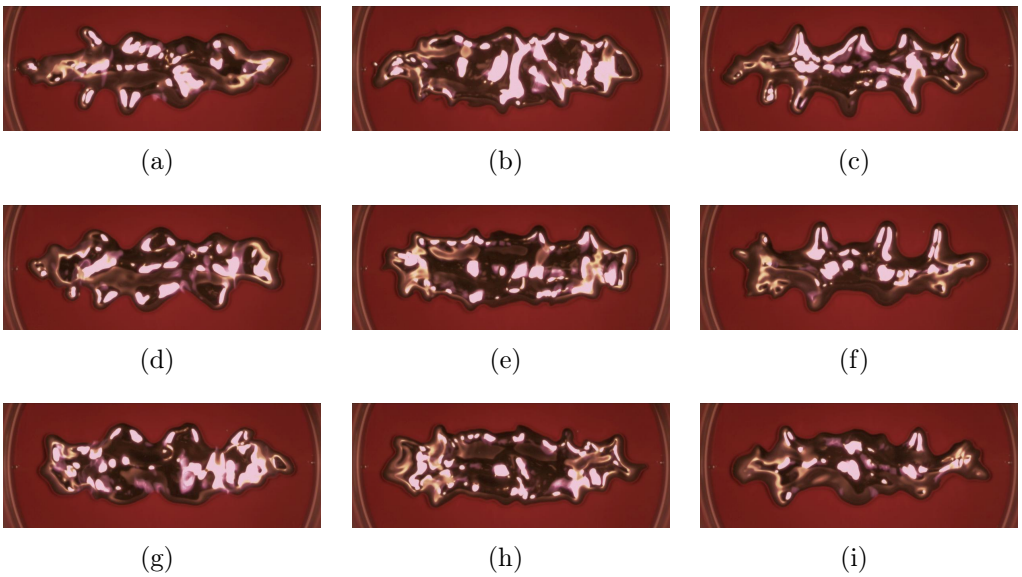

(a) (b) (c)

(d) (e) (f)

(g) (h) (i)

Figure 3.12: Examples of pool behaviour observed in the chaotic regime: $f = 4.55\text{Hz}$, $\mathcal{N} = 1.6327$. Further increase in the value of $\mathcal{N}$ causes the symmetric transverse oscillations to degenerate into more complicated chaotic forms as shown in Figures 3.12(a) to 3.12(i). Indentations still appear on the pool perimeter as shown in Figures 3.12(a), 3.12(c) and 3.12(f), they are however not distributed evenly and their amplitude is much larger tending to form thin finger like shapes.

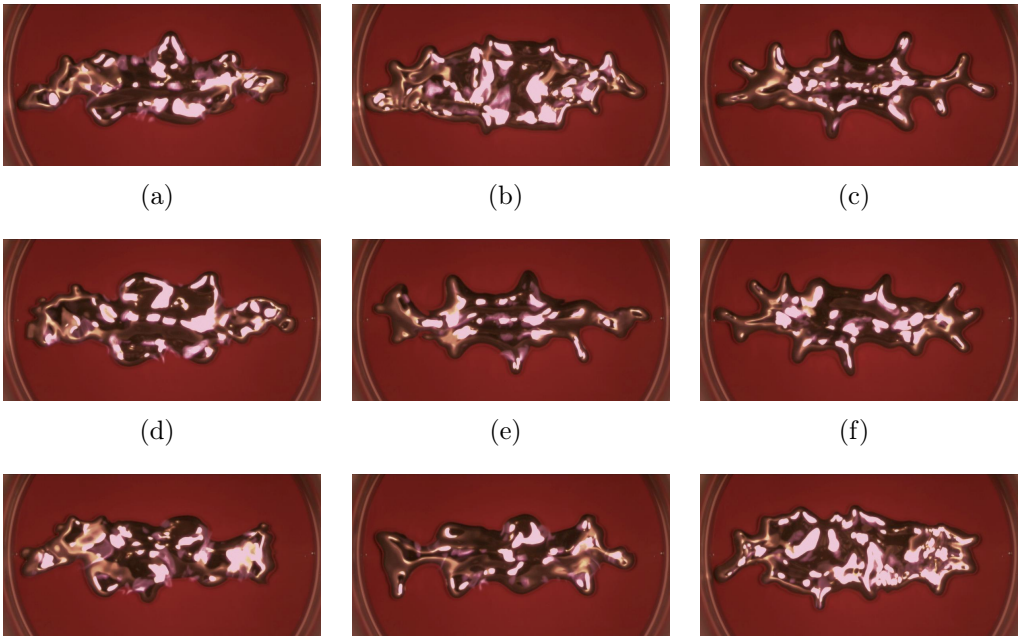

(a) (b) (c)

(d) (e) (f)

(g) (h) (i)

Figure 3.13: Examples of pool behaviour observed in the chaotic regime: $f = 4.55$Hz, $\mathcal{N} = 2.1739$. The Lorentz force starts to dominate pool behaviour causing large chaotic deformations to appear. Close to separating from the pool, the finger like deformations become thinner and longer as shown in Figures 3.13(c), 3.13(e) and 3.13(e).

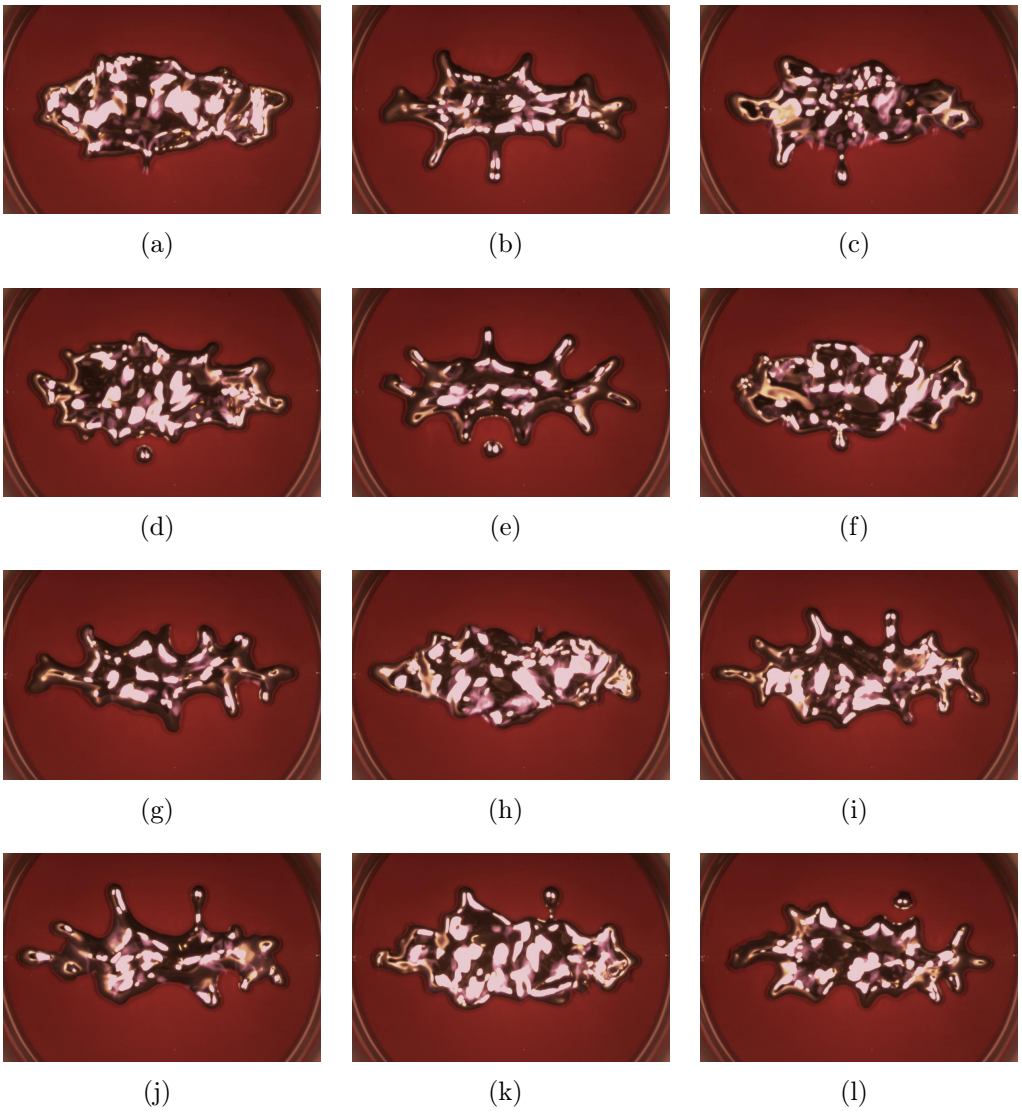

Figure 3.14: Two examples of droplet separation; the first is illustrated in Figures 3.14(a) through 3.14(f); the second in 3.14(g) through 3.14(l). Both were observed when $f = 4.55$Hz, $\mathcal{N} = 2.4742$. The Lorentz force dominates pool behaviour imparting enough kinetic energy to the liquid metal to allow droplets overcome surface tension and separate from the pool. A "finger" forms (see Figures 3.14(g) to 3.14(i), 3.14(a) and 3.14(b)) which is elongated by the fluid motion. As the finger lengthens, it's "base"; i.e. the point at which it joins the pool, becomes thinner as the fingers "head" is propelled away from the pool. This is shown in Figures 3.14(c), 3.14(k) and 3.14(l). The head then separates from the pool to form a droplet as shown in Figures 3.14(d), 3.14(e) and 3.14(l).

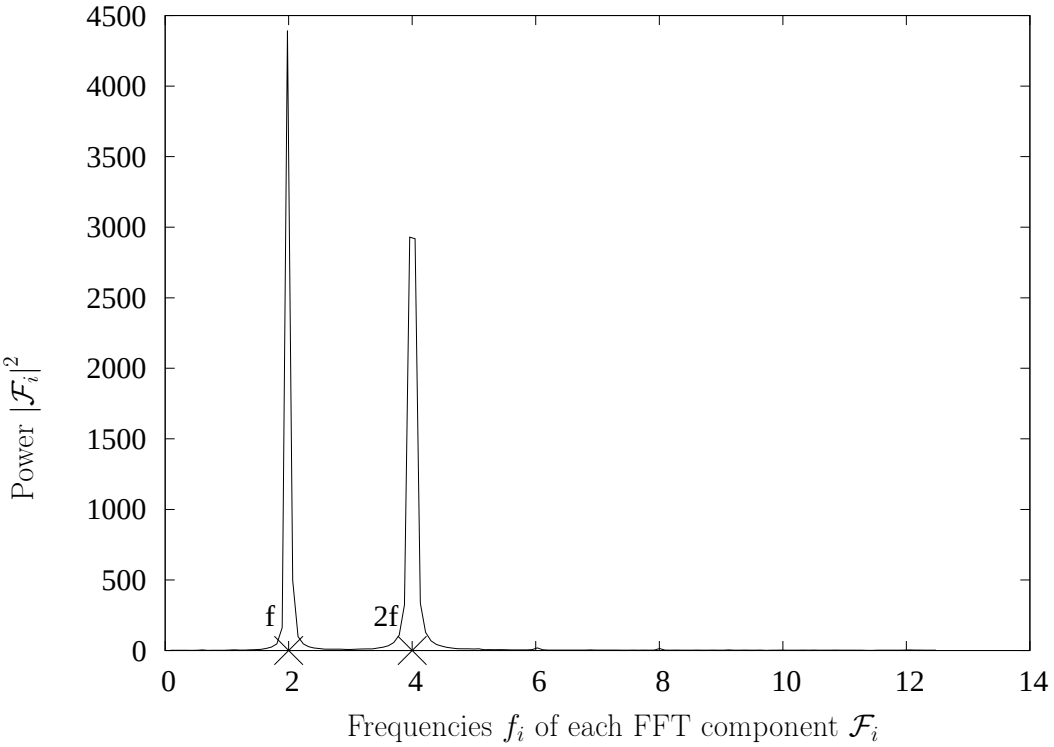

(a) Power spectrum of the 4.4S mode.

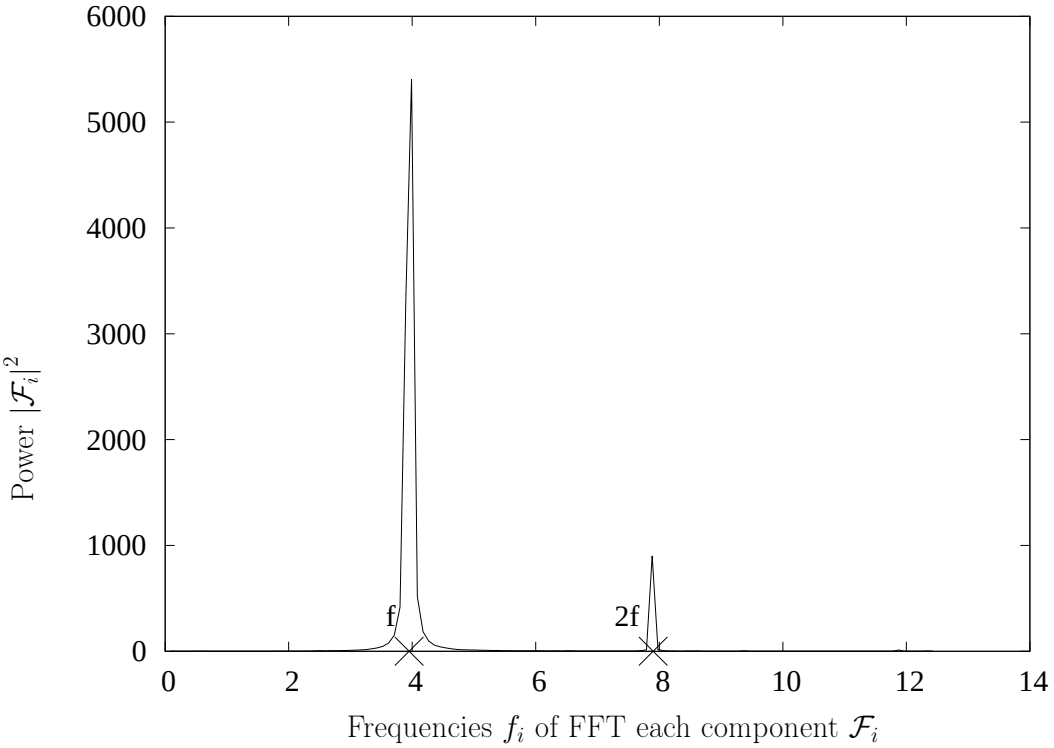

(b) Power spectrum of the 8S mode.

Figure 3.15: Power spectra of two modes: 4.4S and 8S. These are calculated by taking the FFT $\mathcal{F}$ in time of each point

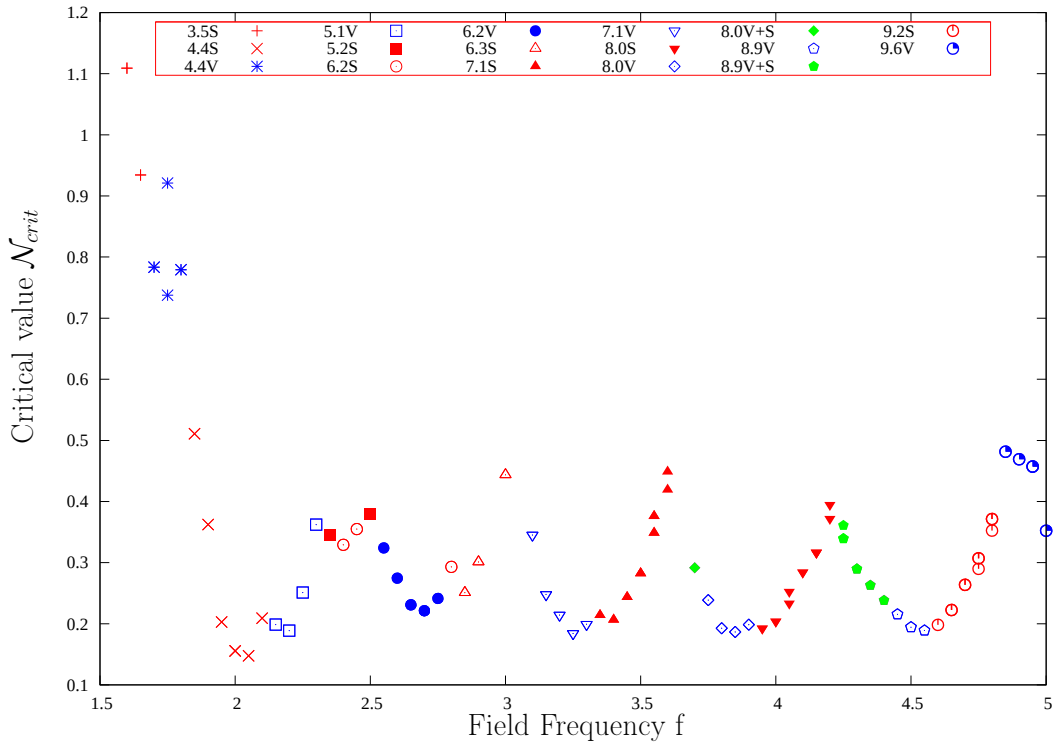

Figure 3.16: Stability diagram over the interval $f = 1.5$Hz to 5Hz. Plot shows the critical value $\mathcal{N}_{crit}$ at which a transverse mode is first observed. The symbols used denote the transverse mode observed, 9.6V denotes the varicose (V) mode with ratio $m = 9.6$. A key for these symbols is shown at the top of the graph. Note that varicose (V) modes are *blue* and sinuous (S) modes are *red*. Points where combined varicose and sinuous deformation was observed are denoted V+S and are *green*.

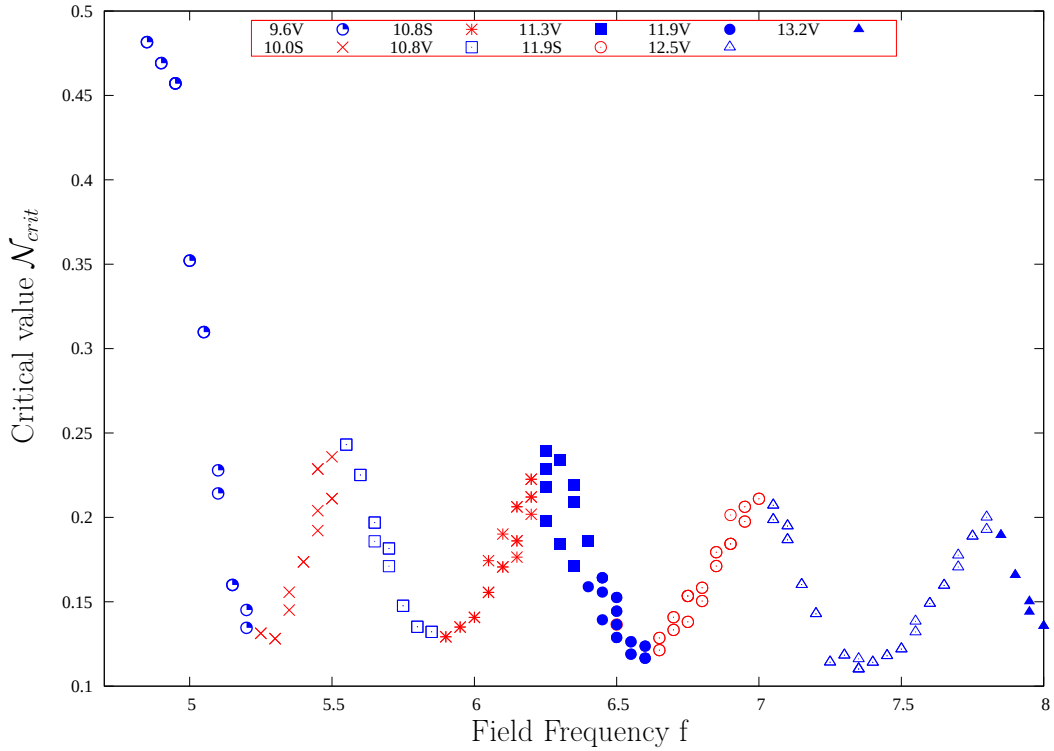

Figure 3.17: Stability diagram over the interval $f = 5$Hz to 8Hz. Plot shows the critical value $\mathcal{N}_{crit}$ at which a transverse mode is first observed. The symbols used denote the azimuthal mode observed, 9.6V denotes the varicose (V) mode with ratio $m = 9.6$. A key for these symbols is shown at the top of the graph. Note that varicose (V) modes are *blue* and sinuous (S) modes are *red*.

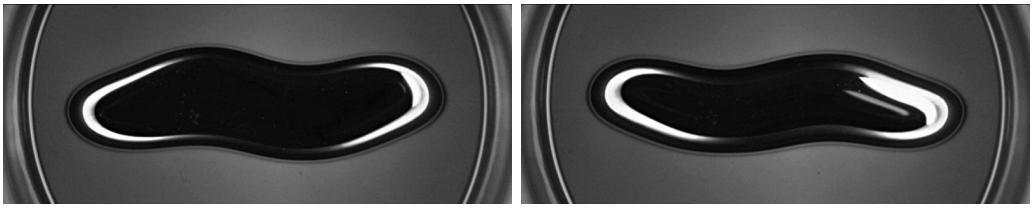

(a) 3.5S $f = 1.6$Hz, $\mathcal{N} = 1.109$

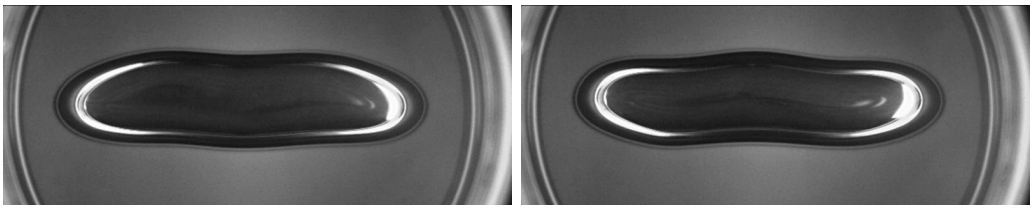

(b) 4.4S $f = 2$Hz, $\mathcal{N} = 1.56 \cdot 10^{-1}$

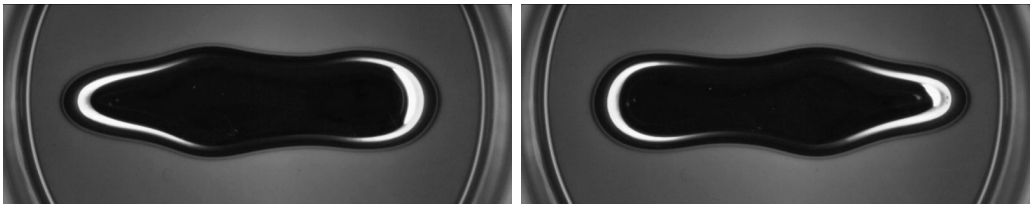

(c) 4.4V $f = 1.7$Hz, $\mathcal{N} = 7.85 \cdot 10^{-1}$

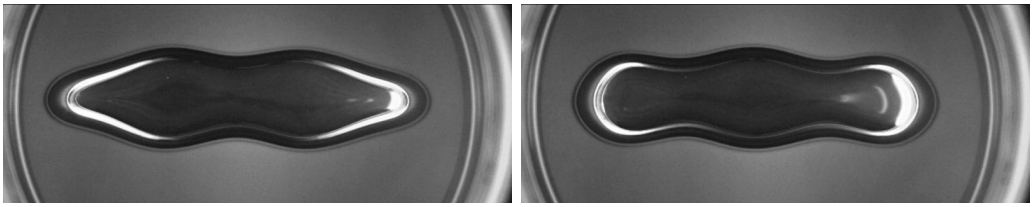

(d) 5.1V $f = 2.15$Hz, $\mathcal{N} = 2.09 \cdot 10^{-1}$

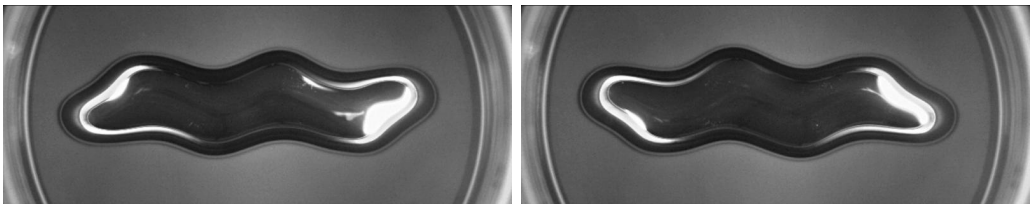

(e) 5.2S $f = 2.35$Hz, $\mathcal{N} = 3.45 \cdot 10^{-1}$

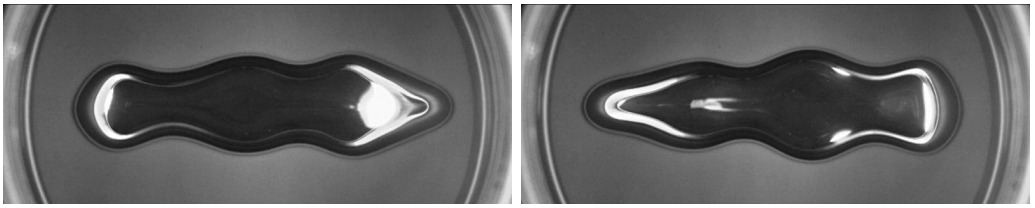

(f) 6.2V $f = 2.55$Hz, $\mathcal{N} = 3.24 \cdot 10^{-1}$

Figure 3.18: Example images of transverse modes observed. Photos of modes 3.5S, 4.4S, 4.4V, 5.1V, 5.2S and 6.2V are shown above.

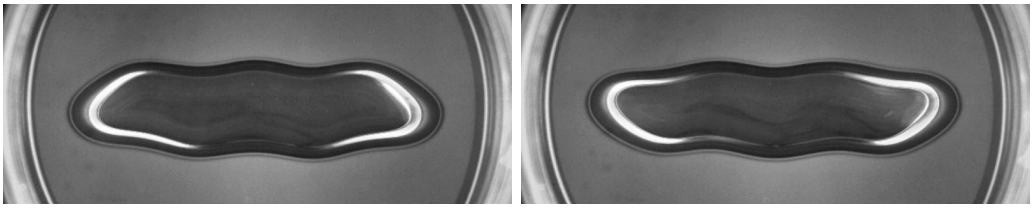

(a) 6.2S $f = 2.4$Hz, $\mathcal{N} = 3.29 \cdot 10^{-1}$

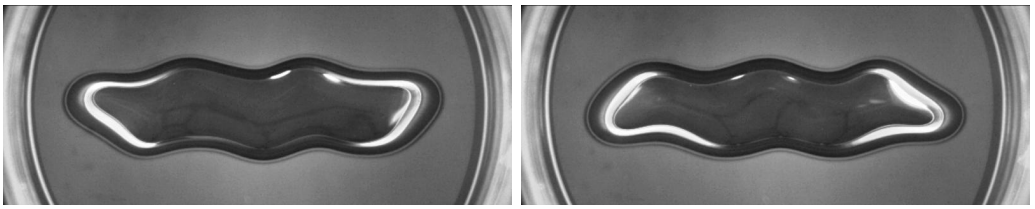

(b) 6.2S $f = 2.4$Hz, $\mathcal{N} = 3.29 \cdot 10^{-1}$

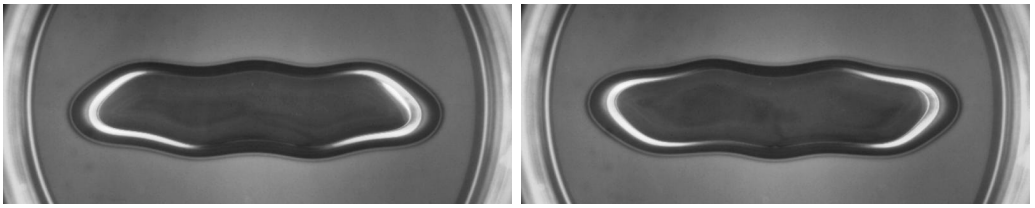

(c) 6.3S $f = 2.4$Hz, $\mathcal{N} = 3.29 \cdot 10^{-1}$

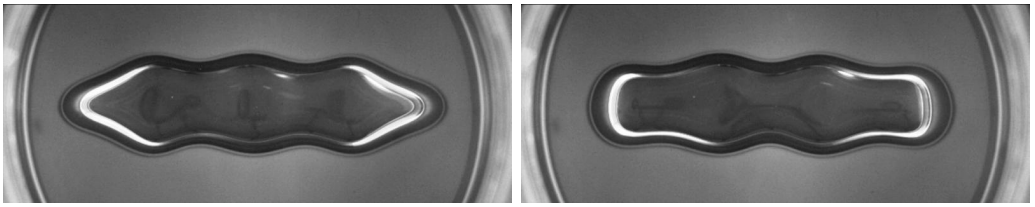

(d) 7.3V $f = 3.15$Hz, $\mathcal{N} = 2.48 \cdot 10^{-1}$

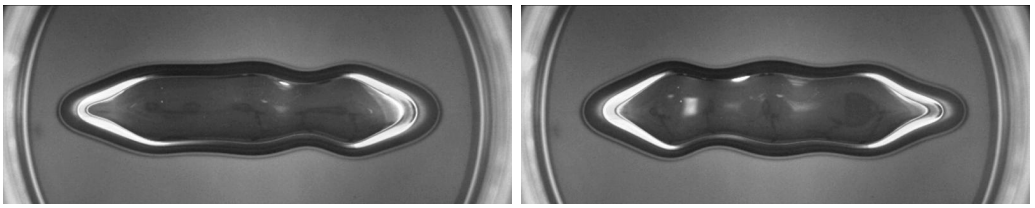

(e) 7.3V $f = 3.15$Hz, $\mathcal{N} = 2.48 \cdot 10^{-1}$

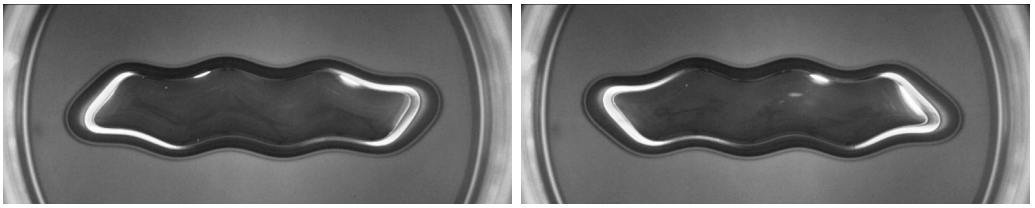

(f) 7.1S $f = 3.35$Hz, $\mathcal{N} = 2.14 \cdot 10^{-1}$

Figure 3.19: Example images of transverse modes observed. Photos of modes 6.2S, 6.3S, 7.3V and 7.1S are shown above.

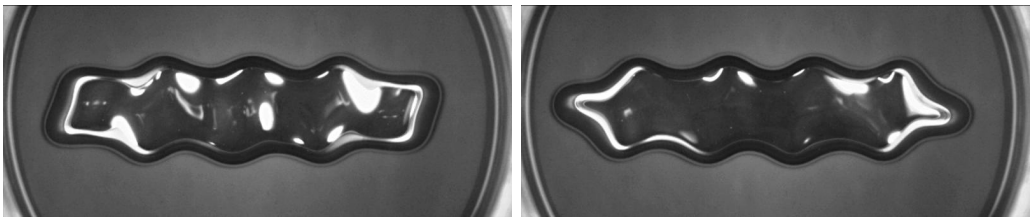

(a) 8.0S $f = 3.95$Hz, $\mathcal{N} = 1.92 \cdot 10^{-1}$

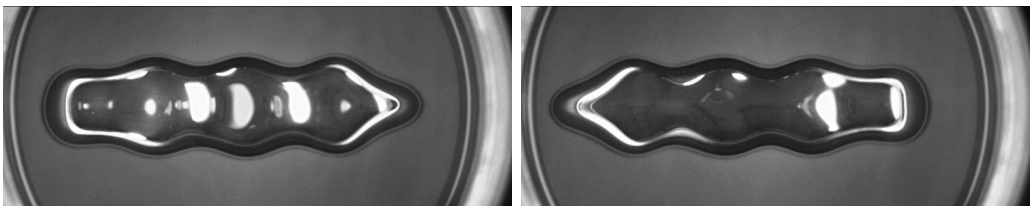

(b) 8.0V $f = 3.75$Hz, $\mathcal{N} = 2.39 \cdot 10^{-1}$

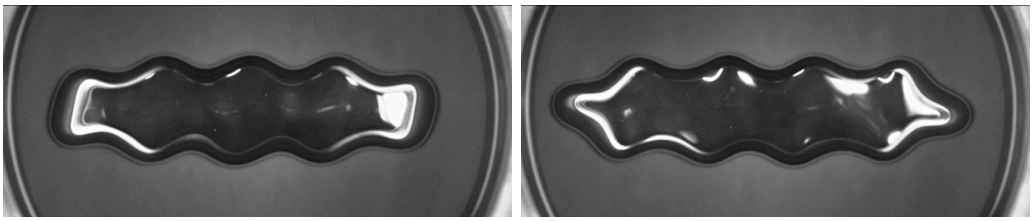

(c) 8.9 $f = 4.3$Hz, $\mathcal{N} = 2.90 \cdot 10^{-1}$

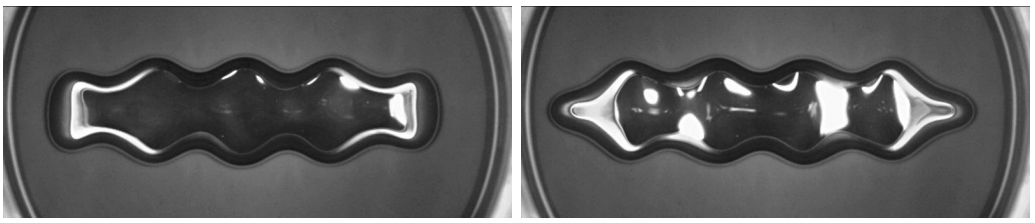

(d) 8.9 $f = 4.3$Hz, $\mathcal{N} = 2.90 \cdot 10^{-1}$

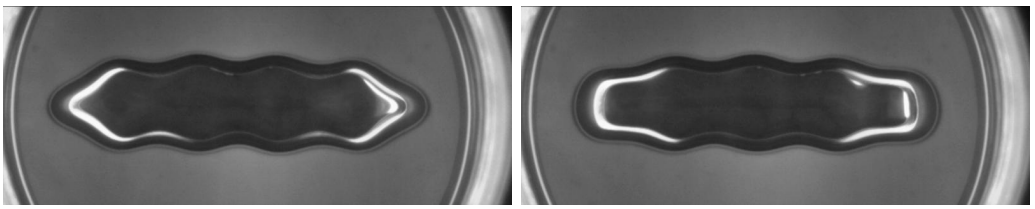

(e) 8.9V $f = 3.75$Hz, $\mathcal{N} = 2.39 \cdot 10^{-1}$

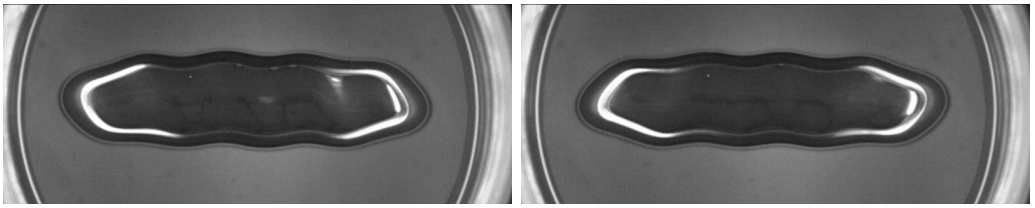

(f) 9.2S $f = 4.6$Hz,$\mathcal{N} = 1.98 \cdot 10^{-1}$

Figure 3.20: Example images of transverse modes observed. Photos of modes 8.0S, 8.0V, 8.9, 8.9V and 9.2S are shown above.

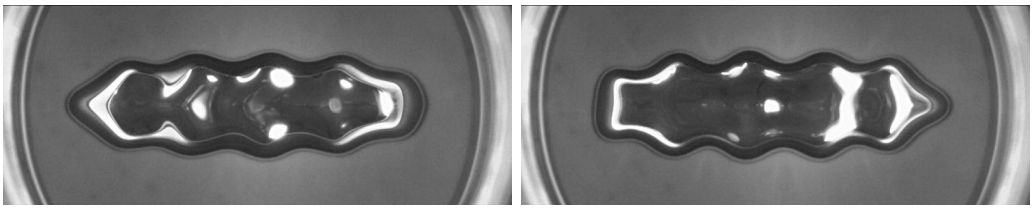

(a) 9.6V $f = 4.95$Hz, $\mathcal{N} = 4.57 \cdot 10^{-1}$

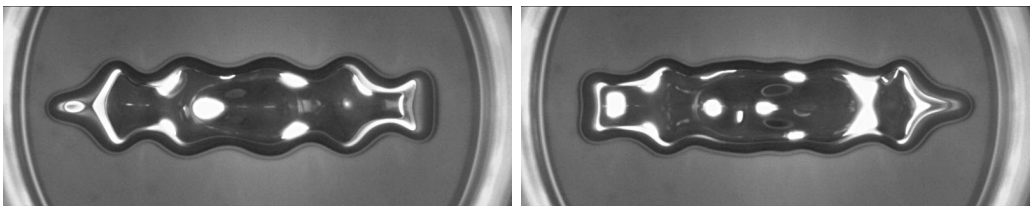

(b) 9.6V $f = 4.95$Hz, $\mathcal{N} = 4.57 \cdot 10^{-1}$

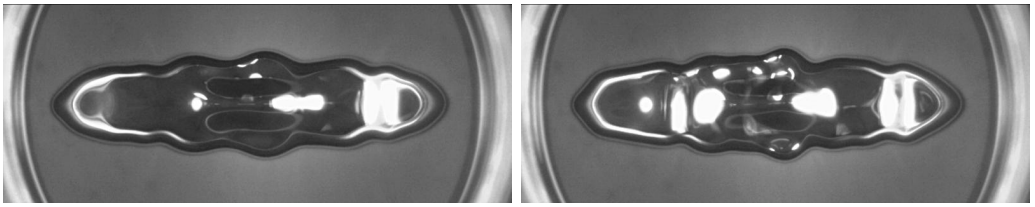

(c) 9.6V $f = 4.95$Hz, $\mathcal{N} = 4.57 \cdot 10^{-1}$

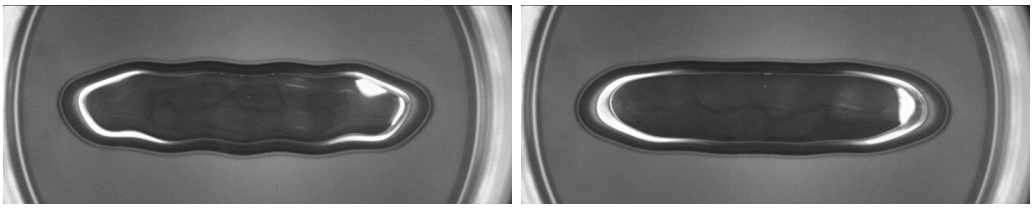

(d) 10.0S $f = 5.3$Hz, $\mathcal{N} = 1.28 \cdot 10^{-1}$

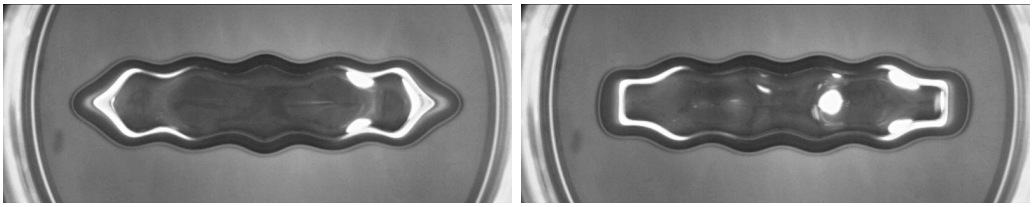

(e) 10.8V $f = 5.75$Hz, $\mathcal{N} = 1.47 \cdot 10^{-1}$

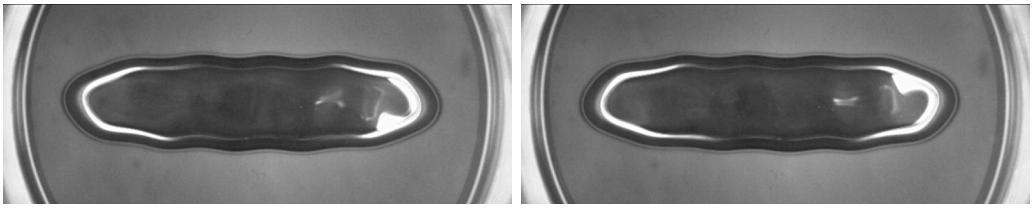

(f) 10.8S $f = 6$Hz, $\mathcal{N} = 1.41 \cdot 10^{-1}$

Figure 3.21: Example images of transverse modes observed. Photos of modes 9.6V and 10.0S are shown above.

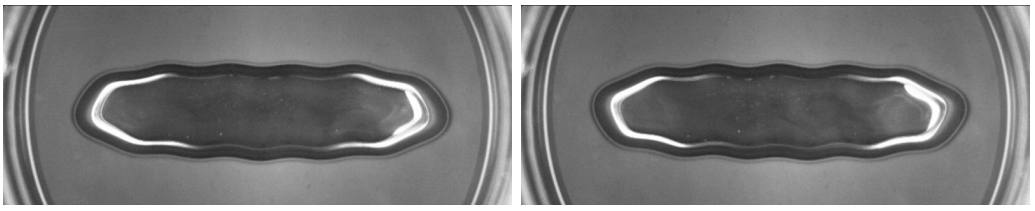

(a) 11.9S $f = 6.65$Hz, $\mathcal{N} = 1.21 \cdot 10^{-1}$

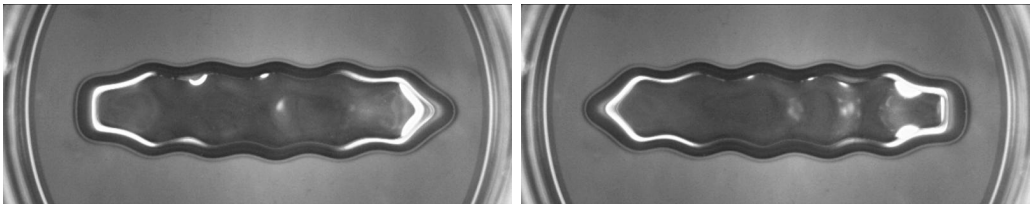

(b) 11.9V $f = 6.5$Hz, $\mathcal{N} = 1.29 \cdot 10^{-1}$

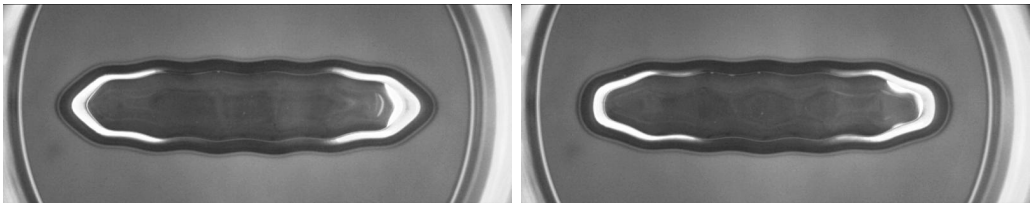

(c) 12.5V $f = 7.4$Hz $\mathcal{N} = 1.14 \cdot 10^{-1}$

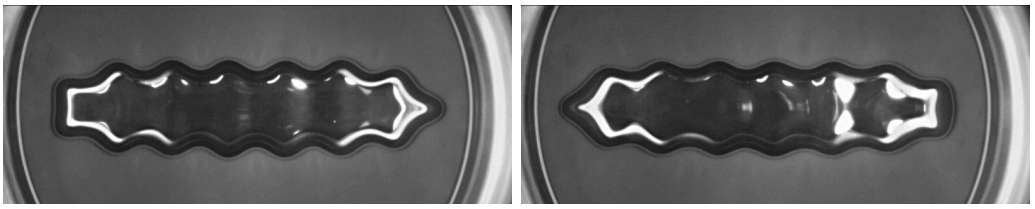

(d) 13.2V $f = 7.85$Hz, $\mathcal{N} = 1.89 \cdot 10^{-1}$

Figure 3.22: Example images of transverse modes observed. Photos of modes 11.9S, 11.9V, 12.5V and 13.2V are shown above.

Chapter 4

Theoretical investigation of free surface parametric instabilities of a strip of liquid metal excited by low frequency magnetic field

4.1 Introduction

In this chapter we attempt to interpret our results from the "strip" experiment (Chapter 3)) using our Lagrangian theory. We wish to understand the behaviour of the transverse modes. In particular we derive a model for the basic mechanism responsible for the formation of transverse modes. We begin by outlining the simplified geometry used to model both varicose (V) and sinuous (S) modes. We then proceed to use our Lagrangian approach to derive a model for the coupled behaviour of the transverse and simple oscillations of the pool. We then compare the stability diagrams obtained theoretically to those obtained experimentally, and we find reasonable qualitative agreement for a number of transverse modes.

4.2 Mathematical model

The experiments were performed using a liquid metal alloy in the presence of a uniform vertical alternating magnetic field:

$$\mathbf{B} = B_0 \sin(2\pi f t)\widehat{\mathbf{z}}, \tag{4.1}$$

where B_0 is the magnetic field amplitude, $\widehat{\mathbf{z}}$ a vertical unit vector and f the magnetic field frequency. In the experiments two types of transverse mode, varicose (V) and sinuous (S) were observed. The geometry of a V mode is shown in Figure 4.1 and that of an S mode in Figure 4.2. Note that we ignore the end effects and assume for simplicity that the pool extends indefinitely along the x axis and thus we only need consider a wavelength section $0 \leq x \leq \ell$. For further details on the experimental geometry see Chapter 3.

We assume that the sides of the pool remain straight and parallel to the z axis, and its height $h(t)$ is uniform but time dependant. The pool surface is considered to be plane and horizontal. This is confirmed experimentally as the pool width is considerably larger than its depth, the width being 30mm and

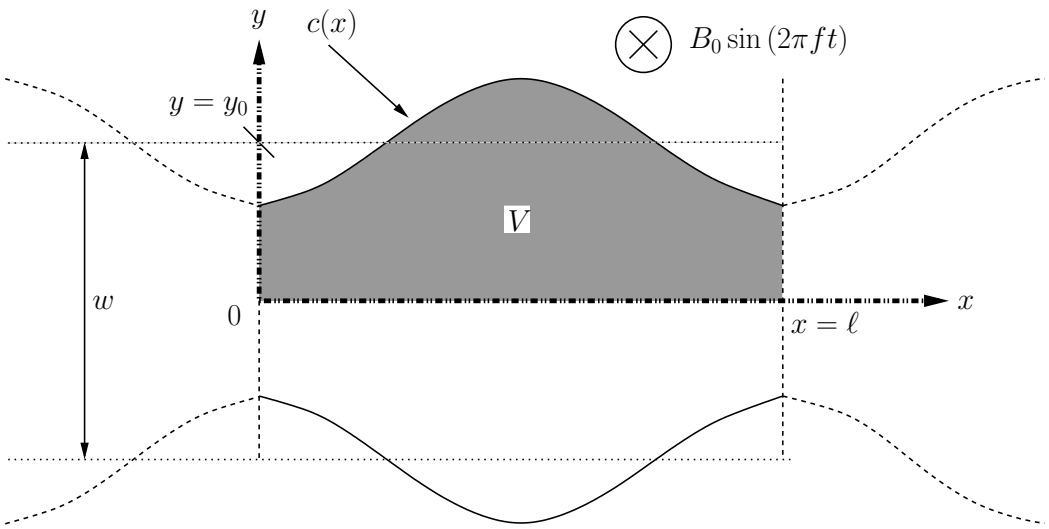

(a) View from above of a V mode.

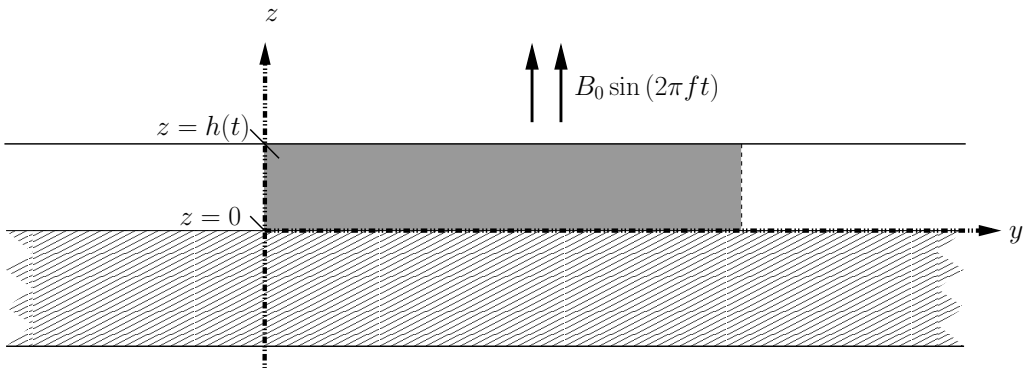

(b) View from the side of a V mode.

Figure 4.1: Views from above and the side of the geometry of a V mode. The z axis is vertical and the x and y axes lie in the horizontal plane perpendicular to z. The pool's upper and lower surfaces are horizontal as shown, the pool has a uniform depth h and the pool's edge at $y = c(x)$ is vertical. The volume enclosed is denoted by $\mathcal{V}$.

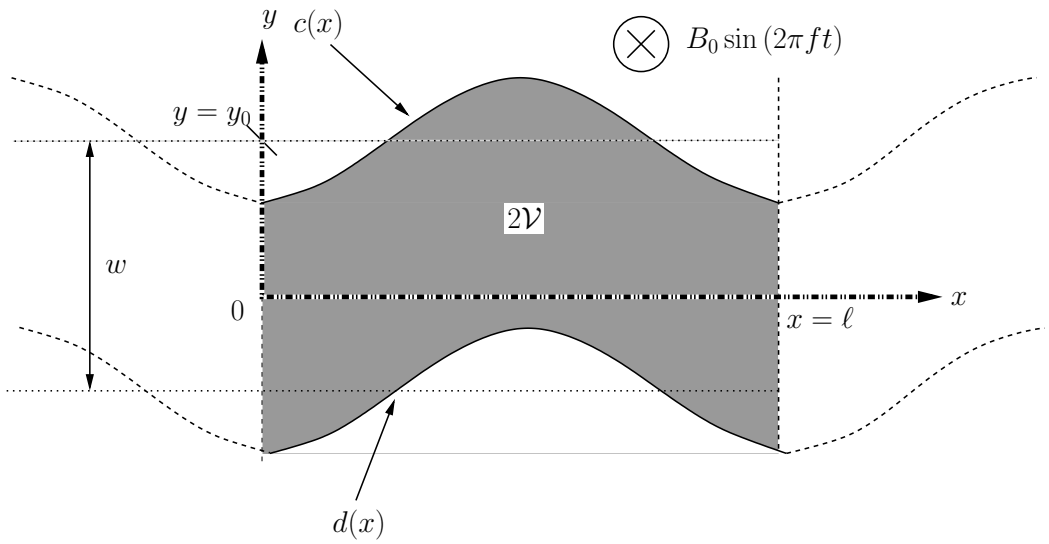

(a) View from above of a S mode.

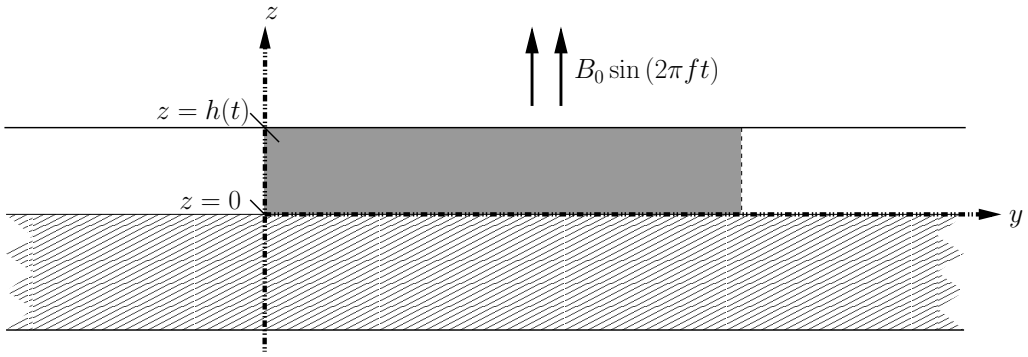

(b) View from side of a S mode.

Figure 4.2: Views from above and the side of the geometry of a S mode. The z axis is vertical and the x and y axes lie in the horizontal plane perpendicular to z. The pool's upper and lower surfaces are horizontal as shown above, the pool has a uniform depth h, and the pool's edges at $y = c(x)$ and $y = d(x)$ are vertical. The volume enclosed is denoted by $2\mathcal{V}$.

its depth being approximately 6mm. As the derivation for the V and S modes is quite similar, we will derive only the V mode theory in detail and outline the minor changes required to consider an S mode in section 4.3.

We define a mean pool width $w(t)$

$$w(t) = \frac{1}{\ell}\int_{x=0}^{\ell} 2c(x)\mathrm{d}x. \tag{4.2}$$

To simplify the analysis we ignore the complicated end effects and assume that the pool continues on indefinitely along both directions of the x axis. We suppose the straight edge of the pool is perturbed by a transverse wave of mode number k say, so that the equation of the pool edge close to $y = y_0$ is given by:

$$y = c(x) = y_0(t) - \epsilon b(t)\cos(kx) \tag{4.3}$$

where the angular wave number

$$k = \frac{2\pi}{\ell}, \tag{4.4}$$

the wave amplitude is given by $\epsilon b(t)$ and ϵ is a small parameter.

It then follows from 4.2 that the pool width $w(t)$ is simply:

$$w(t) = 2y_0(t). \tag{4.5}$$

As the geometry is symmetric about the x axis we need consider only the pool volume $\mathcal{V}$ enclosed between the x axis and $c(y)$:

$$\mathcal{V} = \int_{z=0}^{h(t)}\int_{x=0}^{\ell}\int_{y=0}^{c(y)} \mathrm{d}y\mathrm{d}x\mathrm{d}z = \ell y_0(t)h(t), \tag{4.6}$$

which is the area shaded grey in Figure 4.1.

As $\mathcal{V}$ is constant this allows up to write y_0 as:

$$y_0(t) = \frac{k\mathcal{V}}{2\pi h(t)}. \tag{4.7}$$

We now derive a mathematical model of a simple mode and a *single* transverse mode. The simple mode is characterised by vertical oscillations in pool height h, while the pool width w contracts and expands to conserve pool volume $\mathcal{V}$. The transverse mode is characterised by an instability leading to rapid growth in b, the amplitude of a Fourier mode on the pool edge $y = y_0$.

As in Chapter 2 where we consider the starfish problem, we ignore the complicated fluid dynamics and characterise the system in terms of two generalised co-ordinates: h and b. We then derive a Lagrangian

$$L = T - E_g - E_s - E_m, \tag{4.8}$$

for the system and solve using Lagrange's equations. Here T, E_g, E_s and E_m are the kinetic, gravitational, surface tension and magnetic energies of the pool.

To justify the approximations used in our model we now discuss various dimensionless parameters. We then proceed to show that damping is minor and may be ignored in this preliminary investigation.

4.2.1 Dimensionless parameters

The equilibrium shape of the pool is defined by a balance between the surface tension force and the gravitational body force. The gravitational Bond number

$$Bo_g = \frac{\rho g \ell w}{\gamma} = 420 \tag{4.9}$$

expresses the ratio of these forces. Here ℓ and w are the pools lengths and width at rest as measured in Chapter 3. This value is moderately large, thus we may consider that the pool surface to be plane and horizontal. The pool depth h_0 at rest may be estimated in terms of the capillary length ℓ_c (Paddey [1969]) ,

$$h_0 \approx 2\ell_c, \text{ where } \ell_c = \sqrt{\frac{\gamma}{\rho g}}. \tag{4.10}$$

Here γ, ρ and are the surface tension and density of Ga-In-Sn. The experimentally measured value of h_0 is 5.2mm and $2\ell_c = 5.85$mm.

The electromagnetic forces tend to cause the pool perimeter to contract and expand while the surface tension and gravitational forces tend to restore the pool to its equilibrium shape, while fluid inertia tends to slow the pool oscillations. The ratio of electromagnetic and inertial forces is given by the magnetic interaction parameter

$$\mathcal{N} = \frac{\sigma B^2}{2\pi f \rho},$$

where f is the magnetic field frequency. The values of $\mathcal{N}_{crit}$ for the starfish experiment are an order of magnitude greater than those for the onset of transverse modes indicating that the latter are more easily excited.

4.2.2 Boundary layers and viscous friction

Due to the low kinematic viscosity of Ga-In-Sn, we may assume that the main contribution to viscous friction arises from vertical gradients of the horizontal velocity. Under the usual boundary layer assumptions we estimate the boundary layer depth using the classical expression (see Batchelor [1967]),

$$\delta_\nu = \sqrt{\nu/2\pi f}, \tag{4.11}$$

where ν is the kinematic viscosity of Ga-In-Sn. When $\mathcal{N}$ is large, the Lorenz force balances the viscous term and we may expect the development of a Hartmann layer. The Hartmann number defined by

$$Ha^2 = \frac{2\pi f h^2}{\nu}$$

is moderately large, $Ha \approx 30$. Thus we may expect the development of a Hartmann type boundary layer along the bottom wall. The expression for the

boundary-layer thickness δ_B(Moreau [1990]) is

$$\delta_B = \frac{1}{B_0}\sqrt{\frac{\rho\nu}{\sigma}}, \tag{4.12}$$

which can be written in the form

$$\delta_B = \delta_\nu/\sqrt{\mathcal{N}} \tag{4.13}$$

using (4.11) and (4.12). Thus the Hartmann layer thickness is comparable to the viscous boundary layer thickness in both experiments. The viscous boundary layer depth δ_ν is of order 10^{-3}mm as is the value of δ_B. These are much smaller than pool depth h. This is not surprising as the Reynolds number

$$Re = \frac{2\pi f a h}{\nu}$$

is large and of order 10^4. Viscous effects remain weak near the edge of the pool meniscus as the capillary number

$$Ca = \frac{\rho\nu U}{\gamma}$$

is small, of $O(10^{-3})$. Note that $U = 2\pi f w$ is a typical meniscus velocity. Thus viscous forces and electromagnetic damping play only a small role in determining the pool dynamics. Therefore we may approximate the flow in terms of a potential ϕ.

4.2.3 Gravitational and surface tension energies

Neglecting the edge contribution to surface tension, the surface tension and gravitational potential energy are trivial to derive:

$$E_\gamma + E_{grav} = \mathcal{V}\left(\frac{2\gamma}{h} + \frac{\rho g h}{2}\right). \tag{4.14}$$

Minimising the energy above with respect to h gives us the following estimate of the rest height (c.f. equation (4.10))

$$h_0 = 2\sqrt{\gamma/\rho g}. \tag{4.15}$$

However, to compute E_γ to order ϵ^2 we must include the contribution of the edge:

$$E_{edge} = \gamma h \int_0^\ell \sqrt{1 + c'(x)^2}\,\mathrm{d}x = \gamma h \left(\ell + \frac{\pi}{2}\epsilon^2 b^2 k\right). \tag{4.16}$$

4.2.4 Non-dimensionalisation

Throughout the rest of this chapter we will use primes h', b' etc to denote variables which have been non-dimensionalised with respect to the length scale h_0 and time scale $\sqrt{h_0/g}$. Here h_0 is given by expression 4.15.

Writing the total gravitational and surface tension energy in non-dimensional variables:

$$E = \mathcal{V}'\frac{1}{2}(1/h' + h') + \frac{1}{4}\mathcal{V}'h'(\ell' + \frac{\pi}{2}\epsilon^2 k' b'^2). \tag{4.17}$$

4.2.5 Electromagnetic energy

As in the starfish experiment, the screen parameter

$$R_\omega = 2\pi\nu\sigma f h^2 \tag{4.18}$$

is small, typically $\mathrm{O}(10^{-3})$. Thus the applied magnetic field $\mathbf{B}$ is unaffected by the pool. As shown in 2.2.3, the electromagnetic force may be written in terms of a torsion function τ as:

$$\boldsymbol{F} = \boldsymbol{J} \times \mathbf{B} = \pi f \sigma \rho B_0^2 \sin(4\pi f t)\nabla\tau \tag{4.19}$$

where $\tau[x, y]$ is the torsion function for the shaded region in Figure 4.1, and is defined by:

$$\nabla^2\tau[x, y] = -1, \qquad \tau[x, 0] = 0, \tag{4.20}$$

and

$$\tau[x, c(x)] = 0. \tag{4.21}$$

We expand τ in the form,

$$\tau = \tau_0 + \epsilon\tau_1 + \epsilon^2\tau_2 + \ldots + \epsilon^m\tau_m \ldots$$

Clearly we can take,

$$\tau_0 = -\frac{1}{2}y^2 \tag{4.22}$$

at zero order. Taking a Taylor expansion in ϵ, we may write the boundary condition (4.21) as

$$\begin{aligned}\tau[x, c(x)] = &-\frac{1}{2}y_0^2 - \epsilon y_0 b\cos(kx) - \frac{1}{2}\epsilon^2 b^2\cos^2(kx) \\ &+ \epsilon\tau_1[x, y_0] + \epsilon^2\tau_{1,y}[x, y_0]b\cos(kx) + \epsilon^2\tau_2[x, y_0] + \ldots, \\ = &\ 0\end{aligned} \tag{4.23}$$

where $\tau_{1,y}$ denotes $\partial\tau_1/\partial y$ etc. Considering $O(\epsilon)$ terms we see that τ_1 must satisfy:

$$\nabla^2\tau_1 = 0, \qquad \tau_1[x, y_0] = y_0 b\cos(kx), \qquad \text{and} \qquad (\tau_{1,y})_{y=0} = 0$$

by symmetry. The solution is

$$\tau_1 = \frac{y_0\, b\cosh(ky)\ \cos(kx)}{\cosh(ky_0)}. \tag{4.24}$$

The $O(\epsilon^2)$ terms show that $\nabla^2\tau_2 = 0$, $(\tau_{2,y})_{y=0} = 0$ and

$$\begin{aligned}\tau_2[x, y_0] &= \frac{1}{2}b^2\cos^2[kx] - \tau_{2,y}[x, y_0]b\cos(kx) \\ &= \frac{1}{4}b^2\big[1 - 2ky_0\tanh(ky_0)\big][1 + \cos(2x)].\end{aligned}$$

The solution is

$$\tau_2 = \frac{1}{4}b^2\left[1 - 2ky_0\tanh(ky_0)\right]\left(1 + \frac{\cos(2kx)\cosh(2ky)}{\cosh(2ky_0)}\right). \tag{4.25}$$

It follows from (4.19) that the potential energy U is given by

$$U = -2\pi^2 h\rho f^2 \mathcal{N}\sin(4\pi ft)\int_{x=0}^{\ell}\mathrm{d}x\int_{y=0}^{c(x)}\tau\mathrm{d}y.$$

Using results (4.22), (4.24) and (4.25) we find that

$$U' = \frac{1}{3}\pi^2\mathcal{V}'f'^2\mathcal{N}\sin(4\pi ft)\left[y_0'^2 - 3\epsilon^2 b'^2\left(1 - k'y_0'\tanh(k'y_0')\right)\right] \tag{4.26}$$

in non-dimensional variables.

4.2.6 Kinetic energy

The electromagnetic force (4.19) is irrotational and so are all other body forces, so the flow in the pool is irrotational (except for narrow boundary layers adjacent to the upper and lower pool surfaces). Thus the flow can be represented by a velocity potential ϕ.

4.2.6.1 Boundary conditions

The velocity potential ϕ must satisfy:

$$\nabla^2\phi = 0, \qquad \left(\frac{\partial\phi}{\partial z}\right)_{z=h} = \dot{h}, \qquad \left(\frac{\partial\phi}{\partial z}\right)_{z=0} = 0 \tag{4.27}$$

and the condition on the pool edge $y = c(x)$:

$$\left(\frac{\partial\phi}{\partial n}\right)_{y=c(x)} = v_n. \tag{4.28}$$

Here the co-ordinate n is normal to the edge $y = c(x)$, and v_n is the velocity at a point on the edge. For a fluid particle on the edge $c(x)$,

$$f \text{ say } = y - c(x) = 0. \tag{4.29}$$

Since such a particle must remain on the edge,

$$\frac{\mathrm{D}f}{\mathrm{D}t} = 0, \quad \text{or} \quad \frac{\partial f}{\partial t} = -\nabla\phi \cdot \nabla f. \tag{4.30}$$

From which we obtain the boundary condition at $c(x)$

$$\frac{\partial \phi}{\partial y} + \epsilon k b \frac{\partial \phi}{\partial x} \sin(kx) = \epsilon \dot{b} \cos(kx) - \frac{\dot{h} y_0}{h}. \tag{4.31}$$

4.2.6.2 Velocity potential

Expanding the velocity potential in the form,

$$\phi = \phi_0 + \epsilon\phi_1 + \ldots + \epsilon^m \phi_m \ldots,$$

and taking terms of order zero in ϵ in the boundary condition 4.31 we obtain

$$\phi_0 = \frac{\dot{h}}{2h}(z^2 - y^2), \tag{4.32}$$

the velocity potential due to forced simple oscillations of the pool. This is the simplest type of deformation of the pool; the height h oscillates causing the average pool width y_0 to oscillate in order to conserve volume $\mathcal{V}$. This mode of oscillation is observed only in the experiments when the magnetic field frequency is low, i.e where $f \leq 2$Hz.

Similarly the terms of orders ϵ and ϵ^2 are:

$$\phi_1 = C_1 \cos(kx)\cosh(ky), \text{ and } \phi_2 = C_2 \cos(2kx)\cosh(2ky) \tag{4.33}$$

where

$$C_1 = \frac{\dot{b} + \dot{h}bh^{-1}}{k\sinh(ky_0)}, \text{ and } C_2 = -b\left(\dot{b} + \dot{h}bh^{-1}\right)\frac{\coth(ky_0)}{2\sinh(2ky_0)}. \tag{4.34}$$

Plots of the fluid flow resulting from 4.33 are shown in Figure 4.3.

4.2.6.3 Kinetic energy

The kinetic energy of the irrotational flow in the volume $\mathcal{V}$ is given by

$$T = \frac{1}{2}\rho\int_{\mathcal{V}} \nabla\phi\cdot\nabla\phi \mathrm{d}\mathcal{V} = \frac{1}{2}\rho\int_S \phi\nabla\phi\cdot\mathrm{d}\mathbf{S} \tag{4.35}$$

where we have used the divergence theorem to change to an integral over the surface S which bounds the flow region. We now calculate the kinetic energy of a wavelength section $0 \le x \le \ell$. The lower surface $z = 0$ gives no contribution; by periodicity and symmetry, neither do the boundaries between sections. Thus we need consider only the surface integrals on the upper surface $z = h$ (say S_1) and of the edge along $c(x)$ (say S_2).

On S_1 $\nabla\phi\cdot\mathrm{d}\mathbf{S} = \dot{h}\,\mathrm{d}\mathbf{S}$; thus its contribution T_1 to the kinetic energy is given by

$$T_1 = \frac{1}{2}\rho\dot{h}\int_{x=0}^{\ell}\mathrm{d}x\int_{y=0}^{c(x)}\phi\,\mathrm{d}y. \tag{4.36}$$

On the edge S_2 we ignore the meniscus curvature assuming the surface to be plane and vertical, with equation $y = c(x)$. It may be shown that the surface vector is given by

$$\mathrm{d}\mathbf{S} = (-c'\,,\,1\,,\,0)\mathrm{d}x\,\mathrm{d}z. \tag{4.37}$$

From relations (4.29), (4.30) and (4.37) it then follows that

$$\nabla\phi\cdot\mathrm{d}\mathbf{S} = \dot{c}\mathrm{d}x\,\mathrm{d}z,$$

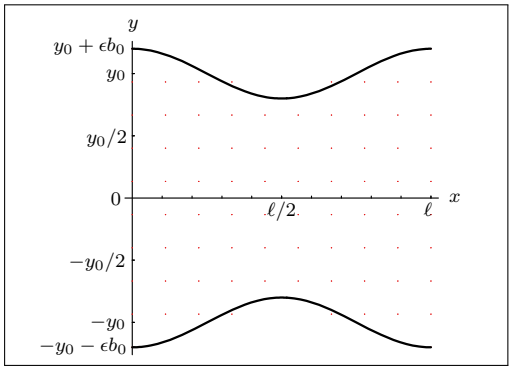

(a) Internal flow at time $t = 0$

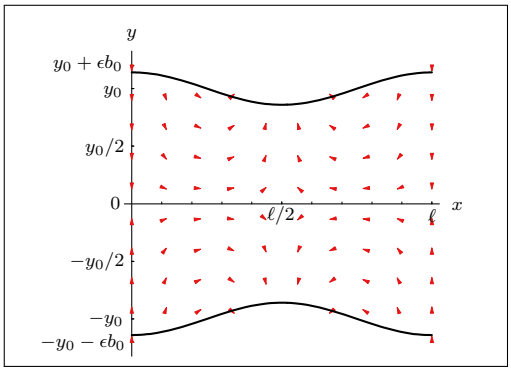

(b) Internal flow at time $t = \frac{T}{4}$

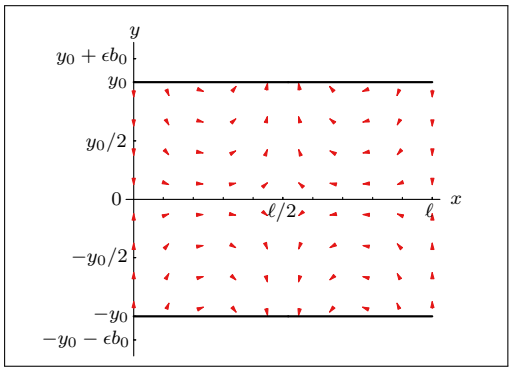

(c) Internal flow at time $t = \frac{T}{2}$

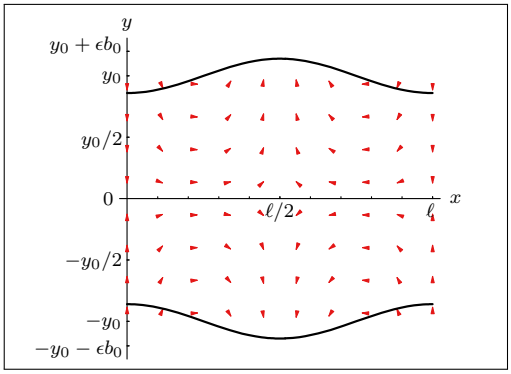

(d) Internal flow at time $t = \frac{3T}{4}$

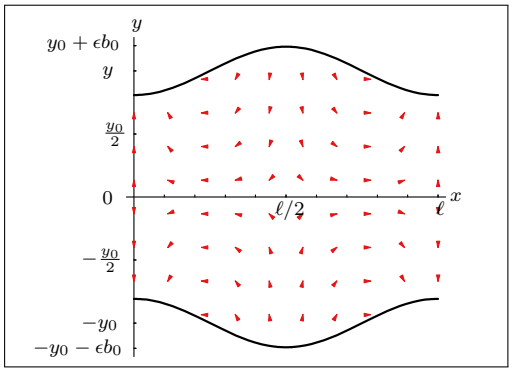

(e) Internal flow at time $t = T$

Figure 4.3: Arrow plots of internal fluid flow caused by a V mode which oscillates with period T say.

so the contribution to the kinetic energy

$$T_2 = \frac{1}{2}\rho \int_0^h \mathrm{d}z \int_0^\ell \phi\big(x, c(x)\big)\dot{c}\,\mathrm{d}x. \tag{4.38}$$

After some algebra and after non-dimensionalising in the same manner as (4.17), we find that we can write the total kinetic energy as a quadratic form in $\dot{h}'$ and $\dot{b}'$,

$$T = Q_0\dot{h}'^2 + \epsilon^2\left(Q_1\dot{h}'^2 + 2R\dot{h}'\dot{b}' + S\dot{b}'^2\right), \tag{4.39}$$

where the non-dimensional coefficients Q_0, Q_1, R and S are:

$$\begin{aligned} Q_0 &= \frac{1}{6}\mathcal{V}'\left[1 + \frac{y_0'^2}{h'^2}\right], & Q_1 &= \frac{\mathcal{V}'b^2}{4h'^2}\left[\frac{\coth(k'y_0')}{k'y_0'} - 1\right] \\ R &= \frac{\mathcal{V}'b'}{4'h'}\left[\frac{\coth(k'y_0')}{k'y_0'} - 1\right], & S &= \frac{\mathcal{V}'}{4k'y_0'}\coth(k'y_0'), \end{aligned} \tag{4.40}$$

where we have non–dimensionalised in the same manner as the energy (4.17) and

$$y_0' = y_0/h_0.$$

4.2.7 Lagrange's equations

Using non–dimensional energies (4.17), (4.39) and (4.26), the Lagrangian 4.8 becomes:

$$L = Q_0\dot{h}'^2 + \epsilon^2(Q_1\dot{h}'^2 + 2R\dot{h}'\dot{b}' + S\dot{b}'^2) - E - U'. \tag{4.41}$$

The resulting Euler-Lagrange equations are:

$$\begin{aligned} \frac{\partial}{\partial t'}\frac{\partial L}{\partial \dot{h}'} - \frac{\partial L}{\partial h'} &= 0, \text{ and} \\ \frac{\partial}{\partial t'}\frac{\partial L}{\partial \dot{b}'} - \frac{\partial L}{\partial b'} &= 0. \end{aligned} \tag{4.42}$$

These yield the following coupled system consisting of two ordinary differential equations:

$$\epsilon^2(2S\ddot{b}' + 2S_h\dot{h}'\dot{b}' + 2R\ddot{h}' + 2R_h\dot{h}'^2 - Q_{1b}\dot{h}'^2) + E_b + U_b = 0, \text{ and} \tag{4.43a}$$

$$\begin{aligned}\epsilon^2(2\ddot{h}'Q_1 + \dot{h}'^2Q_{1h} + 2Q_{1b}\dot{h}'\dot{b}' + 2R\ddot{b}' + 2R_b\dot{b}'^2 - S_h\dot{b}'^2) \\ + 2\ddot{h}'Q_0 + \dot{h}'^2Q_{0h} + E_h + U_h = 0,\end{aligned} \tag{4.43b}$$

where Q_{1h} denotes the partial derivative of Q_1 with respect to h' and so forth, and we have made use of the fact that

$$S_b = \frac{\partial S}{\partial b'} = 0.$$

Equations (4.43) describe the forced symmetric oscillations of $h(t)$ and the asymmetric oscillations of the edge perturbation amplitude $b(t)$. Both equations describe the the effects of surface tension and the magnetic field on a strip of liquid metal.

4.3 S modes

Here we detail the changes required to consider S type modes. The geometry is similar but the displacement is not symmetric in the y direction as the boundary at $y = -y_0$ is now given by

$$y = d(x) = -y_0(t) + \epsilon b(t)\cos(kx). \tag{4.44}$$

This breaks the symmetry across the y direction so we must now consider the volume $2\mathcal{V}$ enclosed each boundary. The geometry is shown in Figure 4.2.

4.3.1 Potential energy

The gravitational and surface tension energies are simply twice as large as those of the V mode model. This is because the surface area is twice as large. Thus the non–dimensional potential energy of the system is simply $2E$ where E is given by equation (4.17).

4.3.2 Electromagnetic potential energy

As before, the electromagnetic body force is given by expression 4.19, but now we have the additional boundary condition on τ:

$$\tau\left[x, d(x)\right] = \text{ constant.} \tag{4.45}$$

Repeating the calculation of τ, we find that τ_0 remains unchanged and the remaining terms are:

$$\tau_1 = \frac{y_0\, b \sinh(ky)\, \cos(kx)}{\sinh(ky_0)}, \text{ and} \tag{4.46}$$

$$\tau_2 = \frac{1}{4}b^2\left[1 - 2ky_0 \coth(ky_0)\right]\left(1 + \frac{\cos(2kx)\cosh(2ky)}{\cosh(2ky_0)}\right). \tag{4.47}$$

Because our geometry is no longer symmetric about the x axis, we must compute the magnetic energy $2U$ over the volume $2V$:

$$U = \frac{1}{3}\pi^2 \mathcal{V}' f'^2 \mathcal{N} \sin(4\pi f t)\left[y_0'^2 - \frac{3}{2}\epsilon^2 b'^2\right]. \tag{4.48}$$

4.3.3 Velocity potential

Changing the pool boundaries changes the velocity potential. In addition to the edge condition 4.28 we have the condition on the edge along $d(x)$:

$$\left(\frac{\partial \phi}{\partial n}\right)_{y=d(x)} = u_n, \tag{4.49}$$

where the co-ordinate n is normal to the edge $y = d(x)$, and the velocity of a point on the edge is u_n. Following a similar derivation as that of the edge along $c(x)$, we obtain the boundary condition at $d(x)$

$$\frac{\partial \phi}{\partial y} + \epsilon k b \frac{\partial \phi}{\partial x} \sin(kx) = \epsilon \dot{b} \cos(kx) + \frac{\dot{h} y_0}{h}. \tag{4.50}$$

This is almost the same as boundary condition 4.31, but the last term has changed sign. The base potential ϕ_0 given by equation (4.32) is unmodified; the others, ϕ_1 and ϕ_2 become

$$\phi_1 = C_1 \cos(kx) \sinh(ky), \text{ and } \phi_2 = C_2 \cos(2kx) \cosh(2ky), \tag{4.51}$$

where

$$C_1 = \frac{\dot{b} + \dot{h} b h^{-1}}{k \cosh(k y_0)}, \text{ and } C_2 = -b \left(\dot{b} + \dot{h} b h^{-1} \right) \frac{\tanh(k y_0)}{2 \sinh(2 k y_0)}. \tag{4.52}$$

Plots of the fluid flow are shown in Figure 4.4.

4.3.4 Kinetic energy

The kinetic energy calculation proceeds as in the V mode case with minor modifications. The volume under consideration is now $2\mathcal{V}$, thus the kinetic energy integral 4.35 becomes

$$2T = \frac{1}{2} \rho \int_S \phi \nabla \phi \cdot \mathrm{d}\mathbf{S}, \tag{4.53}$$

where the surface S is the surface bounding the flow region. As before the lower surface $z = 0$ and the surfaces between sections give no contribution. Again we need to consider the surface integrals on the upper surface S_1 at $z = h$, and the surface S_2 of the edge along $c(x)$, and also the additional contribution from the surface S_3 along the edge $d(x)$. Also S_1 is now bounded by the edges at $y = c(x)$ and $y = d(x)$.

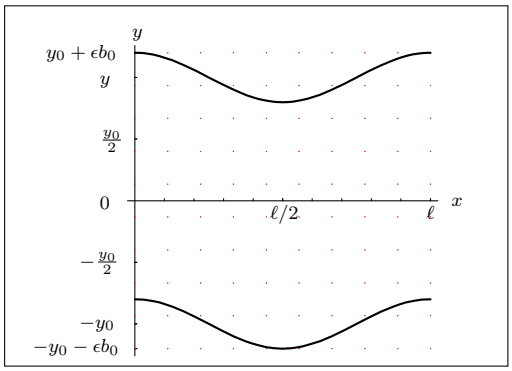

(a) Internal flow at time $t = 0$

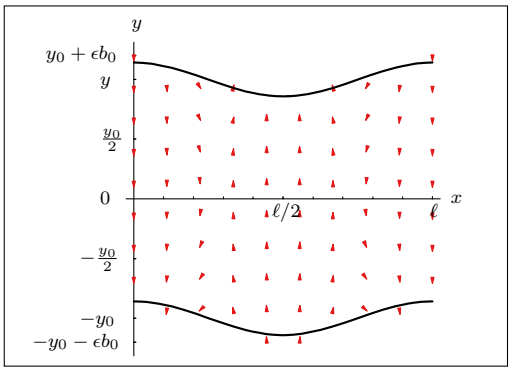

(b) Internal flow at time $t = \frac{T}{4}$

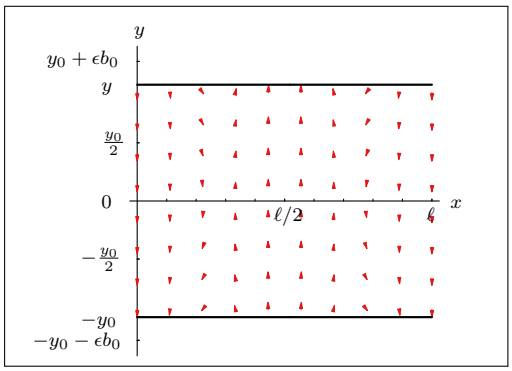

(c) Internal flow at time $t = \frac{T}{2}$

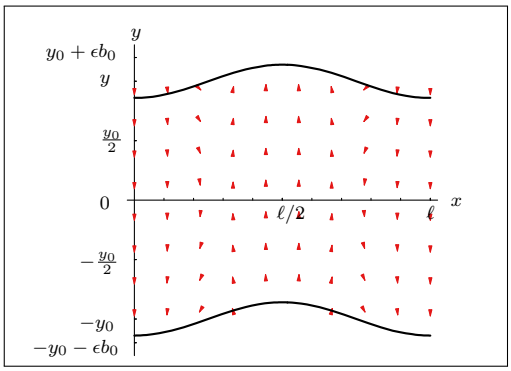

(d) Internal flow at time $t = \frac{3T}{4}$

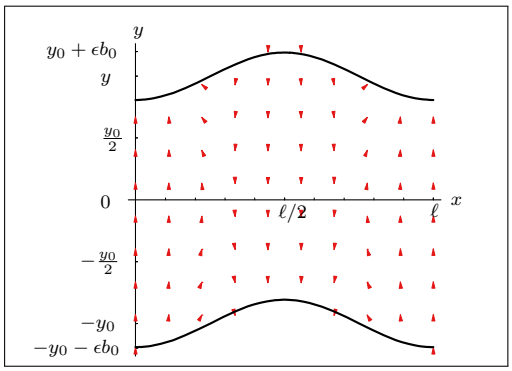

(e) Internal flow at time $t = T$

Figure 4.4: Arrow plots of internal fluid flow caused by a S mode which oscillates with period T say.

We calculate the kinetic energy T as before and the contribution due to S_3 is calculated in a similar fashion to that of S_2 (see equation (4.36)). The resulting kinetic energy is a quadratic form given by 4.39, where the non-dimensional coefficients are

$$Q_0 = \frac{1}{6}\mathcal{V}'\left[1+\frac{y_0'^2}{h'^2}\right], \qquad Q_1 = \frac{\mathcal{V}'b^2}{4h'^2}\left[\frac{\tanh(k'y_0')}{k'y_0'}-1\right],$$
$$R = \frac{\mathcal{V}'b'}{4'h'}\left[\frac{\tanh(k'y_0')}{k'y_0'}-1\right], \qquad S = \frac{\mathcal{V}'}{4k'y_0'}\tanh(k'y_0'). \tag{4.54}$$

On comparison with the coefficients 4.40 of the V-mode model we see the only change is that the $\coth(k'y_0')$ term has been replaced by its reciprocal– $\tanh(k'y_0')$.

4.3.5 Lagrange equations

The Lagrangian function is again given by equation (4.41) where we use the new coefficients given by equation (4.54) and the electromagnetic magnetic potential energy by 4.48. As we have already noted, E is the sum of surface tension and potential energies given by expression 4.17 does not change.

4.3.6 Simple oscillations of pool width w

We now consider the special case where we have no edge perturbation, so $\epsilon = 0$ and the edge of the pool is simply vertical. Obviously this mode is independent of the type of perturbation imposed on the edge, so both models for the V and S modes give the same result. In this case the Lagrangian 4.41 is simply

$$L = Q_0\dot{h}^2 - E - U, \tag{4.55}$$

where the potential energy E and electromagnetic energy U simplify to

$$E' = \frac{1}{2}\mathcal{V}\left(\frac{1}{h'}+h'\right)+\frac{1}{4}\frac{\mathcal{V}'}{h'}, \text{ and } U = \frac{1}{3}\pi^2\mathcal{V}'y_0'^2f'^2\mathcal{N}\sin(4\pi f't').$$

Equations (4.43) reduce to

$$2\ddot{h}Q_0 + \dot{h}^2 Q_{0h} + E_h + U_h = 0, \text{ or}$$

$$\frac{1}{3}\left[1 + \frac{y_0'^2}{h'^2}\right]\ddot{h}' - \frac{1}{3}\frac{y_0'^2}{h'^3}\dot{h}'^2 + \frac{1}{2} - \frac{3}{4h'^2} = \frac{2\pi^2 \mathcal{N} f'^2 y_0'^2}{3h'} \sin(4\pi f' t'). \tag{4.56}$$

This equation governs the electromagnetically forced oscillations of the height h and width y_0 of the Ga-In strip. Equation (4.56) contains an electromagnetic forcing term which oscillates at twice the field frequency.

Small deformations in h.

For a physical interpretation of the symmetric forced oscillations governed by equation (4.56), we consider small-amplitude oscillations and obtain an eigenfrequency for this mode of oscillation. This case corresponds with small values of interaction parameter $\mathcal{N}$. Thus, we consider a small change η in pool height from rest $h = h_0$ or $h' = 1$, i.e

$$h'(t') = 1 + \eta, \tag{4.57}$$

where $\eta = O(\mathcal{N})$, $\mathcal{N}$ being a small parameter.

Introducing expression 4.57 into equation (4.56), linearising and retaining only the terms of $O(\mathcal{N})$ yields the equation governing the strip motion

$$\ddot{\eta} + \Omega'^2 \eta = \frac{2\pi^2 \mathcal{N} f'^2 y_0'^2}{(1 + y_0'^2)} \sin(4\pi f' t'), \tag{4.58}$$

where

$$\Omega'^2 = \frac{1}{1 + y_0'^2}. \tag{4.59}$$

Thus the amplitude η is governed by an electromagnetically-forced simple harmonic oscillator equation. The dimensionless eigenfrequency of the unforced oscillations is $F' = \Omega'/(2\pi)$. Since the electromagnetic forcing has dimension-

less frequency $2f'$, resonance occurs at frequency

$$f'_{simp} = \frac{1}{2}F' = \frac{\Omega'}{4\pi}, \tag{4.60}$$

or in terms of dimensional parameters

$$f_{simp} = \frac{12\gamma}{\rho\left(h_0 y_0^2 + h_0^3\right)}. \tag{4.61}$$

4.3.7 Azimuthal "varicose" and "sinuous" modes

We now consider the special case where the pool height h is held constant at the height $h = h_0$, allowing only the edge perturbation amplitude b to oscillate under the effects of electromagnetic forcing. In this case the Lagrangian 4.41 is simply

$$L = \epsilon^2 \dot{b}^2 S - E - U', \tag{4.62}$$

which reduces the system of ODEs 4.43 to

$$2\epsilon^2 \ddot{b}' S + E_b + U_b = 0, \text{ or} \tag{4.63}$$

$$\ddot{b}' + b'\Omega'^2[1 - C\sin\left(4\pi f' t'\right)] = 0. \tag{4.64}$$

This is a Mathieu equation with dimensionless eigenfrequency

$$\Omega'^2 = \Omega_V'^2 = \frac{\pi}{2\mathcal{V}'} k' y_0' \tanh(k' y_0'), \tag{4.65}$$

and

$$C = C_V = \frac{8\pi \mathcal{N} \mathcal{V}' f'^2}{k'} (1 - k' y_0' \tanh(k' y_0')). \tag{4.66}$$

in the V-mode case. In the S-mode case

$$\Omega'^2 = \Omega_S'^2 = \frac{\pi}{2\mathcal{V}'} k'^2 y_0' \coth(k' y_0') \tag{4.67}$$

and

$$C = C_S = \frac{4\pi\mathcal{N}\mathcal{V}' f'^2}{k'}. \tag{4.68}$$

The solutions of the Mathieu equation (4.64) will grow in time when $\mathcal{N}$ exceeds a certain critical value $\mathcal{N}_{crit}$. It is a well known result that the solutions are least stable near the system's eigen frequency

$$f_m = \frac{\Omega}{2\pi}. \tag{4.69}$$

In terms of dimensional parameters f_m is

$$f_m = f_V = \frac{\sqrt{\gamma \tanh(ky_0)}}{\ell^{3/2}\sqrt{\rho}} \tag{4.70}$$

for V-modes, and

$$f_m = f_S = \frac{\sqrt{\gamma \coth(ky_0)}}{\ell^{3/2}\sqrt{\rho}} \tag{4.71}$$

in the S-mode case.

We anticipate the motion to be a combination of vertical pool oscillations of frequency $2f$ governed by equation (4.58) and transverse modes whose amplitude oscillates at f and whose stability is governed by the Mathieu equation (4.64).

4.4 Results and comparison with experimental data

For small $\mathcal{N}$ the transverse modes are not excited and the pool motion is simple, the upper surface at $z = h$ oscillating vertically with frequency $2f$, while the pool edges move in and out to conserve pool volume $\mathcal{V}$. This motion is governed by (4.58), a simple oscillator forced directly by the Lorenz force at $2f$. We have also derived the resonance frequency f_{simp} (see (4.61)) at which these oscillations are most easily excited.

For larger values of $\mathcal{N}$, when a certain critical value $\mathcal{N}_{crit}$ is exceeded, the azimuthal modes are excited. Our Mathieu approximation (equation (4.64)) predicts that the strongest instability is subharmonic. For a given mode, the Mathieu approximation also predicts that a graph of critical values $\mathcal{N}_{crit}$ versus magnetic field frequency f will have a "v" shape, centred around a minimum at the eigenfrequency f_m (equation (4.69)). A table of theoretical and experimentally determined values of f_m is given in Table 4.1. The stability diagrams predicted by the Mathieu approximation for various modes are shown in Figures 4.5(b), 4.6(b), 4.7(b), 4.8(b), 4.9(b) and 4.10(b). Concerning the transition between the axisymmetric and azimuthal modes, we obtain predictions of the critical value $\mathcal{N}_{crit}$ from our full model (equations (4.43a) and (4.43b)) for various modes at various frequencies. These results are graphed as lines in Figures 4.5(a), 4.6(a), 4.7(a), 4.8(a), 4.9(a) and 4.10(a). These critical values are calculated to an absolute error of 1×10^{-3} using a bisection method. To determine if a value of $\mathcal{N}$ is unstable the ordinary differential equations (4.43a) and (4.43b) were solved using the Runge Kutta 4 method with automatic time step control (Press et al. [1992]) with a relative error per step of 10^{-5}, where the run was limited to 1000 periods of the magnetic field. If during a run the absolute value of the azimuthal wave amplitude b grows 3 orders of magnitude larger than its initial value of 10^{-4} the solution is considered unstable. To

	Mathieu f_m (Hz)		Experimental f_m (Hz)	
Mode	V mode	S mode	V mode	S mode
4.4	1.695	1.812		2.05
5.1	2.144	2.229	2.20	
6.2	2.906	2.955	2.70	
7.1	3.577	3.606	3.25	
8.0	4.287	4.304	3.85	3.95
8.9	5.035	5.046	4.55	4.55
10.8	6.736	6.739		5.30
11.3	7.210	7.212	5.90	5.90
11.9	7.792	7.794	6.60	6.60
12.5	8.389	8.390	7.40	

Table 4.1: Resonance frequencies f_m for various transverse modes determined experimentally and using the Mathieu approximation.

ensure that the values of $\mathcal{N}_{crit}$ obtained using this method were not influenced by the parameters chosen, all of the parameters mentioned above were varied by at least one order of magnitude and results were not significantly changed.

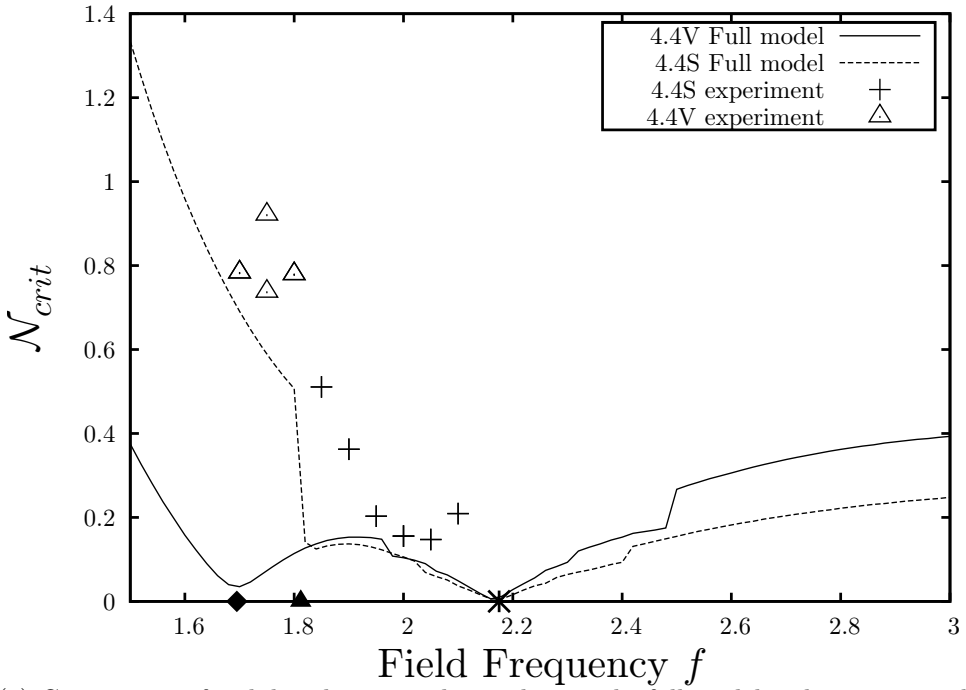

(a) Comparison of stability diagrams obtained using the full model and experimental results.

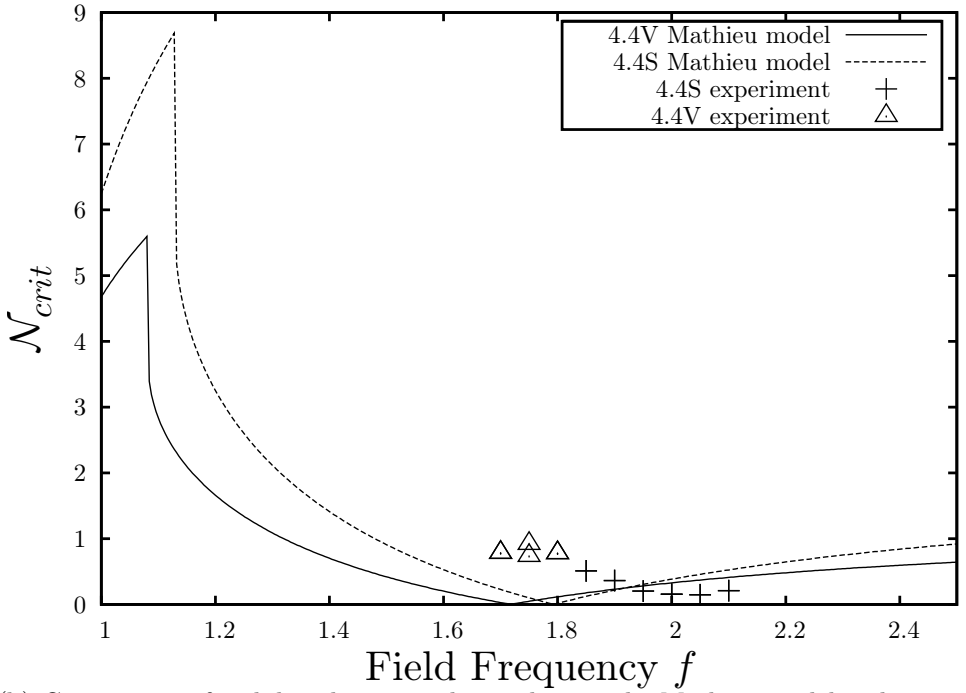

(b) Comparison of stability diagrams obtained using the Mathieu model and experimental results.

Figure 4.5: Comparison between theory and experimental results for transverse modes 4.4V and 4.4S. The predicted $\mathcal{N}_{crit}$ are plotted alongside the experimental results. A key for each graph is shown in the top right corner. The star marks the position of the resonance frequency f_{simp} of the simple modes. The positions of the resonance frequencies of the V and S modes are marked with a solid diamond and triangle respectively.

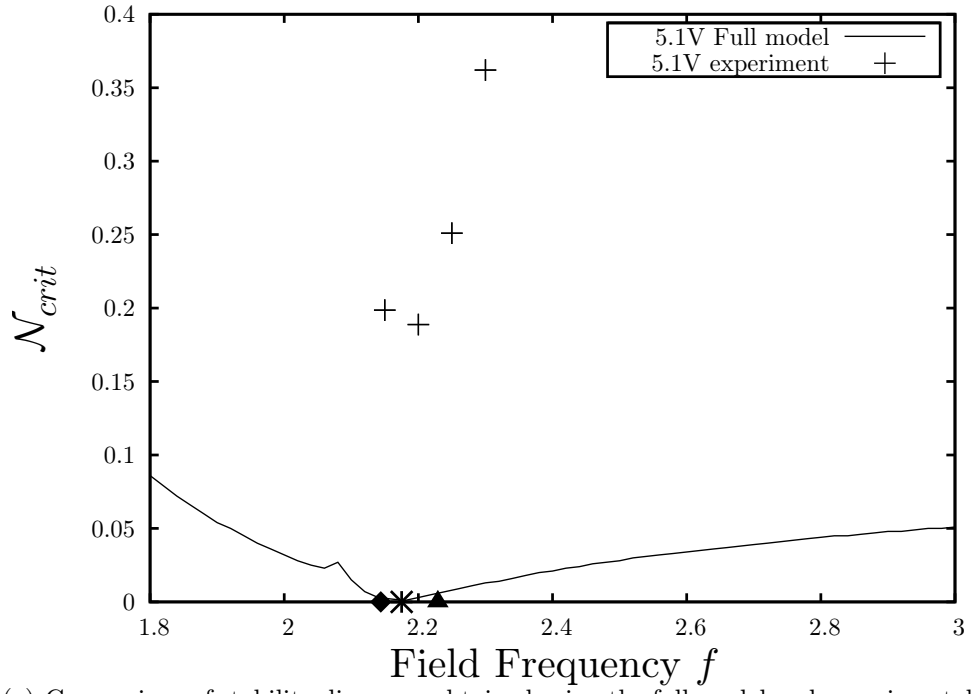

(a) Comparison of stability diagrams obtained using the full model and experimental results.

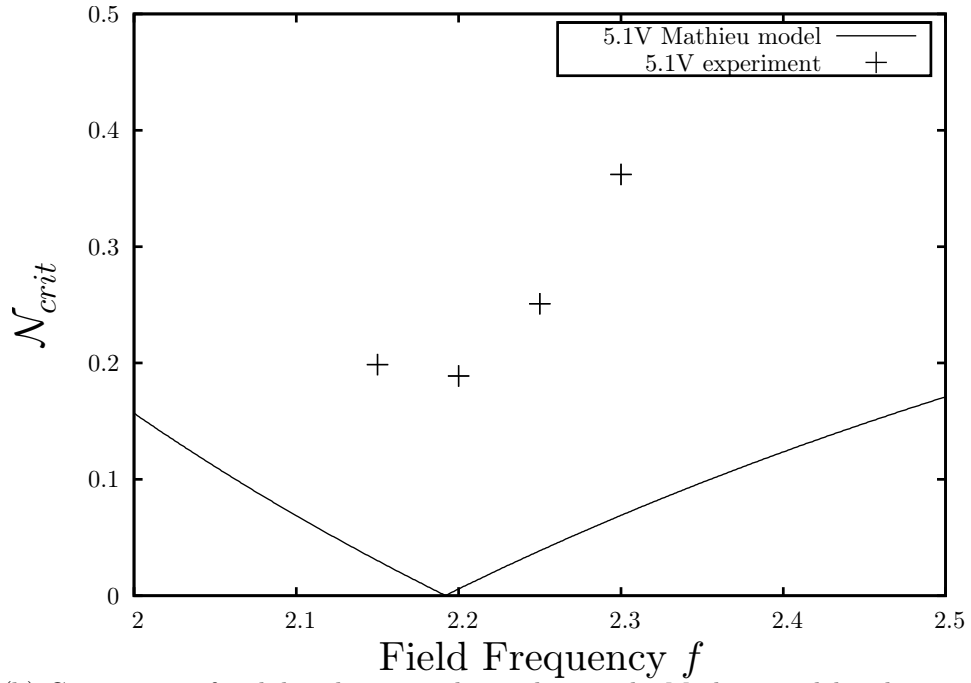

(b) Comparison of stability diagrams obtained using the Mathieu model and experimental results.

Figure 4.6: Comparison between theory and experimental results for transverse modes 5.1V. The predicted $\mathcal{N}_{crit}$ are plotted alongside the experimental results. A key for each graph is shown in the top right corner.

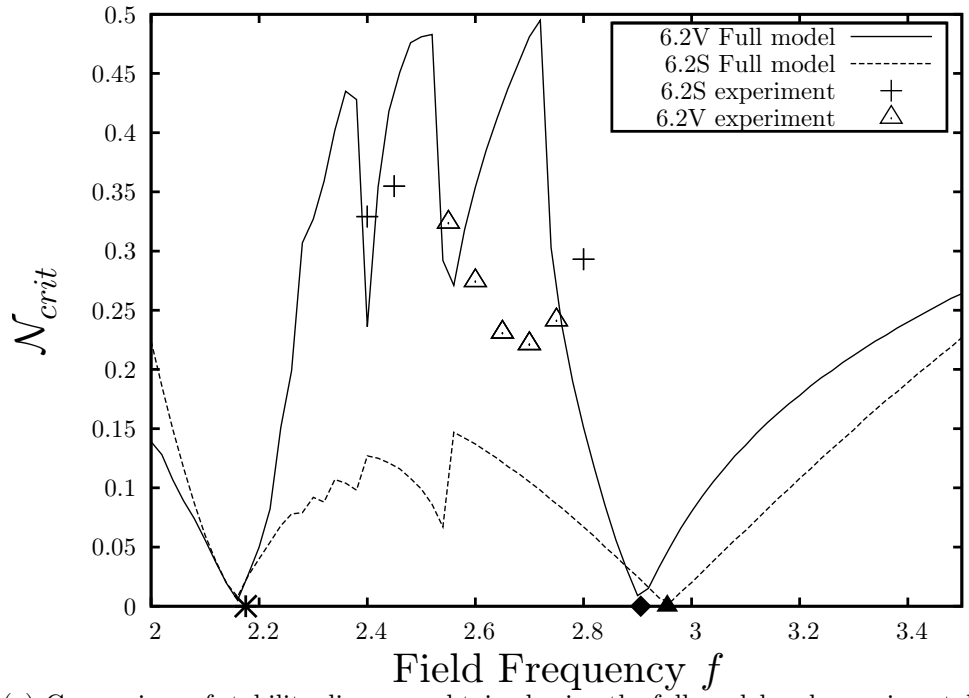

(a) Comparison of stability diagrams obtained using the full model and experimental results.

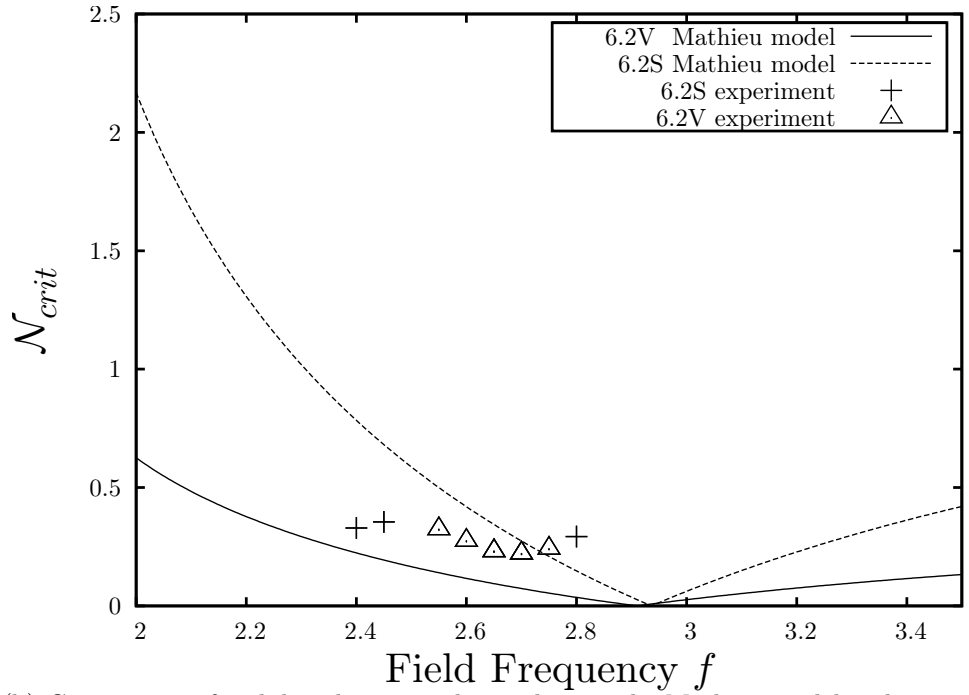

(b) Comparison of stability diagrams obtained using the Mathieu model and experimental results.

Figure 4.7: Comparison between theory and experimental results for transverse modes 6.2V and 6.2S. The predicted $\mathcal{N}_{crit}$ are plotted alongside the experimental results. A key for each graph is shown in the top right corner.

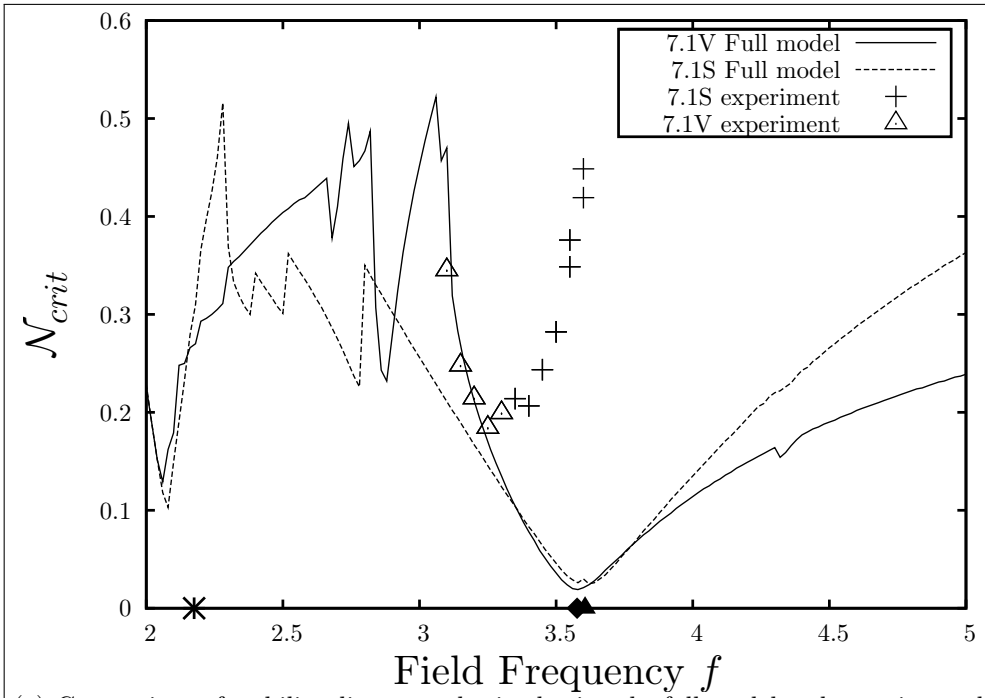

(a) Comparison of stability diagrams obtained using the full model and experimental results.

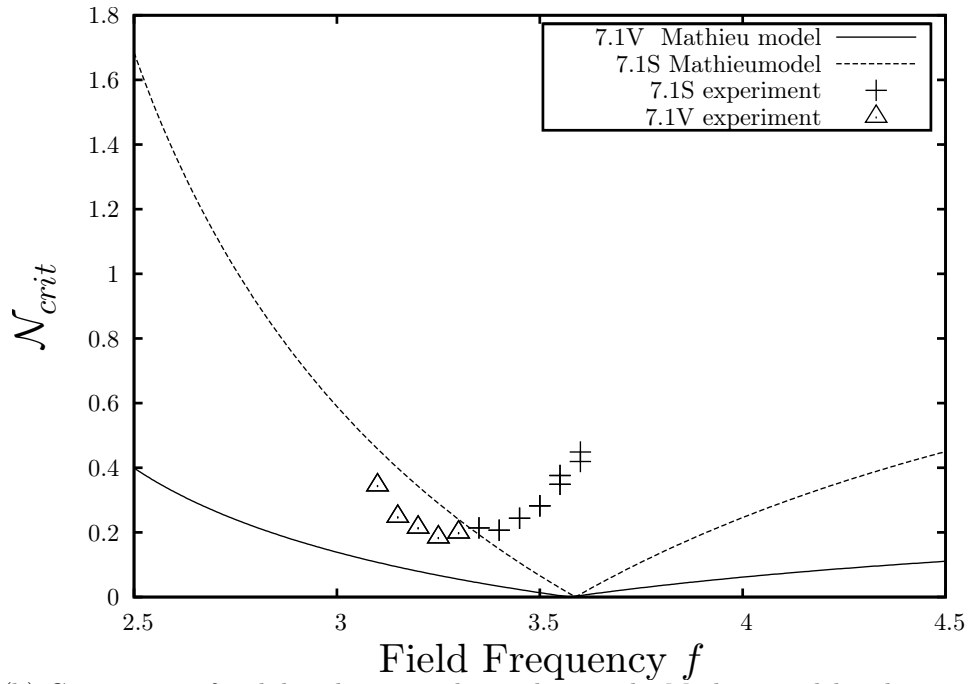

(b) Comparison of stability diagrams obtained using the Mathieu model and experimental results.

Figure 4.8: Comparison between theory and experimental results for transverse modes 7.1V and 7.1S. The predicted $\mathcal{N}_{crit}$ are plotted alongside the experimental results. A key for each graph is shown in the top right corner.

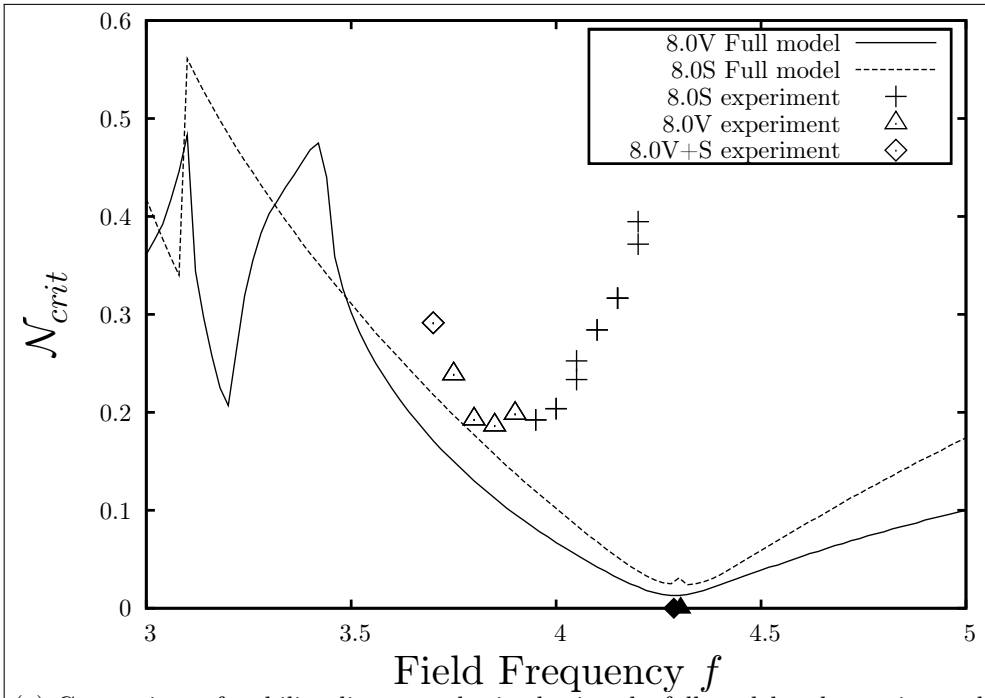

(a) Comparison of stability diagrams obtained using the full model and experimental results.

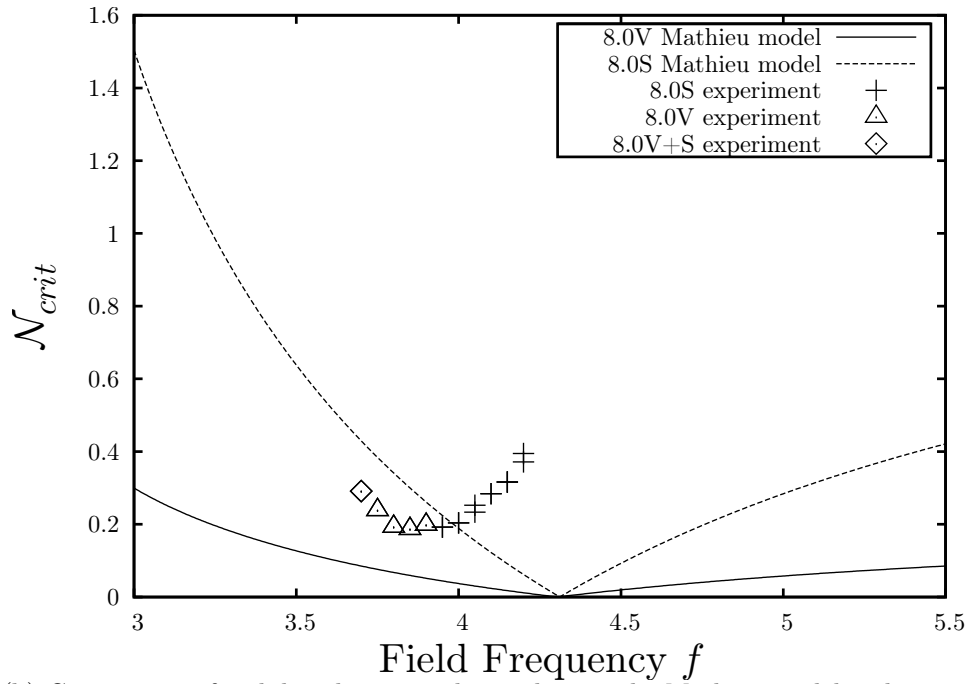

(b) Comparison of stability diagrams obtained using the Mathieu model and experimental results.

Figure 4.9: Comparison between theory and experimental results for transverse modes 8.0V and 8.0S. The predicted $\mathcal{N}_{crit}$ are plotted alongside the experimental results. A key for each graph is shown in the top right corner.

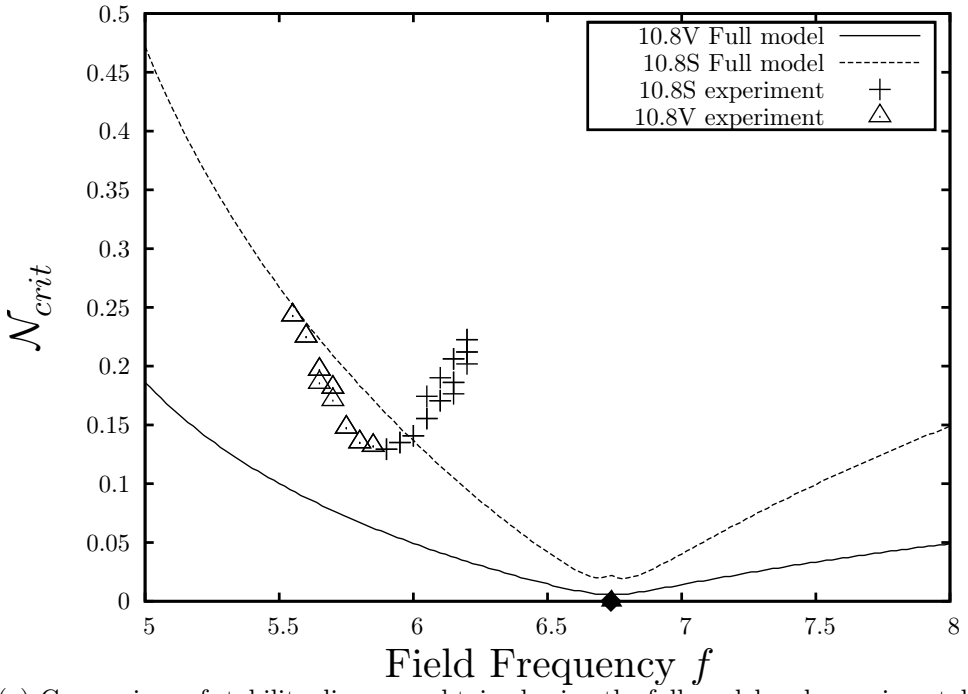

(a) Comparison of stability diagrams obtained using the full model and experimental results.

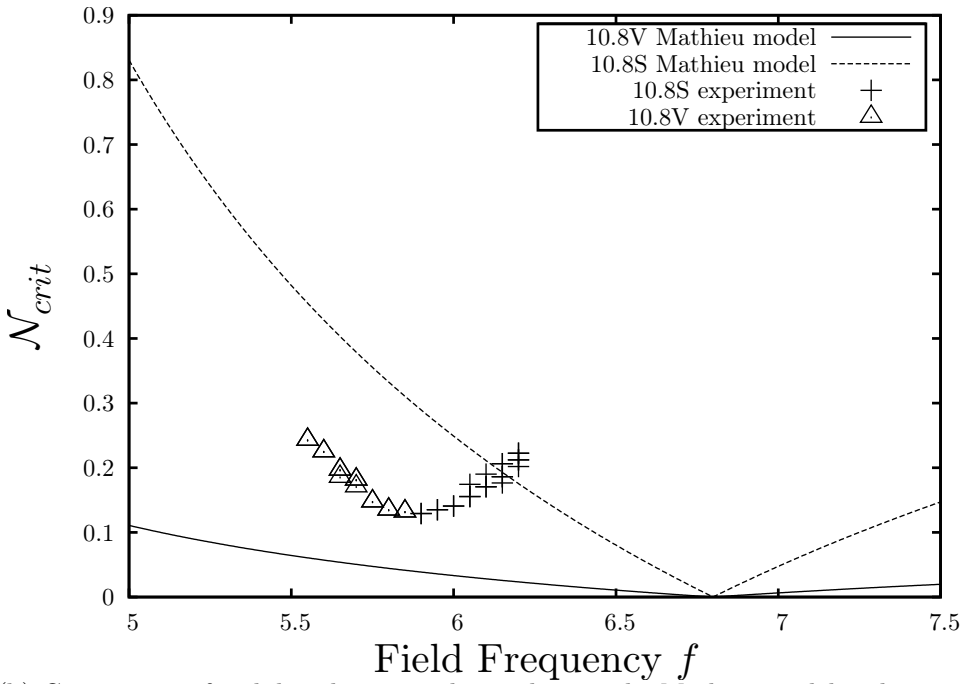

(b) Comparison of stability diagrams obtained using the Mathieu model and experimental results.

Figure 4.10: Comparison between theory and experimental results for transverse modes 10.8V and 10.8S. The predicted $\mathcal{N}_{crit}$ are plotted alongside the experimental results. A key for each graph is shown in the top right corner.

4.5 Discussion

We compared our theory with the experimental results in Chapter 3 bearing in mind we make the following assumptions in our the analysis:

- treatment of the fluid flow is simplified, we assume it is potential,
- we assume a uniform applied magnetic field,
- we assume the shield parameter (R_f) is small,
- we assume that the amplitude of an azimuthal mode is small compared to h,
- we do not consider coupling between azimuthal modes.

The last assumption is almost certainly the most important source of discrepancy between the experimental and theoretically calculated stability diagrams.

Despite the simplified geometry used, we feel that the resonance frequencies f_m (equation (4.69)) predicted by Mathieu approximation (4.64) compare well with the experimentally determined f_m. The resonance f_m may be estimated from the experimentally determined stability diagrams from the frequency f at which a given mode is most easily excited, i.e the minimum $\mathcal{N}_{crit}$. These are compared with the f_m predicted by (4.69) in Table 4.1. The f_m predicted by (4.69) differ from the experimentally determined values by at most 20% but for a number of modes, they are within 10%.

When a varicose and sinuous mode which have the same wavelength ℓ are observed in the experiments, the varicose mode is excited at lower frequencies than the sinuous mode. The Mathieu approximation predicts that for two modes which have the same ℓ, f_m will be smaller for the varicose mode than for the sinuous mode. Indeed the stability diagrams predicted by the Mathieu equation predict that mode 4.4V will be excited at lower f than 4.4S. Unfortunately this is not true of other modes, the Mathieu approximation predicting

that the V mode will always be more easily excited. This is probably due to the fact that in our derivation varicose and sinuous modes are considered in isolation and therefore coupling between them is not considered.

Nonetheless we observe that the stability diagrams (see Figures 4.5 to 4.10) obtained from the full model and the Mathieu approximation have the same basic structure as the experimental results. That is to say that the experimentally obtained values of $\mathcal{N}_{crit}$ have the same vee shape as the theoretically determined values, with a minimum centred on the eigenfrequency f_m of the mode under consideration. In general the stability diagram predicted by full model compares better with the experimental stability diagram than the Mathieu diagram, indicating that coupling between the simple oscillations is an important effect. We conclude that although our theory does not explain all of the structure present in the experimental stability diagram, it does explain the basic vee shape structure. Our theory shows that this structure is due to a Mathieu-type subharmonic instability which is the basic mechanism for the transverse modes.

Chapter 5

Experimeintal investigation of the effects of a medium frequency magnetic field on a pool of liquid metal

5.1 Introduction

In Chapters 2 and 3 we examined the effect of a low-frequency magnetic field on a pool of liquid metal. In the low-frequency limit, the pool's effect on the magnetic field may be neglected which simplified our analysis of the parametric free surface instabilities observed.

In industrial processes, more often higher frequency fields are used in processes such as levitation (Muck [1923], Okress et al. [1952]) and cold crucible metallurgy. The physics of these processes is more complicated as at larger magnetic field frequencies f, the currents induced in the liquid metal by the external field partially expel the field from the fluid interior. This complicates the electromagnetic calculation significantly. As the shape of the liquid changes, so does the configuration of the induced currents. This in turn affects the external magnetic field.

The objective of this chapter is to describe the results of experiments which investigate the various instabilities encountered in levitation and quasi-levitation processes. We continue the work of Perrier [2002]; however a special device has been designed to control the temperature variation and to minimise surface oxidation of the pool. Both phenomena were prevalent in his preliminary investigation.

We consider the effects of a medium-frequency magnetic field on a pool of Ga-In-Sn. The pool geometry is similar to that of the "starfish" experiment we analysed in Chapter 2. We examine the effect of a 7.8kHz magnetic field on pools of liquid metal (Ga-In-Sn). Three different pool volumes are used, 5ml, 7ml and 10ml. The equipment used did not allow the field frequency to be varied. Thus we vary field strength B_0 instead and we observe increasingly complicated phenomena with increasing B_0. Two types of phenomena were observed: slow symmetric oscillation of the pool perimeter and pool rotation. Diagrams of the pool and experimental apparatus are given in Figures 5.1, 5.2 and 5.3.

In the first instance the pool perimeter is deformed in a regular pattern either elliptic, triangular or square. The extrema of the pool perimeter oscillate radially, typically with a frequency f_{osc} say of a couple of hertz. At certain field strengths we observed that the pool perimeter would cease oscillating radially and the pool would briefly rotate with angular velocity ω_{rot} say about its centre in either direction. Pool rotation was generally brief, only a few seconds, before the pool rotation stopped and reversed sense or resumed oscillating radially. Examples of these types behaviour are given in Figures 5.5 to 5.15.

There have been many investigations of the effects of medium or high frequency magnetic fields on a free surface. Complete levitation or quasi-levitation in cold crucible processing has been studied experimentally. Various types of free surface instability have been observed or predicted theoretically (Priede and Gerbeth [2000a], Priede and Gerbeth [2000b], Priede and Gerbeth [2005], Priede and Gerbeth [2006]). A key difficulty with levitation is maintaining the stability of large drops of heavy metal when they are levitated by strong magnetic fields.

Vinsard et al perfomed interesting experimental and theoretic investigations of the effect of a medium frequency field on a flat pool in a cylindrical container (Hinaje et al. [2006b], Dufour and Vinsard [2007], Hinaje et al. [2006a],Hinaje et al. [2006c]). They shows that the surface deforms itself into the form of a "key hole" or hammer like shape. Experimental investigations of a pool resting on a substrate were also carried by Conrath and Karcher [2005]. They show for moderate magnetic field strength that an azimuthal instability leads to the formation of a triangle shaped mode 3 or sometimes a square shaped mode 4. They determine the stability threshold, which depends on the magnetic field frequency. We observe the same modes in our experiment and call them triangle and square modes, examples of which are given in Figures 5.6 to 5.14. Perrier [2002] present the results of similar experiments with a larger drop and with higher magnetic field strengths. Complex morphologies were observed, but due to the high temperatures of the drop caused by the significant Joule

heating, the influence of oxidation on the surface tension was significant.

5.2 Experimental apparatus

Due to the higher magnetic field frequency used than in starfish and strip experiments, the pool is strongly heated by the external magnetic field. Thus special care is taken to remove heat from the pool to maintain approximately isothermic conditions. As in the "starfish experiment" analysed in Chapter 2, the pool rests on a slightly concave substrate. This substrate is the base of a boronitrate crucible whose dimensions are given in Figure 5.1. For more detailed dimensions of the concave base see Figure 5.2. Boronitrate is used due to its weak electrical conductivity and high thermal conductivity. These properties allow heat to be effectively removed from the pool while ensuring that the crucible does not influence the external magnetic field. The boronitrate crucible is mounted in a second PVC crucible and is cooled by water as indicated with blue arrows in Figure 5.1. Oxidation of the pool surface is avoided by a covering layer of water-HCl solution.

The pool is subject to a medium frequency magnetic field of 7.8KHz. This field is produced by alternating current flowing in a coil of copper pipe. The coil is constructed from 6 turns of 10mm diameter copper pipe, each turn is separated by a 2mm gap. The inner coil diameter is equal to the outer diameter of the crucible assembly. The crucible assembly is mounted inside the coil as shown in Figure 5.3.

5.2.1 Dimensionless parameters

The screen parameter

$$R_f = 2\pi f \sigma \mu_0 a^2 \tag{5.1}$$

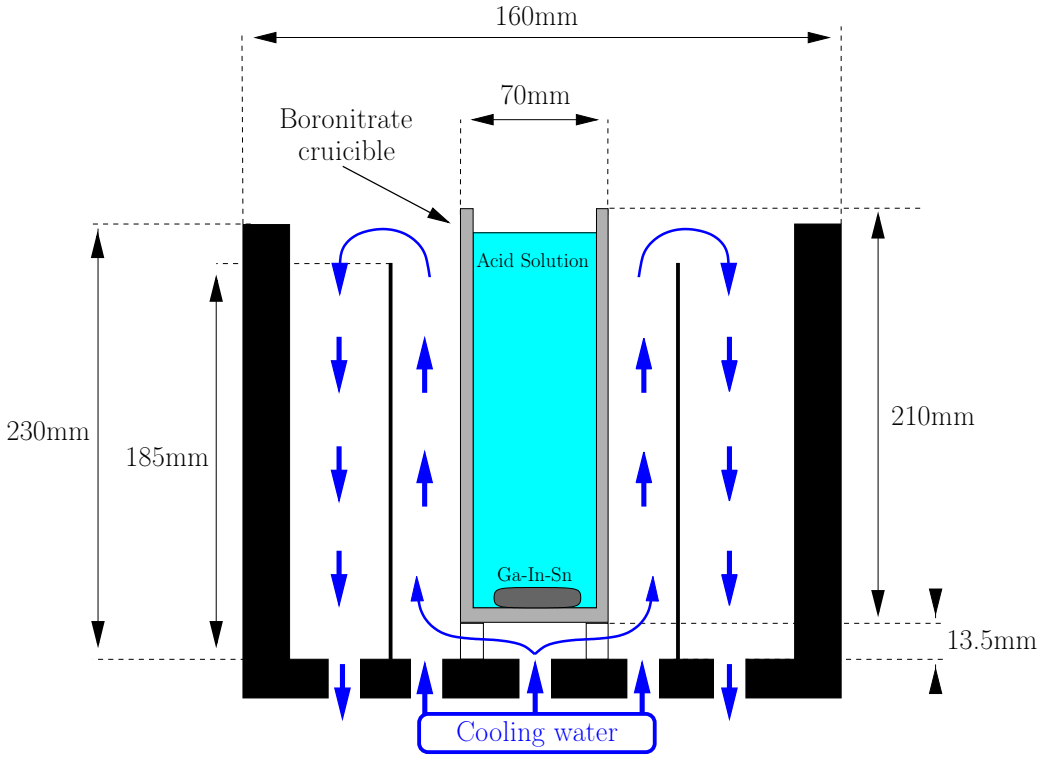

Figure 5.1: Sketch of the crucible assembly. The Ga-In-Sn rests at the base of a boronitrate crucible as depicted above. To slow oxidation of the Ga-In-Sn, it is immersed in a water-HCl solution. The Ga-In-Sn is heated by the imposed magnetic field and is cooled with water as shown.

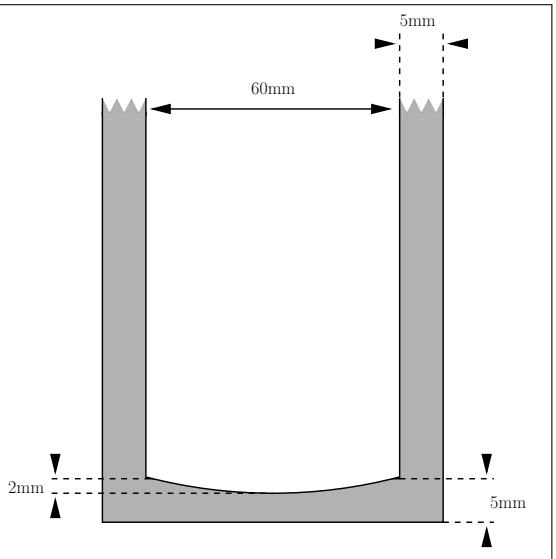

Figure 5.2: Sketch of the bottom of the boronitrate crucible detailing the material thickness used as well as the depth of the concave base.

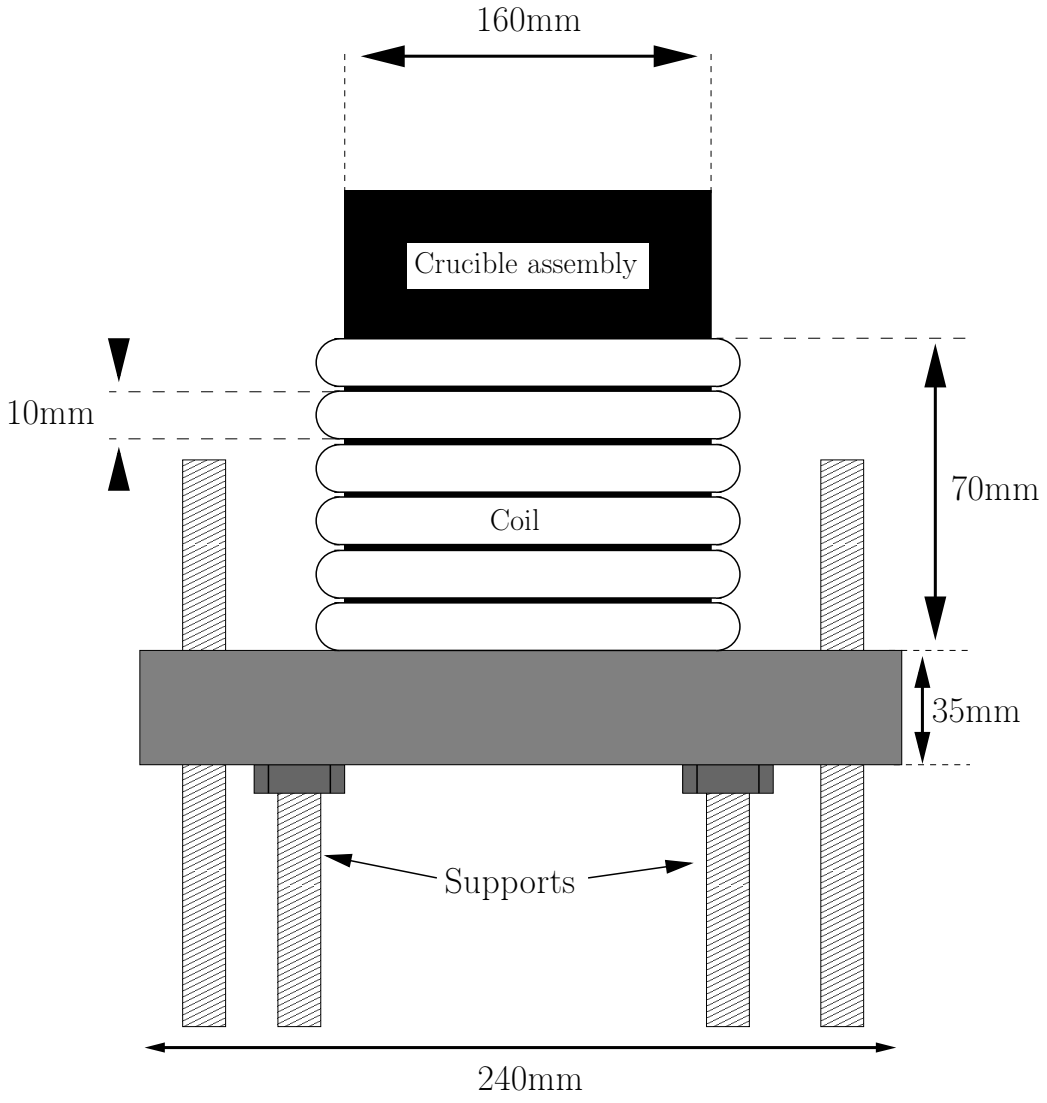

Figure 5.3: Diagram showing the placement of the crucible assembly in the coil. The coil consists of 6 turns of hollow copper pipe. The pipe had a diameter of 10mm and the turns were separated by 2mm. Water flowing through the hollow pipe cools the coil.

is typically of the order 50 in the present experiments; thus the magnetic field is only partially expelled from the pool as the skin depth is given by:

$$\delta_{mag} = \sqrt{\frac{1}{\mu_0 \sigma \pi f}}. \tag{5.2}$$

Skin depth $\delta_{mag} = 3\text{mm}$, which is approximately half the pool depth. Experimentally we have measured the average pool depth h at various field strengths and typically $5\text{mm} < h < 7\text{mm}$.

The magnetic interaction parameter

$$\mathcal{N} = \frac{\sigma B_0^2 a}{\rho U_a}. \tag{5.3}$$

$\mathcal{N}$ is a measure of the ratio of electromagnetic forces to fluid inertia. Here a is the pool radius, and

$$U_a = \frac{B_0}{\sqrt{\mu_0 \rho}} \approx 0.1 \text{ m s}^{-1} \tag{5.4}$$

is a typical velocity of the fluid flow, in this case the Alfvén velocity. In these experiments $\mathcal{N}$ is of order 10^{-3}. Thus the alternating part of the electromagnetic forces is unlikely to drive any significant fluid motion.

The effects of the imposed magnetic field are then better described by the electromagnetic Bond number

$$Bm = f_L / f_\gamma \tag{5.5}$$

defined as the ratio of the Lorentz force f_L to surface tension f_γ. An order of magnitude estimation of f_γ gives

$$f_\gamma = \gamma V^{1/3}. \tag{5.6}$$

Likewise the induced current density is given by

$$j = \frac{B_0}{\mu_0 V^{1/3}}, \tag{5.7}$$

and we estimate the magnetic field strength:

$$B_0 = \mu_0 n I \tag{5.8}$$

were $n = 85.7$ is the number of turns per unit length of our coil and I is RMS value in Amps of the current in the coil. Using equaitions (5.7) and (5.8) we obtain the following estimate of the Lorentz force:

$$f_L = V^{2/3} \mu_0 \left(nI\right)^2 . \tag{5.9}$$

Thus the magnetic Bond number is

$$Bm = \frac{V^{1/3} \mu_0 \left(nI\right)^2}{\gamma}. \tag{5.10}$$

In our experiments $10 < Bm < 200$. We observe the onset of radial pool oscillation and rotation when $Bm > 30$. Thus we speculate that this behaviour is due to an instability which develops between the surface tension and mean part of the electromagnetic force.

The Reynolds number

$$Re = \frac{U_a h}{\nu} \tag{5.11}$$

is of the order 10^3; thus we expect non laminar internal flow.

5.3 Results

We observed complicated behaviour in the course of our experiments. Starting at rest we increase the coil current gradually recording the critical value of Bm_{crit0} at which the pool's behaviour changes. We use 3 different volumes of

Mode	Bm_{crit}	f_{osc} (Hz)	ω_{rot} (rad/s)
5ml drop			
Ellipse	37.6	1.8	-
Ellipse/Triangle transition	50.5 to 58.8	-	-
Triangle	58.8	2.8	-
Rotating triangle	71.2	-	7 to 9
7ml drop			
Triangle	42.5	2.5	-
Rotating Triangle	57.5	-	6 to 10
10ml drop			
Triangle	43.1	2	-
Rotating triangle	54.7	-	7 to 11
Triangle/ Square transition	61.0 to 83.3	-	-
Oscillating Rotating Square	83.3	-	-

Table 5.1: Summary of values of Bm_{crit} at which different modes were observed during the experiment. Values of f_{osc} and ω_{rot} are given where it was possible to measure them.

Ga-In-Sn in the first experiment, 5ml, 7ml and 10ml. These volumes where choosen as the resulting pool does not touch the sides of the crucible during the experiments, so is somewhat similar to the "starfish" experiment we studied earlier. Photos of the pool at rest are given in Figure 5.16. In the second experiment we use a volume of Ga-In-Sn which touches the walls of the crucible and observe different behaviour.

5.3.1 "Starfish" like pool

For magnetic Bond number Bm below some critical value Bm_{crit0} say, we observe only small irregular deformations of the circular pool perimeter. These deformations were too small to be recorded satisfactorily on video. At Bm_{crit0}, we observe that the initially circular pool perimeter is deformed into an elliptic or triangular shape whose extrema oscillate radially as shown in Figures 5.5, 5.9 and 5.11.

As we continue to increase Bm, pool behaviour becomes more irregular. When certain critical values of Bm are reached, which we denote Bm_{crit1}, Bm_{crit2} etc, we observe that the pool perimeter changes its shape to more complicated shapes. The initially elliptic pool perimeter becomes triangular, or the triangular pool becomes square. As with the first mode observed these higher modes oscillate radially with frequency f_{osc} say as shown in Figures 5.7 and 5.14.

In addition to these radially oscillating modes, we observe pool rotation. A pool which is oscillating radially may suddenly stop oscillating and the square or triangular pool will rotate in either a clockwise or anticlockwise direction for a short period (typically 2-3 seconds) with an angular velocity of ω_{rot} say. The pool will then stop rotating and will either resume oscillating radially or will rotate in the opposite direction. Examples of pool rotation are given in Figures 5.8, 5.10, 5.12 and 5.15. Combination of various modes was also observed, and examples of these are given in Figures 5.6 and 5.13.

In the case of a 5ml pool as we increase Bm from zero we observe elliptic radial oscillation when Bm exceeds $Bm_{crit0} = 37.7$. The pool perimeter is deformed into an ellipse like shape which oscillates radially with $f_{osc} = 1.8$Hz. As we increase Bm, the perimeter becomes triangular and for $50.5 < Bm < 58.7$ the oscillating pool perimeter takes on both elliptic and triangular shapes. When we increase Bm to $Bm_{crit1} = 58.8$ we observe only a triangular radial oscillation of the pool perimeter with $f_{osc} = 2.8$Hz. Continuing to increase Bm we observe the onset of rotation at $Bm_{crit2} = 71.2$. The pool maintains a triangular shape while it rotates both clockwise and anticlockwise. We have measured the rotational speed ω_{rot} photographically and ω_{rot} varies between 7 and 9 rad/s.

The behaviour of the 7ml pool is much simpler. Increasing Bm from zero, we observe triangular radial oscillation with $f_{osc} = 2.5$Hz when Bm exceeds $Bm_{crit0} = 42.5$ and we observe the onset of rotation at $Bm_{crit1} = 57.4$. The rotational speed ω_{rot} varies between 6 and 10 rad/s.

The behaviour of the 10ml pool is more complicated. Triangular radial oscillation with $f_{osc} = 2$Hz is observed when Bm exceeds $Bm_{crit0} = 43.1$. Rotation of the triangle shaped pool is observed when Bm exceeds $Bm_{crit1} = 54.7$. The rotation speed ω_{rot} varies between 7 and 11 rad/s. Increasing Bm, we observe that when Bm is larger than $Bm_{crit1} = 61.0$, the pool perimeter takes on a combination of triangle and square shape and the pool continues to rotate. When Bm exceeds 83.3, the pool perimeter is deformed into a square which alternately rotates about its center and osciallates radially. These results are summarised in Table 5.1.

5.3.2 Comparison with J. Priede's model

Priede et al. [2006] study the stability of a perfectly conducting thin liquid disk submitted to a uniform alternating magnetic field. Although the physics of our experiment is somewhat more complicated than that taken into account by their model, we might expect some qualitative agreement between our observations and theirs.

They consider the growth of a small Fourier mode of wave number m, and derive an expression for the critical value Bm_{crit}:

$$Bm_{crit} = (m+1)\pi,\ m = 2, 3, \ldots, \tag{5.12}$$

which indicates that the first unstable mode is $m = 2$. This corresponds to the elliptic radial oscillations we observe. Although this mode is the first mode excited in a 5ml pool, we do not observe it in the larger pools.

They also derive an expression for the mode which will have the greatest growth rate m_{max} when $Bm > Bm_{crit}$:

$$m_{max} = \left[\frac{2Bm}{3\pi}\right], \tag{5.13}$$

where the square brackets indicate that the integer part is to be taken. This

result does not compare well with our experimental observations however. Take the 5ml pool for example. We observe a combination of ellipse and triangle forms at $Bm = 50$. These correspond to $m = 2$ and 3. Formula 5.13 predicts that for this Bond number, the mode excited will be $m = 10$. Similarly the predictions made by equation (5.13) for the other pool volumes compare poorly with our observations.

5.3.3 Behaviour of pool which touches crucible walls at rest

Though not thoroughly investigated we observed interesting results when the pool volume is large enough so that the pool perimeter is in contact with the cruicible walls. We used a volume of 21ml of Ga-In-Sn. A photo of the pool at rest is given in Figure 5.16. This experiment is similar to that of Hinaje [2005]. A tin-lead alloy is used, and the crucible is larger than ours, its radius being 45.75mm. He also used a different field frequency of 3.7KHz. Despite these differences we expect that our pool of Ga-In-Sn will behave similarly to his pool of tin-lead alloy.

Repeating the same procedure as in the first experiment, we observe that the pool is squeezed away from the crucible walls and at $Bm_{crit0} = 53.03$ a combination of a square and pentagonal modes is observed. Some examples of this are given in Figure 5.17. As the pool extremities touch the walls of the crucible, the pool's oscillations are rather complex and we are unable to determine if the pool's oscillations were purely radial, or if rotation of the pool occurs as well. Increasing the magnetic field strength further we observe a symmetry break and the regular square and pentagon shapes become distorted and increasingly complex. At $Bm = 83.2$ we observe the formation of fingers which break the pool symmetry.

The pool shape becomes increasing complex taking on less symmetric forms until we reach a critical $Bm = Bm_{crit1} = 123.2$. At this point the pool takes on

a nearly static "croissant" form as shown in Figure 5.19. This resembles one of the stable forms observed by Hinaje [2005] in a pool of molten tin submitted to a medium frequency magnetic field. This shape does move slightly, but this croissant form is maintained for periods of a minute or so. This static "croissant" deformation seems to be quite stable. Increasing the magnetic field strength, we observe the same "croissant" form even at magnetic Bond numbers as high as $Bm = 212.7$. Joule heating made it difficult to adequately cool the pool at larger field strengths. Thus we were unable to observe the effect of larger Bm on the pool.

5.3.4 Effect of oxidation

The only stable static form we observed is that of the croissant shape; Hinaje [2005] however observed many other interesting morphologies. Towards the end of the experiment, we allowed the pool to oxidise and performed a brief third experiment to observe the effect of oxidation on the pool. As before, we use a pool volume of 21ml. Again the pool touches the crucible walls at rest. We allow the pool surface to oxidise by replacing the covering water-acid solution with water. The effect of oxidation is twofold; first it acts to lower the surface tension of the pool surface, second it forms a "crust" which tends to adhere to the crucible base reducing the mobility of the lower surface of the pool.

We observe results similar to those of Hinaje [2005]. Increasing Bm from zero we observe that the pool surface is deformed into increasingly irregular forms as observed by Hinaje [2005]. We first see the development of an indentation on the pool perimeter or an "opening" as Hinaje [2005] names it. We observed this at $Bm = 48.0$; a small indentation formed and grew inwards forming a cavity shaped like a pair of glasses as shown in Figure 5.20(b). As Bm increases the cavity is enlarged, eventually forming a "hammer" shape at $Bm = 51.8$ (see Figure 5.20(c)). The shape of the cavity becomes increasingly complex as we increase Bm, adding another lobe to the "hammer" at $Bm = 83.4$ (see

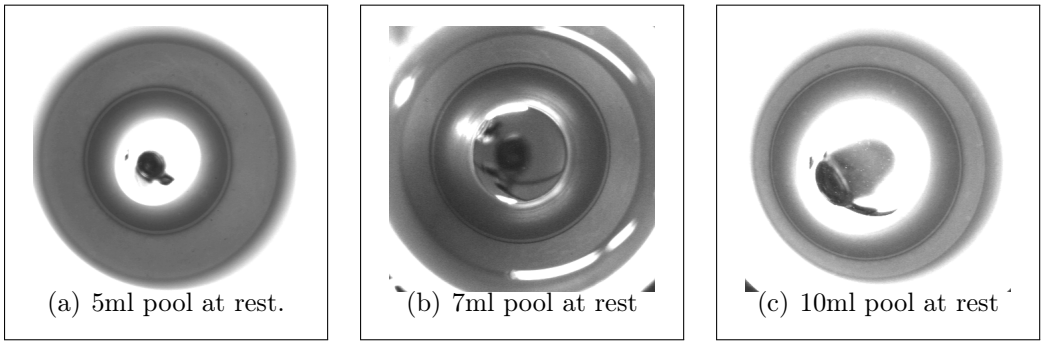

(a) 5ml pool at rest. (b) 7ml pool at rest (c) 10ml pool at rest

Figure 5.4: Photographs of the pools at rest.

Figure 5.20(d)). At higher values of Bm the channel becomes very complex forming a "horse" like shape at $Bm = 99.4$ (Figure 5.20(e)) and a "clover" at $Bm = 115.4$ (Figure 5.20(f)). We were unable to increase the field strength further as the oxidation of the drop became so severe that flakes of metal oxide quickly polluted the covering water making continued observation difficult.

5.4 Conclusion

Considering a simple pool geometry we have observed complicated coupled and non-linear phenomena. An initially circular pool is deformed into regular elliptic, triangular and square shapes which oscillate radially at a couple of hertz. Rotation of the pool is also observed. The oscillating pool stops oscillating and rotates about its centre for a few seconds, after which it either stops and resumes oscillating radially or rotates in the opposite direction.

The simplest behaviour was observed with the 7ml pool. Except when the field strength was small, the pool maintained a triangular shape which oscillates radially or rotates depending on the value of Bm. The 10ml pool exhibited the most complicated behaviour. As Bm increased it perimeter was deformed into both triangular and square shapes. We observe and intermediate regime where the pool alternately takes on both forms. Pool oscillation and rotation are observed for both the triangular and square shaped pool perimeters.

Although the mechanism behind both the radial oscillation of the pool perimeter and the pool rotation is not fully understood, we speculate that the observed phenomena are due to an instability which develops between the balance of surface tension and the electromagnetic force. The magnetic interaction parameter $\mathcal{N}$ is weak in our experiments which indicates that the alternating Lorentz force is unlikely to drive fluid motion directly as is the case with the "starfish" and "strip" experiments. The magnetic Bond number Bm, was typically $20 < Bm < 100$ when pool oscillation or rotation was observed. This indicates that while the electromagnetic force is dominant, the pool surface tension is not negligible, suggesting that the pool behaviour is due to an instability which develops in the balance between the two.

The model derived in Priede et al. [2006], does not compare well with our experiments. This is most likely due to their assumption that the fluid is a perfect conductor. In the present experiments, the so called skin depth δ_{mag} is similar to the pool depth.

We also observe similar phenomena to those presented by Hinaje [2005]. However we only observe the more complicated pool morphologies they observe when we allow our pool surface to oxidise. This suggests that oxidation may play some role in the results they present. We suppose that the complex morphologies they observe are caused by reduced surface tension due to oxidation of the surface of the liquid metal they use.

Using a relatively simple geometry, we have observed complicated free surface behaviour. Predications obtained from theoretical work does not compare well with our observations. Further experimental investigation is needed to understand the behaviour we have observed. Performing a similar experiment using a magnetic field of larger frequency would be interesting as the physics involved would be similar to those modelled by Priede et al. [2006].

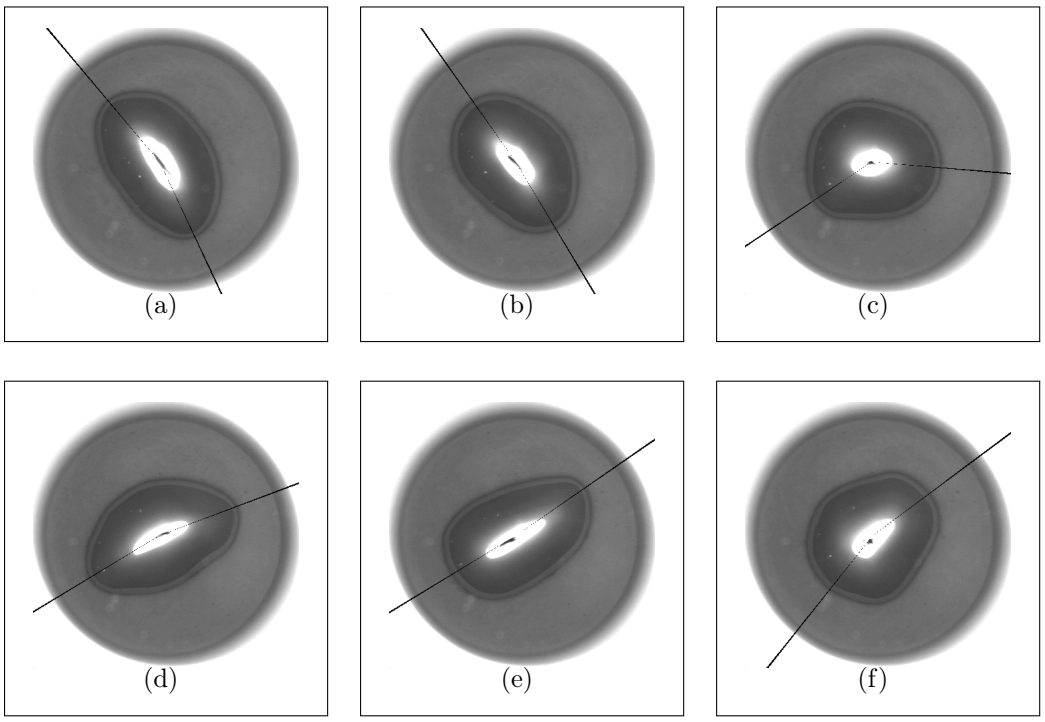

Figure 5.5: Elliptic radial oscillations of a 5ml pool at $Bm = 48.6$. Consecutive frames recorded at intervals of 7.5×10^{-2}s are shown in Figures 5.5(a) to 5.5(f). These show the elliptic contraction and expansion of the pool perimeter which is characteristic of the mode.

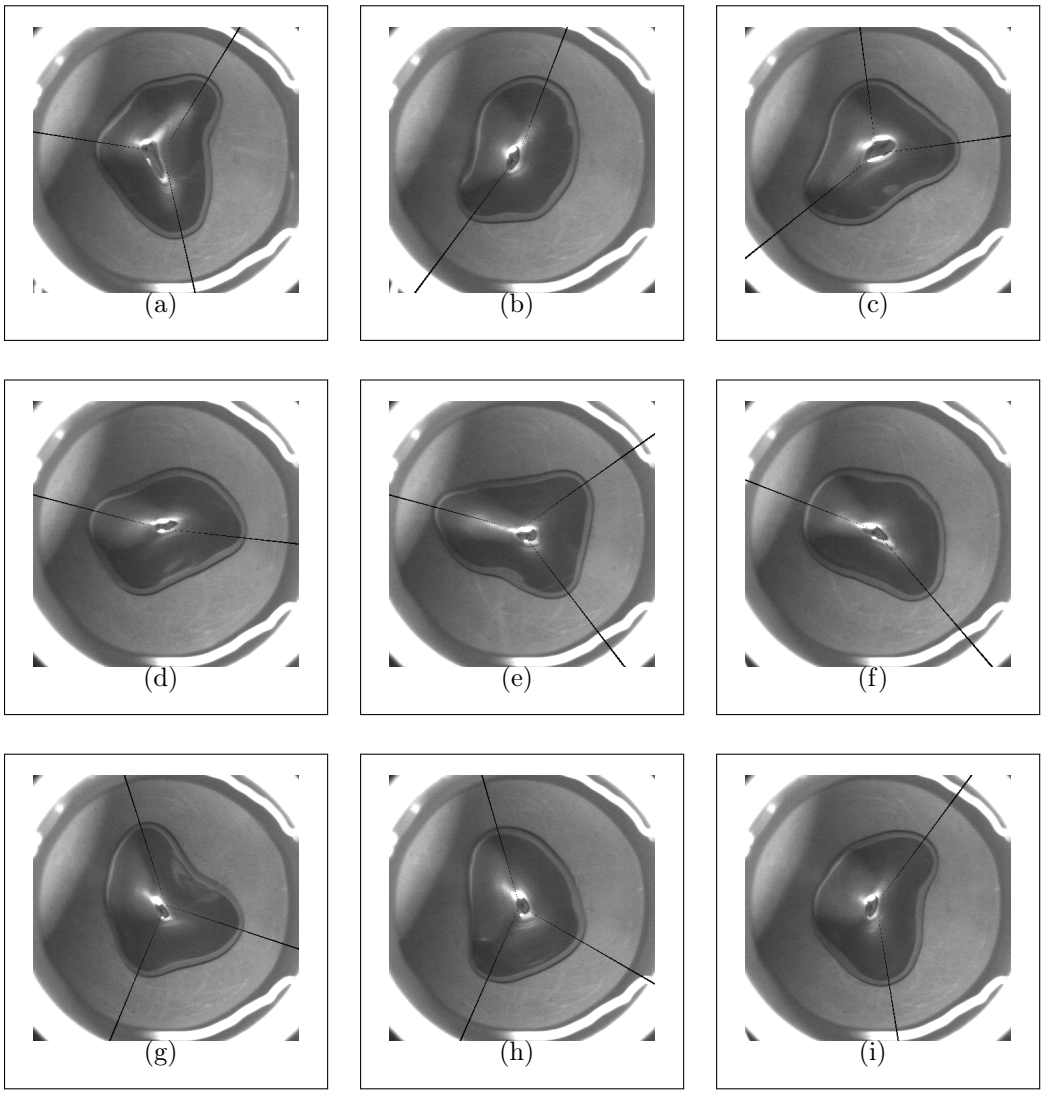

Figure 5.6: Combination of elliptic and triangular radial oscillations observed in a 5ml pool $Bm = 51.5$. Consecutive frames recorded at intervals of 7.5×10^{-2}s are shown in Figures 5.6(a) to 5.6(i).

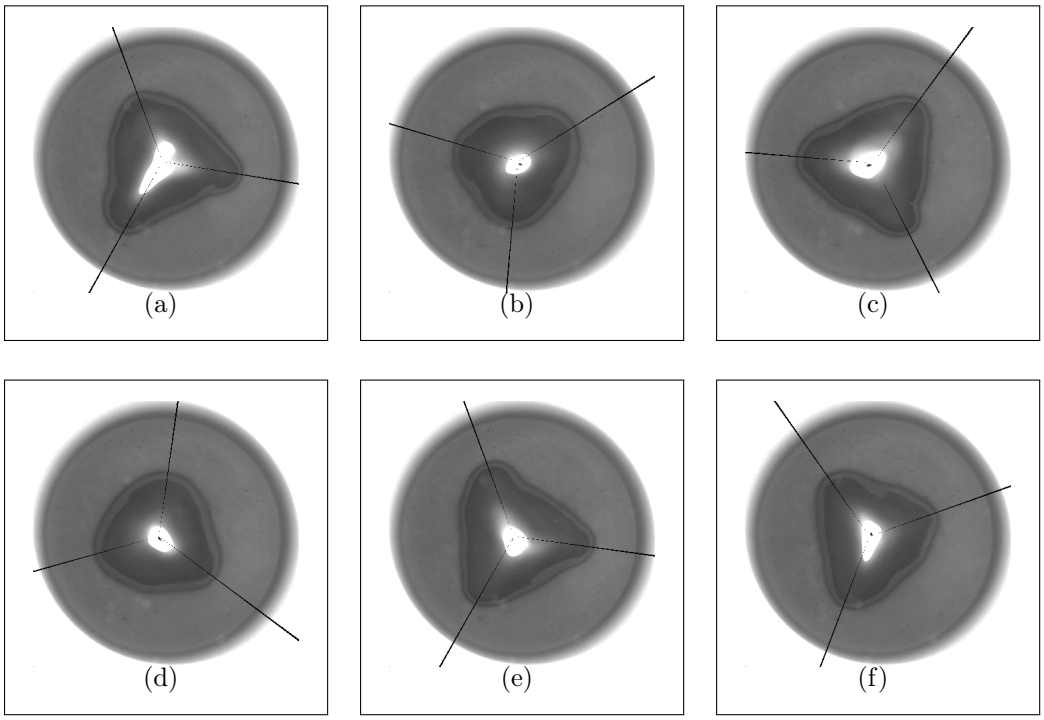

Figure 5.7: Triangular radial oscillations of a 5ml pool $Bm = 69.4$. Consecutive frames recorded at intervals of 7.5×10^{-2}s are shown in Figures 5.7(a) to 5.7(f). These show the contraction and expansion of the triangle shaped perimeter.

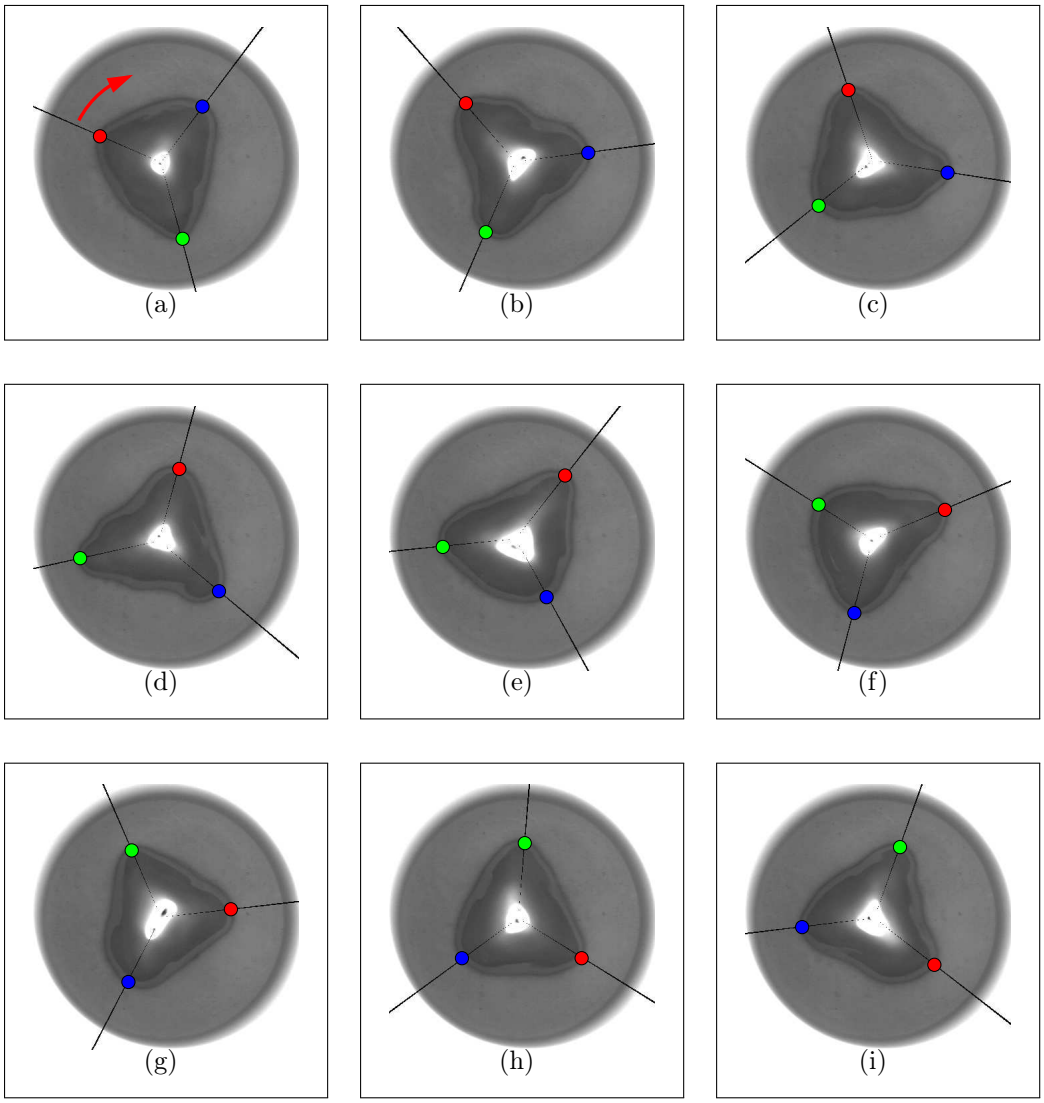

Figure 5.8: Rotating mode triangular mode observed in a 5ml pool $Bm = 71.2$. Consecutive frames recorded at intervals of 7.5×10^{-2}s are shown in Figures 5.8(a) to 5.8(i). The coloured dots track the rotation of the corners of the triangle shaped perimeter.

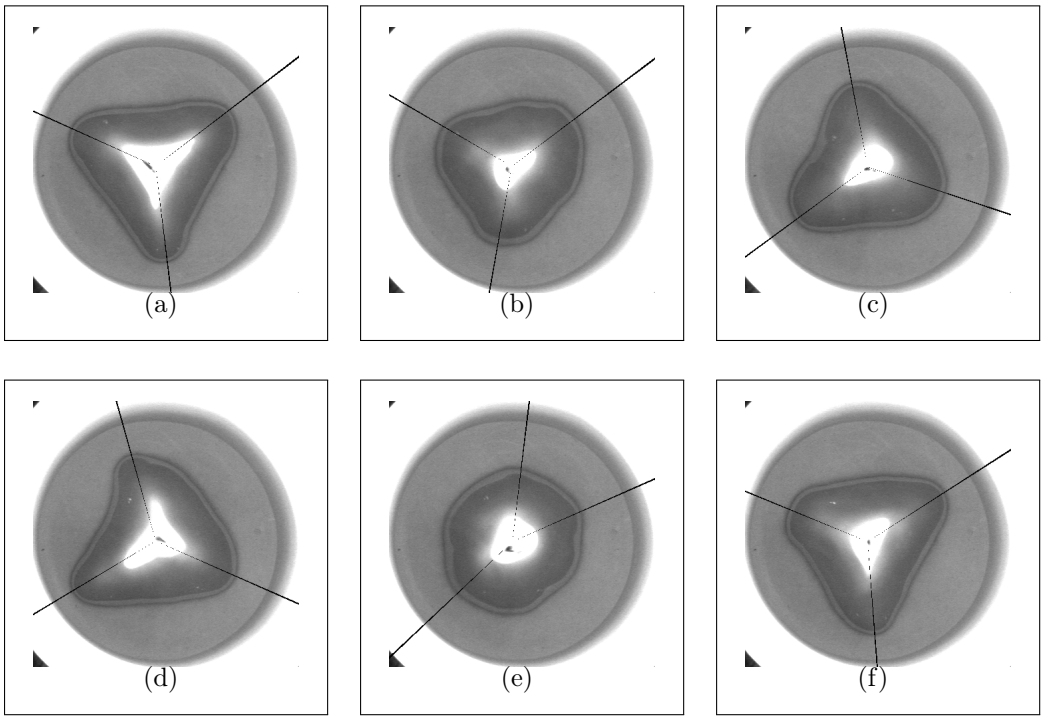

Figure 5.9: Triangular radial oscillations of a 7ml pool $Bm = 44.2$. Consecutive frames recorded at intervals of 7.5×10^{-2}s are shown in Figures 5.9(a) to 5.9(f). These show the contraction and expansion of the triangle shaped perimeter.

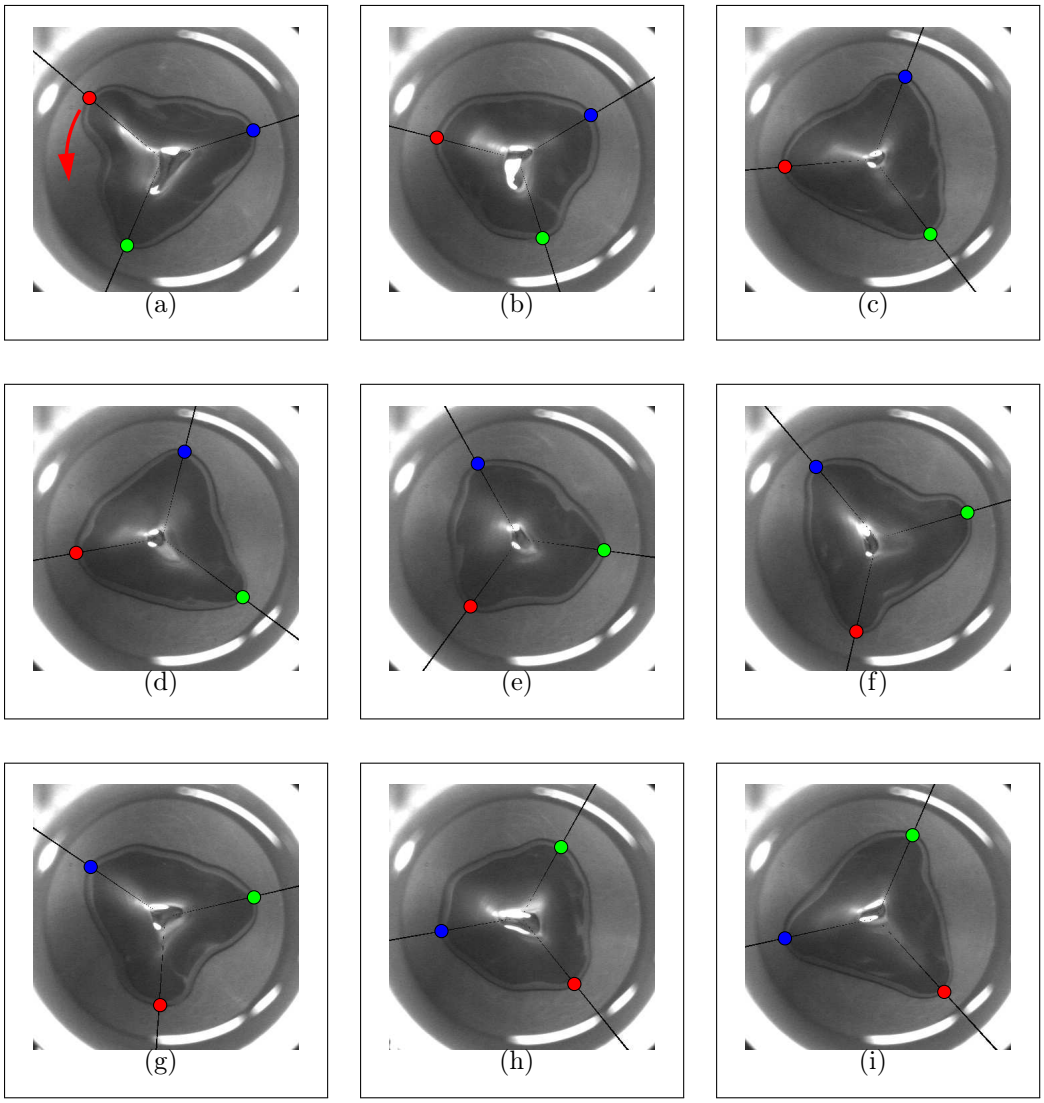

Figure 5.10: Rotating triangular mode observed in a 7ml pool $Bm = 57.5$. Consecutive frames recorded at intervals of 7.5×10^{-2}s are shown in Figures 5.10(a) to 5.10(i). The coloured dots track the rotation of the corners of the triangle shaped perimeter.

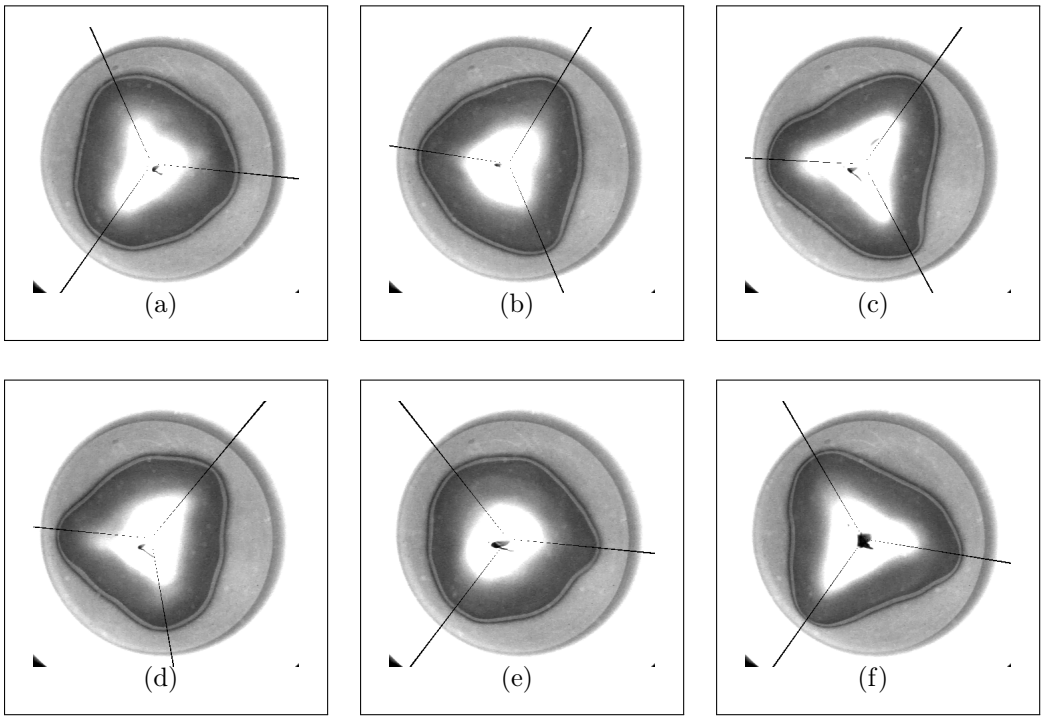

Figure 5.11: Triangular radial oscillations of a 10ml pool $Bm = 50.2$. Consecutive frames recorded at intervals of 7.5×10^{-2}s are shown in Figures 5.11(a) to 5.11(f). These show the contraction and expansion of the triangle shaped perimeter.

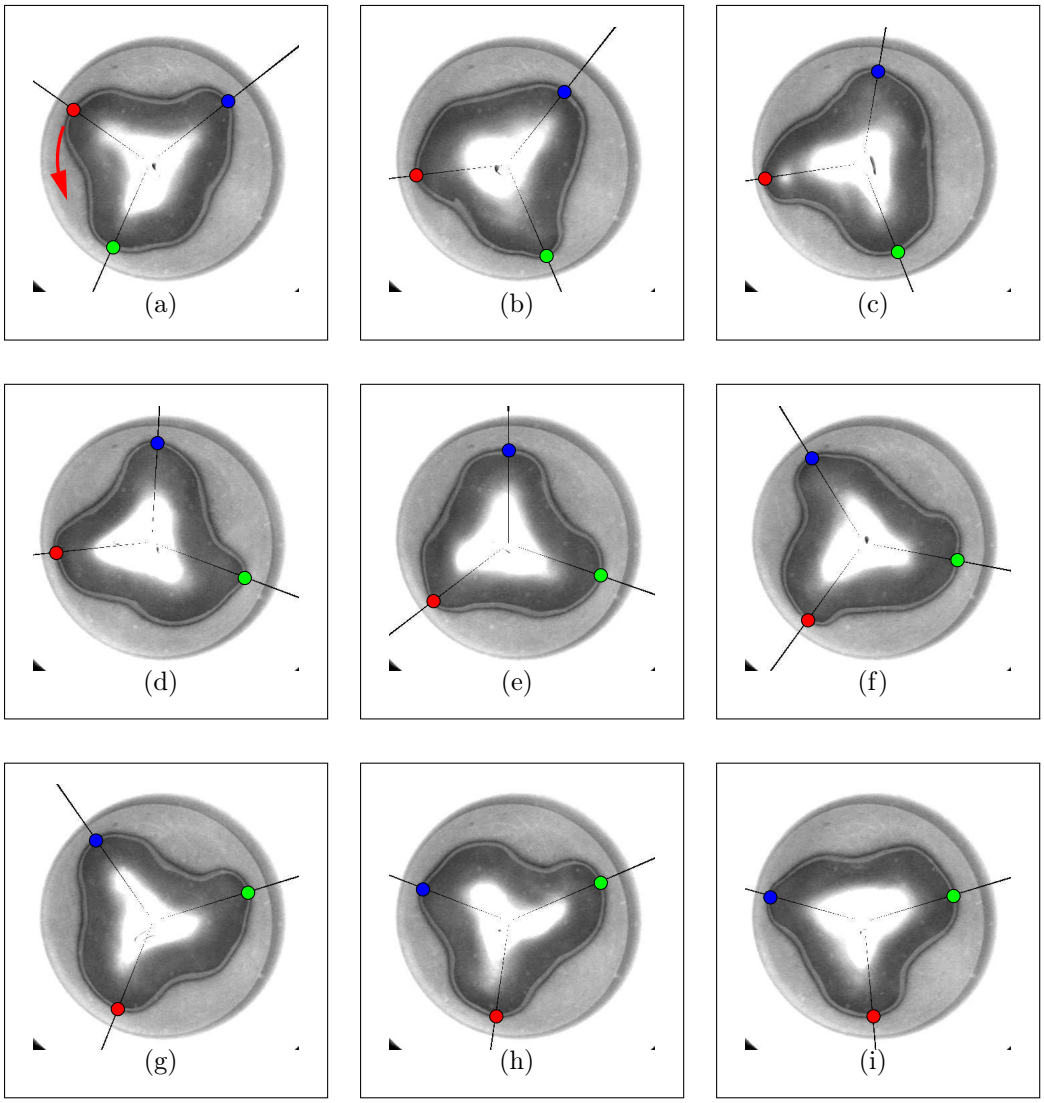

Figure 5.12: Rotating triangular mode observed in a 10ml pool $Bm = 63.3$. Consecutive frames recorded at intervals of 7.5×10^{-2}s are shown in Figures 5.12(a) to 5.12(i). The coloured dots track the rotation of the corners of the triangle shaped perimeter.

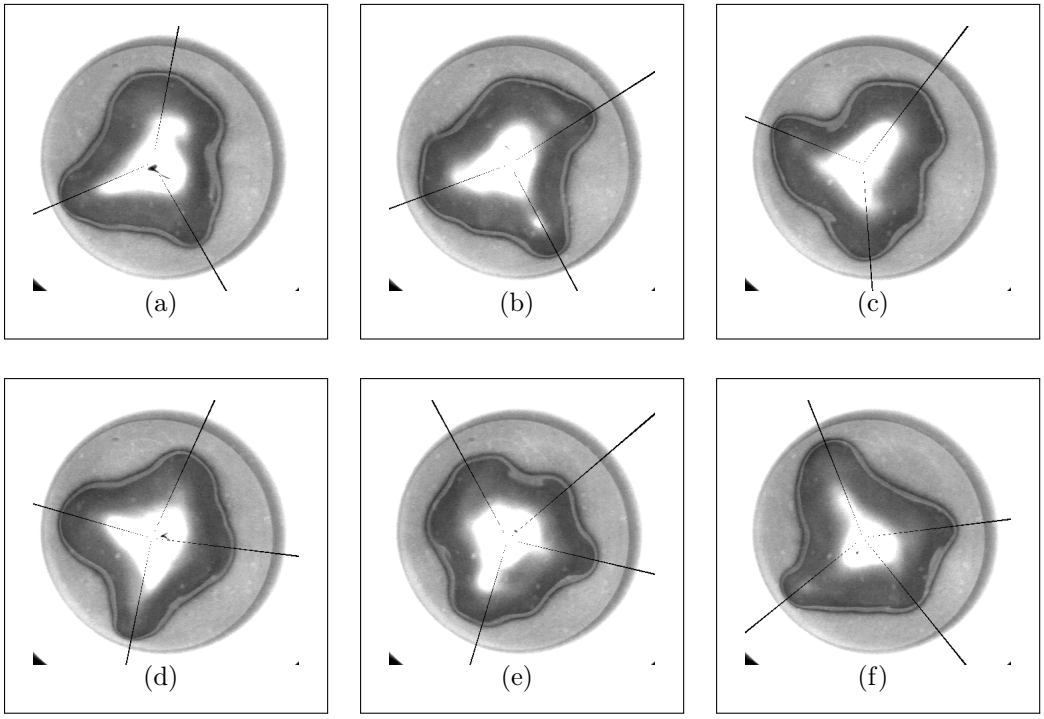

Figure 5.13: Combination of triangular and square radial oscillation of a 10ml pool $Bm = 74.3$. Consecutive frames recorded at intervals of 7.5×10^{-2}s are shown in Figures 5.13(f) to 5.13(f).

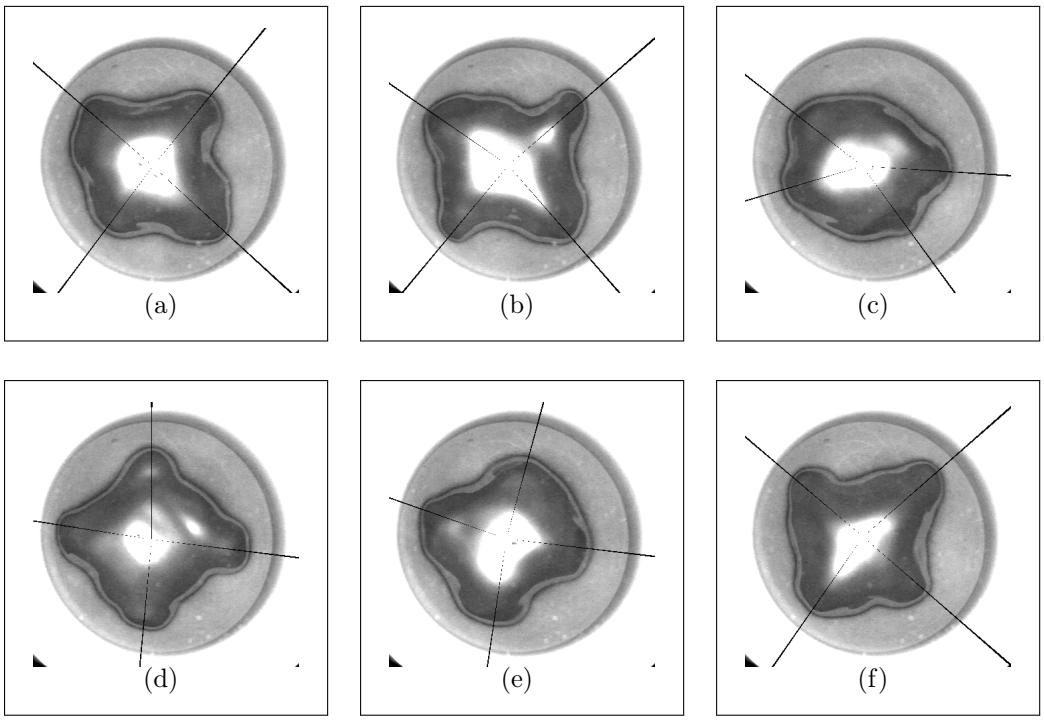

Figure 5.14: Square radial oscillations of a 10ml pool $Bm = 88.7$. Consecutive frames recorded at intervals of 7.5×10^{-2}s are shown in Figures 5.14(a) to 5.14(f). These show the contraction and expansion of the square perimeter.

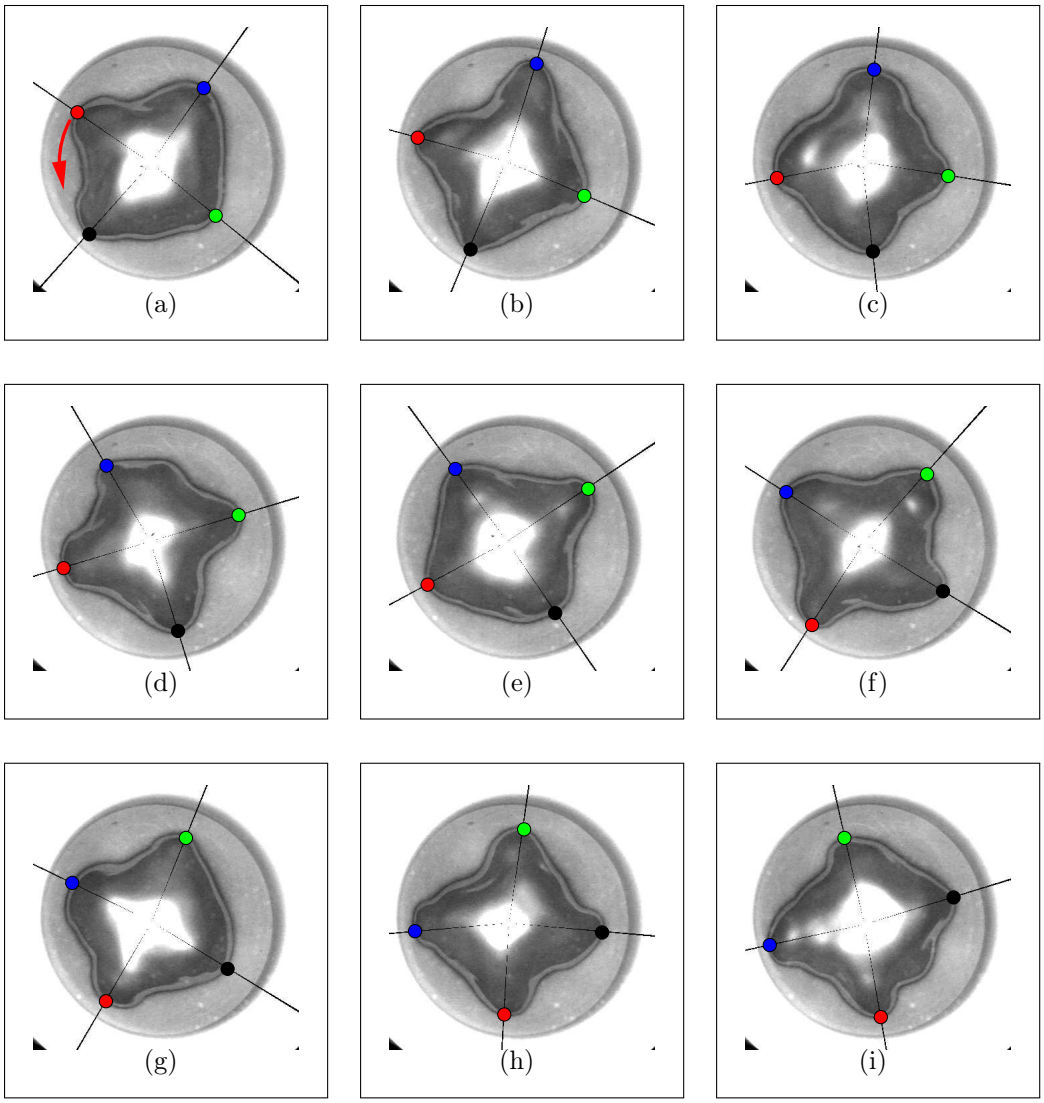

Figure 5.15: Rotating square mode observed in a 10ml pool $Bm = 88.7$. Consecutive frames recorded at intervals of 7.5×10^{-2}s are shown in Figures 5.15(a) to 5.15(i). The coloured dots track the rotation of the corners of the square perimeter.

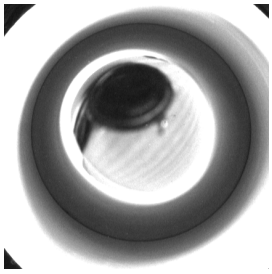

Figure 5.16: Photo of 21ml pool at rest.

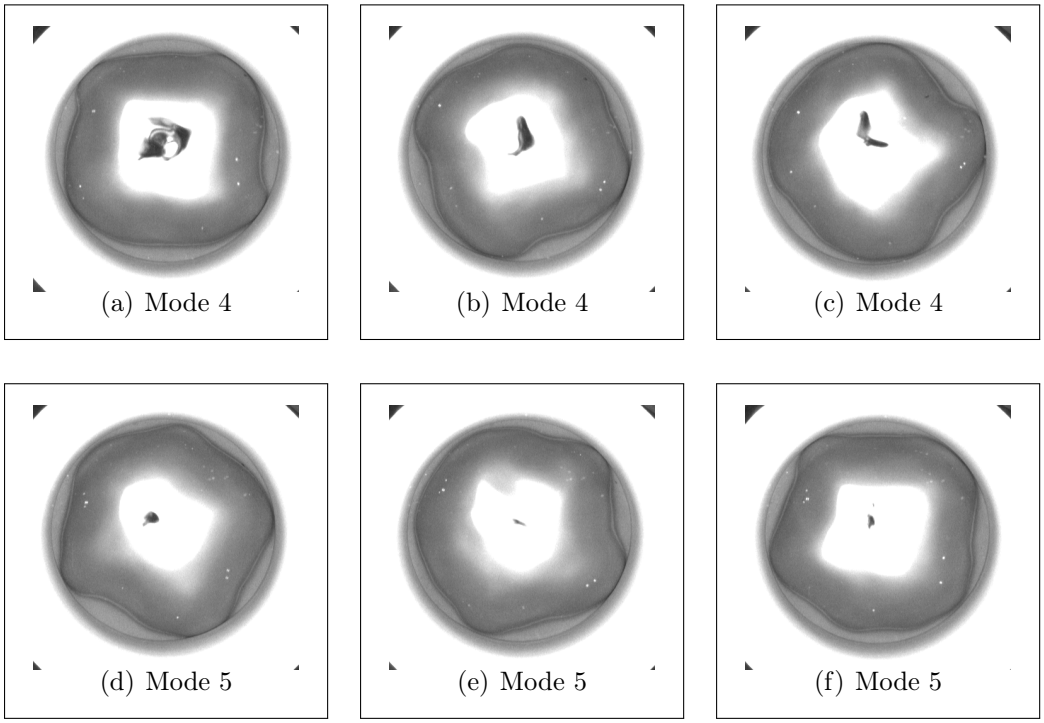

(a) Mode 4 (b) Mode 4 (c) Mode 4

(d) Mode 5 (e) Mode 5 (f) Mode 5

Figure 5.17: Square and pentagonal modes both observed at $Bm = 53.0$ on a pool which touches the sides of the crucible at rest.

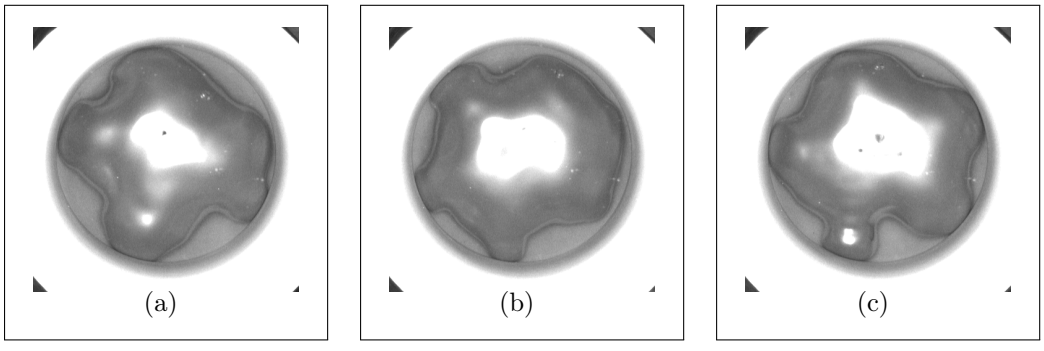

(a) (b) (c)

Figure 5.18: Increasing the field strength, pool forms become increasingly non-linear as can be seen in these examples recorded with $Bm = 83.2$.

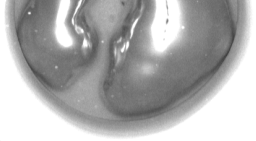

(a) Static "Croissant" form observed at $Bm = 123$.

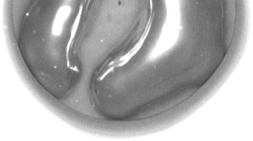

(b) Static "Croissant" form observed at $Bm = 123$.

(c) Static "Croissant" form observed at $Bm = 123$

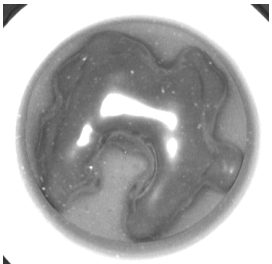

(d) Static "Croissant" form observed at $Bm = 156$.

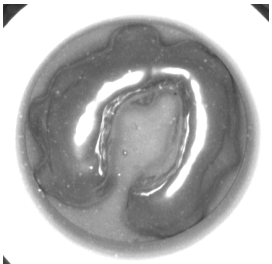

(e) Static "Croissant" form observed at $Bm = 156$.

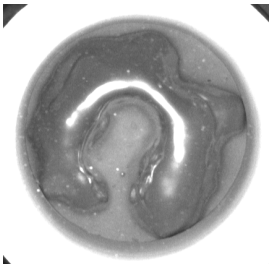

(f) Static "Croissant" form observed at $Bm = 156$.

Figure 5.19: Increasing the field strength, pool forms become increasingly non-linear as can be seen in these examples. Figures 5.19(a) to 5.19(c) are photos taken with $Bm = 123$. We observe the same "croissant" form at higher $Bm = 156$ in figures 5.19(d) to 5.19(f).

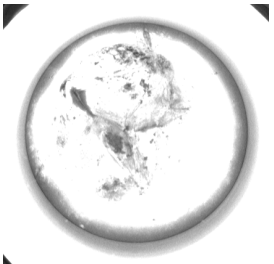

(a) Oxidised pool at rest.

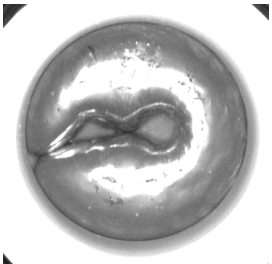

(b) Static "Glasses" form observed at $Bm = 48.1$.

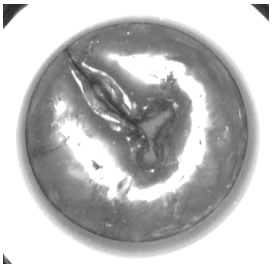

(c) Static "Hammer" form observed at $Bm = 51.8$.

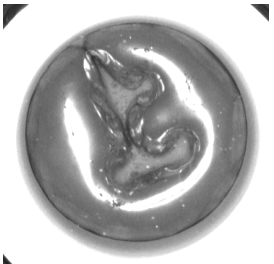

(d) Static "Hammer" form with additional lobe observed at $Bm = 83.4$.

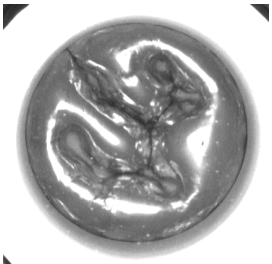

(e) Static "Horse" form observed at $Bm = 99.4$.

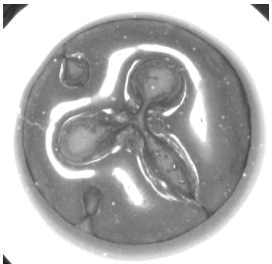

(f) Static "Clover" form observed at $Bm = 115.4$.

Figure 5.20: Examples of static free surface deformation of a pool of oxidised Ga-In-Sn.

Chapter 6

High-frequency fields and the Phase-field method

6.1 Introduction

High-frequency magnetic fields are used in many industrial processes associated with metallurgy such as levitation melting and cold crucible processing. Such processes are often subject to instabilities which limit their efficiency. In this chapter we present a preliminary investigation of a "phase field" method which could be used to model these problems. In contrast to theory for the "strip" and "starfish" problems, the work we present in this chapter considers a purely numerical approach, and we consider a different geometry from the problems we investigated in the previous chapters.

The general problem is as follows: a liquid metal is submitted to a high-frequency magnetic field

$$\mathbf{B} = \mathrm{Re}\left\{\mathbf{B}_0 e^{i2\pi f t}\right\} \tag{6.1}$$

of frequency f and amplitude $|\mathbf{B}_0|$, and whose orientation is that of $\mathbf{B}_0$. $\mathbf{B}$ penetrates a relatively small distance

$$\delta_B = \frac{1}{\sqrt{\pi\mu\sigma f}} \tag{6.2}$$

into the conductor. This is commonly known as the skin effect (Davidson [2001] gives an explanation of this effect) as effect of $\mathbf{B}$ may be considered as a pressure

$$p_{mag} = \frac{B^2}{4\mu_0} \tag{6.3}$$

on the conductor's surface. When coupled with surface tension

$$p_\gamma = \gamma\kappa, \qquad \kappa = \text{ curvature}, \tag{6.4}$$

the total pressure $\kappa\gamma + p_{mag}$ will determine the equilibrium shape of the conductor. This configuration may not be stable however. Additionally the fluid flow in the conductor is complicated and possibly unstable (Sneyd [1979]).

A great deal of analytic work has been done on the problem. A general

formulation of the combined high-frequency electromagnetic and fluid dynamic problem is given by Sneyd [1979]. Shercliff [1981] calculates the static shape of molten metal columns in both a uniform and quadrupole magnetic field assuming that the field does not penetrate into the metal.

Sneyd and Moffatt [1982] consider the more complicated case of an initially solid cylindrical cylindrical conductor which is melted in a high frequency magnetic field which levitates it. They establish an energy principle and use it to calculate the equilibrium shape of the molten metal free surface. Similar work has been performed by Mestel [1982]. He analyses the free-surface perturbation to an initially spherical liquid conductor submitted to an axisymmetric field.

Instabilities present in levitation melting and cold-crucible processing are considered by Priede and Gerbeth (Priede and Gerbeth [2000a], Priede and Gerbeth [2000b], Priede and Gerbeth [2005])). Using both numerical and analytical approaches they consider the rotational and oscillatory stability of a solid sphere which is levitating by various field configurations. A different approach is taken by Conrath and Karcher [2005]. They study the shaping of liquid metal pool. Their analysis is limited by their assumption that the pool does not perturb the magnetic field.

These analytic and semi analytic methods are limited as they are generally unable to take large free surface deformations and/or complicated fluid flow into account. Thus it is of interest to investigate these processes using entirely numerical models. This chapter is concerned with the problem of taking large deformations of a conductor surface into account. We consider a different problem from the previous chapters, namely the effect of a high-frequency (HF) magnetic field on the surface of a conductor. We modify the Allen-Cahn phase-field method (Allen and Cahn [1979]) to compute the equilibrium shape of the free-surface in two simple problems:

- the equilibrium shape of the cross-section of an infinitely long pool resting

on a substrate subject to gravity and surface tension,

- the equilibrium shape of the cross-section of a conducting column submitted to a high frequency magnetic field whose field lines are parallel far from the column.

The geometry of the first problem we consider is given in Figure 6.1. An infinite strip of liquid resting on a substrate is subject to a gravitational field $\mathbf{g}$. The field $\mathbf{g}$ is uniform and acts down the y axis i.e $\mathbf{g} = -g\widehat{\mathbf{y}}$, where $\widehat{\mathbf{y}}$ is a the unit vector along the y axis. Gravitation will tend to flatten the column against a substrate which we place in the (x, z) plane at $y = 0$. The static form is determined by the balance of surface tension due to the curvature of the column's surface and gravitation. This balance leads to the Young-Laplace equation (Paddey [1969])

$$\rho g y = \gamma \kappa \tag{6.5}$$

where

$$\kappa = \nabla \cdot \widehat{\mathbf{n}} \tag{6.6}$$

is the curvature of the column surface and $\widehat{\mathbf{n}}$ is a unit normal pointing outwards from the surface.

The geometry of the second problem we consider is given in Figure 6.2. We consider a simple field configuration similar to one studied by Shercliff [1981] i.e. an infinite column of conducting fluid submitted to a parallel uniform magnetic field. The Lorentz force due to the interaction of the induced current in the column will tend to deform the the column cross-section. For weak magnetic fields, Shercliff [1981] showed that the circular cross section is deformed into an ellipse.

While a variety of computational methods exist to solve these problems our motivation for studying the phase field method is that it avoids the difficulties inherent in traditional moving mesh approaches. The phase-field method represents the surface movement as a vector field confined to a thin band in

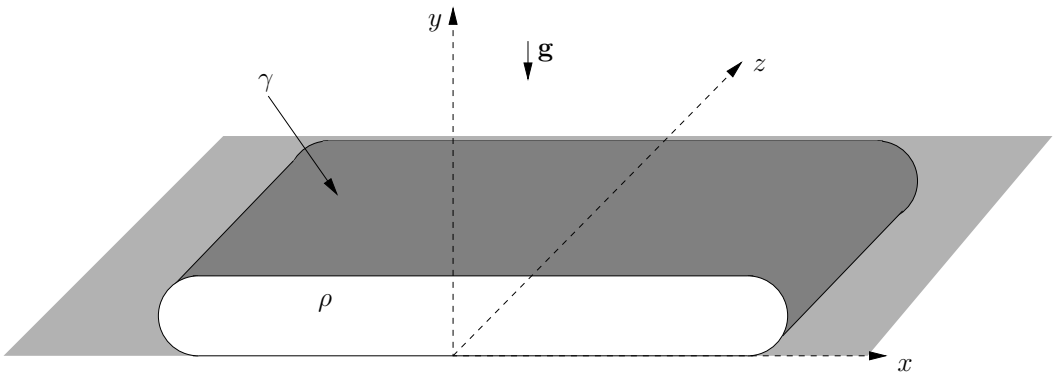

Figure 6.1: Sketch of static shape of a column submitted to a uniform horizontal gravitational field.

which the surface resides. This allows a fixed mesh to be used and avoids the difficulties which are inherent in any moving mesh scheme.

Other methods similar to the phase-field method include the level set (Sethian [1999]), VOF (Hirt and Nichols [1981])and front tracking (Popinet and Zaleski [1999]) methods. Unlike the phase-field method, these do not treat the discretisation uniformly on the whole domain which complicates their formulation. Front tracking requires that an additional Riemann problem be solved to communicate information across the interface. The level set and VOF methods require renormalisation of the indicator function at each time step. This artificially damps the surface motion.

6.2 Phase-field formulation

The phase-field method is also a level-set method (Du et al. [2005]) but the surface motion may be viewed as the dissipation of the phase field's free energy $\mathcal{F}$. If we wish to consider surface tension, the value of $\mathcal{F}$ represents different interfacial energies associated with the phase field. The simplest functional one may consider is:

$$\mathcal{F} = \int_V W(\psi) + \alpha \frac{|\nabla \psi|^2}{2} \mathrm{d}V. \tag{6.7}$$

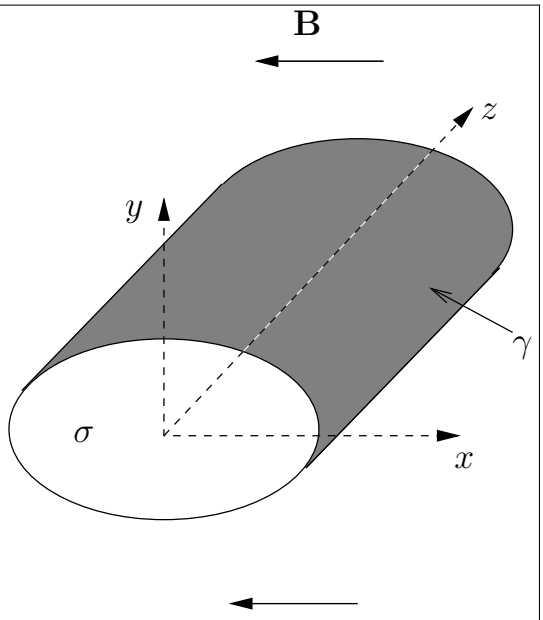

Figure 6.2: Sketch of static shape of a column submitted to a parallel uniform magnetic field.

The function $W(\psi)$ is chosen so that it penalises for values out of phase, while the gradient term penalises for large transition interfaces. If we choose the values of $\psi = 1$ to denote our conductor region and the value of $\psi = -1$ to denote the surrounding air, then the function W is as follows:

$$W(\psi) = \beta\left(1-\psi^2\right)^2/4 \tag{6.8}$$

where β is an arbitrary positive constant. This function which is plotted in Figure 6.3 with $\beta = 1$, is positive for all values of ψ except ± 1 where it is zero. If ψ obeys a steepest descent law with respect to $\mathcal{F}$, we recover the Allen-Cahn equation:

$$\frac{\partial \psi}{\partial t} = -\frac{\delta \mathcal{F}}{\delta \psi}. \tag{6.9}$$

Thus we model a two fluid system using a phase function ψ to identify the coexisting fluids as shown in Figure 6.4. ψ takes on discrete values, ± 1 say, for each of the two fluids. Any intermediate value will indicate the proximity of an interface.

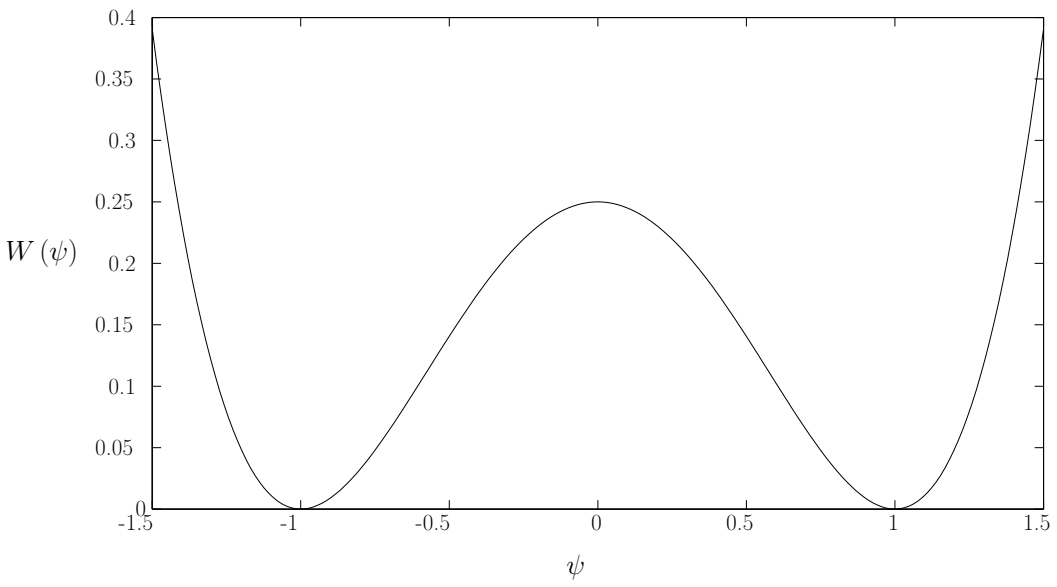

Figure 6.3: Plot of $W(\psi)$

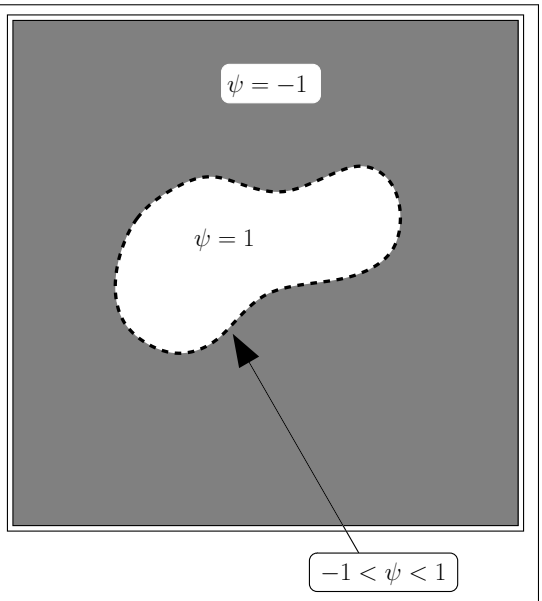

Figure 6.4: A diagram showing how a phase function ψ may be used to model an interface between two fluids. One fluid (grey) corresponds to regions in the domain where $\psi = -1$, the other (white) where $\psi = 1$. In the diffuse interface between the two $-1 < \psi < 1$.

And in order to conserve the volume of both phases we must impose the volume constraint:

$$\int_V \psi \mathrm{d}V = \mathcal{V} \tag{6.10}$$

where $\mathcal{V}$ is a constant whose value is determined by conservation of the volumes of the two fluids.

To give a physical interpretation to the constants α and β consider the simple case where ψ does not vary in the x and y direction and varies only in the z direction, with the boundary conditions:

$$\psi\left(z = -\infty\right) = -1 \text{ and} \tag{6.11}$$

$$\psi\left(z = \infty\right) = 1. \tag{6.12}$$

In this simple one-dimensional case the free energy 6.7 is simply:

$$\mathcal{F} = \int_{z=-\infty}^{\infty} W\left(\psi\right) + \frac{\alpha}{2}\left(\frac{\partial \psi}{\partial z}\right)^2 \mathrm{d}z. \tag{6.13}$$

We assume that the system is at equilibrium, i.e $\mathcal{F}$ is at a minimum. This implies that

$$\frac{\delta \mathcal{F}}{\delta \psi} = \frac{\partial W\left(\psi\right)}{\partial \psi} - \alpha \frac{\partial^2 \psi}{\partial z^2} = 0. \tag{6.14}$$

This may be integrated once with respect to ψ to yield:

$$\frac{\alpha}{2}\left(\frac{\partial \psi}{\partial z}\right)^2 = W\left(\psi\right), \tag{6.15}$$

which has solution:

$$\psi\left(z\right) = \tanh\left(\frac{z}{\delta_\psi}\right) \tag{6.16}$$

where

$$\delta_\psi = \sqrt{\frac{2\alpha}{\beta}} \tag{6.17}$$

is the interface thickness which we define as the distance which comprises 95% of the variation of ψ. The surface tension κ due to the presence of the diffuse

interface is just the free energy 6.13 of the equilibrium solution 6.16

$$\kappa = \frac{2}{3}\sqrt{\frac{2\alpha}{\beta}}. \tag{6.18}$$

Including gravity and magnetic field

We consider the effect of gravitational and/or an electromagnetic field by adding the gravitational and electromagnetic energy to the free energy 6.7:

$$\mathcal{F} = \int_V W(\psi) + \alpha\frac{|\nabla\psi|^2}{2} + \phi(\psi)\,\mathrm{d}V \tag{6.19}$$

where

$$\phi(\psi) = \rho(\psi)\,gz + \frac{B^2}{2\mu_0} \tag{6.20}$$

is the sum of the gravitational and electromagnetic energies. Now:

$$\frac{\delta F}{\delta\psi} = \frac{\partial W(\psi)}{\partial\psi} - \alpha\nabla^2\psi + \frac{\partial\phi}{\partial\psi} \tag{6.21}$$

where

$$\frac{\partial\phi}{\partial\psi} = \frac{\partial\rho(\psi)}{\partial\psi}gz + \frac{1}{\mu_0}\mathbf{B}\cdot\frac{\partial\mathbf{B}}{\partial\psi}. \tag{6.22}$$

Substitution into 6.9 give us the following evolution equation for the phase function ψ

$$\frac{\partial\psi}{\partial t} = \alpha\nabla^2\psi - W' - \phi' \tag{6.23}$$

where the primes W', ϕ' etc denote partial derivatives $\frac{\partial W}{\partial\psi}$, $\frac{\partial\phi}{\partial\psi}$ with respect to ψ.

We now need to define the fluid density ρ and conductivity σ in terms of the phase function ψ. One possibility is

$$\rho = \rho_0 p(\psi), \qquad \sigma = \sigma_0 p(\psi). \tag{6.24}$$

where

$$p(\psi) = \frac{1}{16}(1+\psi)^3\left(8 - 9\psi + 3\psi^2\right). \tag{6.25}$$

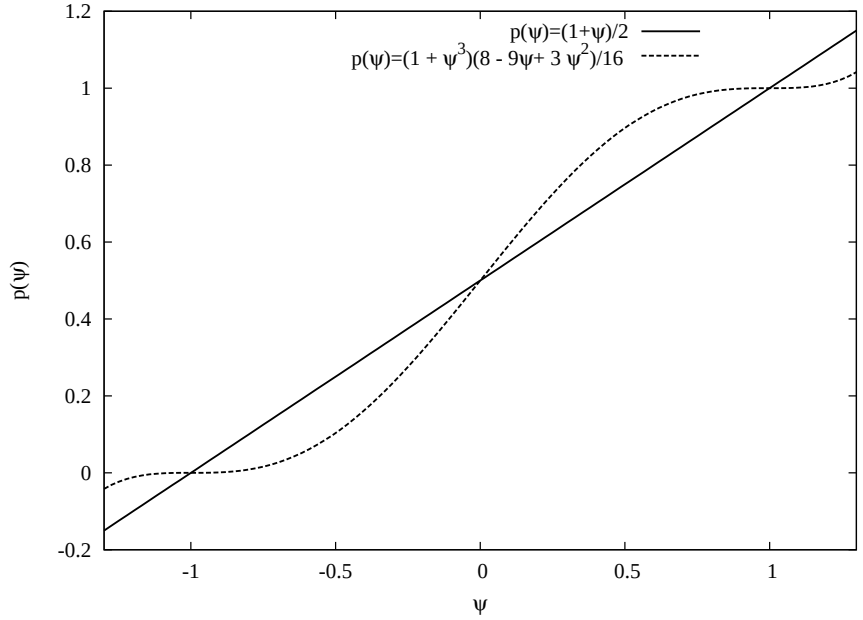

Figure 6.5: Comparison of two possible choices of $p(\psi)$, a linear relationship and a quintic relationship.

In the course of our numerical experiments, we found that this choice of function for p gave better results than a straightforward linear relationship such as

$$p\left(\psi\right) = \left(\psi + 1\right)/2. \tag{6.26}$$

When we used this linear relationship (6.26) we observed that the phase field ψ took on values larger than 1 or less than -1 due to accumulated numerical errors. Unfortunaly this corresponds to unphysical, and possibly negative values of ρ and σ. We found that this problem was resolved when we used the quitic (6.25). This is most likely becuase of two features of this quintic: its slope is zero at $\psi = 1$ and $\psi = -1$, and the graph of $p(\psi)$ (see figure 6.5) remains flat for values of ψ slightly larger than 1 or slightly less than -1.

6.3 Electromagnetic calculation

An arbitrary shaped column with conductivity σ_0 is placed in an alternating magnetic field $\mathrm{Re}\left\{\mathbf{B}e^{ß\omega t}\right\}$ where $\mathbf{B}$ is the amplitude of the field and ω the field frequency. We calculate $\mathbf{B}$ using what is known as the A^* formulation. We use a modified vector potential $\mathbf{A}^*$ such that

$$\frac{\partial \mathbf{A}^*}{\partial t} = \nabla V + \frac{\partial \mathbf{A}}{\partial t}, \tag{6.27}$$

where $\mathbf{A}$ is the usual vector potential for the magnetic field $\mathbf{B}$,

$$\mathbf{B} = \nabla \times \mathbf{A} = \nabla \times \mathbf{A}^*, \tag{6.28}$$

and V is the scalar electric potential. The induction equation may be written in terms of $\mathbf{A}^*$ as:

$$\nabla \times \nabla \times \mathbf{A}^* = -i\omega\mu_0\sigma(\psi)\mathbf{A}^*. \tag{6.29}$$

The derivative $\frac{\partial \mathbf{B}}{\partial \psi}$ may be deduced from equation (6.28):

$$\frac{\partial \mathbf{B}}{\partial \psi} = \nabla \times \frac{\partial \mathbf{A}^*}{\partial \psi} \tag{6.30}$$

and from equation (6.29)

$$\nabla \times \nabla \times \frac{\partial \mathbf{A}^*}{\partial \psi} = -i\omega\mu_0 \left(\frac{\partial \sigma}{\partial \psi}\mathbf{A}^* + \sigma \frac{\partial \mathbf{A}^*}{\partial \psi} \right). \tag{6.31}$$

To calculate the electromagnetic contribution to equation (6.23) we first need to solve the induction equation (6.29) so that we can calculate $\mathbf{B}$. Then we solve equation (6.31) for $\frac{\partial \mathbf{A}^*}{\partial \psi}$ so that we can calculate $\frac{\partial \mathbf{B}}{\partial \psi}$.

6.4 2D model

In two dimensions x and y say the vector potential $\mathbf{A}^*$ reduces to a scalar potential ξ such that:

$$\mathbf{A}^* = \xi\widehat{\mathbf{z}}. \tag{6.32}$$

The induction equation (6.29) becomes:

$$\nabla^2\xi = i\omega\mu_0\sigma\xi, \tag{6.33}$$

likewise equation (6.31) becomes:

$$\nabla^2\frac{\partial\xi}{\partial\psi} = i\mu_0\omega\left(\frac{\partial\sigma}{\partial\psi}\xi + \sigma\frac{\partial\xi}{\partial\psi}\right). \tag{6.34}$$

To solve this and Allen-Cahn equation (6.23) numerically we approximate the Laplacian operator using a so called "Mehrstellen" (Patra and Karttunen [2006], Collatz and Williams [1960]) discretisation. This is the same approach Jacqmin [1999] uses to solve the Cahn-Hillard equation coupled with the Navier-Stokes equation.

6.5 Mehrstellen discretisation

In a two dimensional square grid with spacing h, there are two possible discretisations of the Laplacian:

$$\nabla^2 f(x,y) = L \cdot f(x_i, y_j) + O(h^2). \tag{6.35}$$

The first is the well known five point discretisation:

$$L_5 = \frac{1}{h^2}\begin{bmatrix} 0 & 1 & 0 \\ 1 & -4 & 1 \\ 0 & 1 & 0 \end{bmatrix} \tag{6.36}$$

The second is the "Mehrstellen" nine point discretisation:

$$L_9 = \frac{1}{6h^2}\begin{bmatrix} 1 & 4 & 1 \\ 4 & -20 & 4 \\ 1 & 4 & 1 \end{bmatrix} \tag{6.37}$$

The L_9 discretisation is isotropic, i.e. the leading term in its truncation error

$$\frac{h^2}{12}\nabla^4 f(x,y) + O(h^4)$$

has no preferred direction. In the same way as Jacqmin [1999], we make use of this to derive a fourth order differencing scheme. Consider Poisson's equation:

$$\nabla^2 f(x,y) = \rho(x,y). \tag{6.38}$$

Approximating the Laplacian with the "Mehrstellen" operator:

$$L_9 f(x_i,y_j) = \nabla^2 f(x,y) + \frac{h^2}{12}\nabla^2\rho(x,y) + O(h^4). \tag{6.39}$$

Now evaluating $\nabla\rho(x,y)$ using the standard L_5 discretisation one finds that

$$\frac{h^2}{12}\nabla^2\rho(x,y) = \frac{h^2}{12}L_5\rho(x_i,y_j) + O(h^4). \tag{6.40}$$

Now combining equations (6.39) and (6.40) we obtain the fourth order discretisation of the Laplacian of f

$$L_9 f(x_i,y_j) - \frac{h^2}{12}L_5\rho(x_i,y_j) = \nabla^2 f(x,y) + O(h^4). \tag{6.41}$$

Now applying this discretisation to equation (6.33):

$$\nabla^2\xi = L_9\xi - i\omega\mu_0\frac{h^2}{12}L_5(\sigma\xi) + O(h^4), \tag{6.42}$$

so to $O(h^4)$

$$L_9\xi + i\omega\mu_0\frac{h^2}{12}L_5(\sigma\xi) + i\omega\mu_0\sigma\xi = 0. \tag{6.43}$$

Writing in stencil form and simplifying:

$$\frac{1}{6h^2}\begin{bmatrix}1 & 4 & 1\\ 4 & -20 & 4\\ 1 & 4 & 1\end{bmatrix}\xi_{i,j} + i\omega\mu_0\frac{1}{12}\begin{bmatrix}0 & 1 & 0\\ 1 & 8 & 1\\ 0 & 1 & 0\end{bmatrix}(\sigma_{i,j}\xi_{i,j}) = 0. \tag{6.44}$$

Discretising equation (6.34) in the same way we obtain:

$$\frac{1}{6h^2}\begin{bmatrix}1 & 4 & 1\\ 4 & -20 & 4\\ 1 & 4 & 1\end{bmatrix}\xi'_{i,j} + i\omega\mu_0\frac{1}{12}\begin{bmatrix}0 & 1 & 0\\ 1 & 8 & 1\\ 0 & 1 & 0\end{bmatrix}\left(\sigma'_{i,j}\xi_{i,j} + \sigma_{i,j}\xi'_{i,j}\right) = 0. \tag{6.45}$$

Similarly for the Allen-Cahn equation (6.23) we obtain:

$$\alpha\frac{1}{6h^2}\begin{bmatrix}1 & 4 & 1\\ 4 & -20 & 4\\ 1 & 4 & 1\end{bmatrix}\psi^n_{i,j} - \frac{1}{12}\begin{bmatrix}0 & 1 & 0\\ 1 & 8 & 1\\ 0 & 1 & 0\end{bmatrix}\Gamma^n_{i,j} = 0, \tag{6.46}$$

where

$$\Gamma^n_{i,j} = \dot{\psi}^n_{i,j} + W'\left(\psi^n_{i,j}\right) + \phi^{n\prime}\left(\psi^n_{i,j}\right), \tag{6.47}$$

and n indicates the time at time step n $t^n = n\Delta t$. We approximate the time derivative $\dot{\psi}$ at time t^n say with the first order backward difference:

$$\dot{\phi}_{i,j}\left(t_n\right) = \frac{\psi^n_{i,j} - \psi^{n-1}_{i,j}}{\Delta t}. \tag{6.48}$$

Combining equation (6.47) and (6.48) we obtain

$$\Gamma^n_{i,j} = \frac{\psi^n_{i,j} - \psi^{n-1}_{i,j}}{\Delta t} + W'\left(\psi^n_{i,j}\right) + \phi\left(\psi^n_{i,j}\right). \tag{6.49}$$

The finite difference equations resulting from equations (6.46) and (6.49) are non-linear and difficult to solve. Newton-Raphson iteration may be used, which we used initially. Convergence was difficult to achieve and was extremely slow. However we found after much experimentation that performing a zeroth order

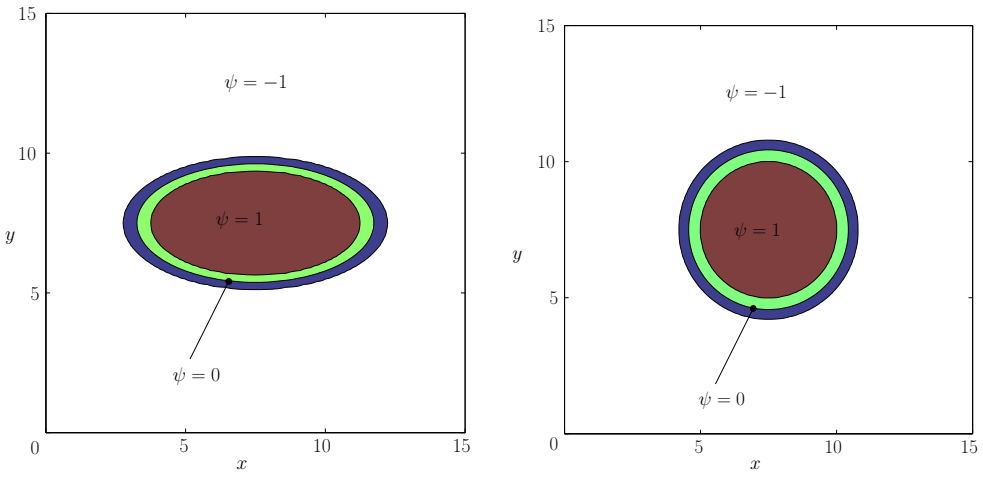

(a) Initial elliptic shape of a liquid column. (b) Final circular shape of a liquid column

Figure 6.6: The equilibrium shape of an initially elliptic column of liquid.

linearisation of the non-linear terms $W'\left(\psi_{i,j}^{n}\right)$ and $\phi\left(\psi_{i,j}^{n}\right)$ by replacing them with their values calculated at the previous time step: $W'\left(\psi_{i,j}^{n-1}\right)$ and $\phi\left(\psi_{i,j}^{n-1}\right)$ did not change the final static form of ψ calculated.

6.6 Results

6.6.1 No external field

In the absence of an external field, we expect that surface tension will tend to deform a liquid column of arbitrary cross-section to a circle. Starting with an elliptic cross-section as shown in Figure 6.6(a) we find using Allen-Cahn dynamics 6.9 that the final static form of the column cross section is indeed circular as shown in Figure 6.6(b).

6.6.2 Gravitational field

Using a regular grid with spacing $h = 0.1$ we find the static form of an initially circular column subject to a homogeneous gravitational field.

Starting with an circular profile with radius 3m we solve the discrete Allen-Cahn equation (6.46) and 6.49 on a 150 by 150 square grid using a time step size

$\Delta t = 5 \cdot 10^{-3}$. We consider that the static form is found when the magnitude of $\frac{\partial \psi}{\partial t}$ is less than 10^{-5} over the entire grid.

We consider two cases. In both the phase-field parameters $\alpha = 1$ and $\beta = 30$ give estimates of surface tension and interface width (see expressions 6.18 and 6.17) $\kappa = 10.4$ and $\delta_\psi = 0.26$.

In Figure 6.7(a) and 6.7(b) we take fluid density $\rho = 0.45$ and $\rho = 0.9$. We compare the cross-section found using the phase field in black with that found using the Young-Laplace equation (6.5) in red. As ψ varies between 1 and -1 we take the contour $\psi = 0$ as the interface in the phase-field model. We see that the two compare well with the Young-Laplace equation giving a slightly flatter shallower form for the column cross-section.

6.6.3 Parallel magnetic field

Considering a magnetic field which is parallel and uniform far from the liquid column, Shercliff (Shercliff [1981]) found that the form of the cross-section is approximately elliptic. Using a similar field configuration we calculate the equilibrium shape of a liquid column submitted to a magnetic field which is parallel far from the column. Starting with a circular column of radius 2m, we solve the Allen-Cahn equation (6.46) and the field equations (6.44) and (6.45). We use a square 400 by 400 grid whose length and height are 40m giving a grid spacing $h = 0.1$. We use time step size $\Delta t = 4 \cdot 10^{-3}$s. As before we consider that the static form is found when $\frac{\partial \psi}{\partial t}$ is less than 10^{-5} over the entire grid.

We impose a constant parallel field $\mathbf{B}_0$ say on the upper and lower boundaries, and take the field to be normal to the left and right boundaries. In Figure 6.8 we show the static form obtained using $|\mathbf{B}| = 1.5 \cdot 10^{-3}$T and in Figure 6.9 we used $|\mathbf{B}| = 1.5 \cdot 10^{-3}$T. In both cases we use the same phase-field parameters as before i.e $\alpha = 1$ and $\beta = 30$.

Shercliff predicts for $|\mathbf{B}| = 1.5 \cdot 10^{-3}$T, that the column profile will be ap-

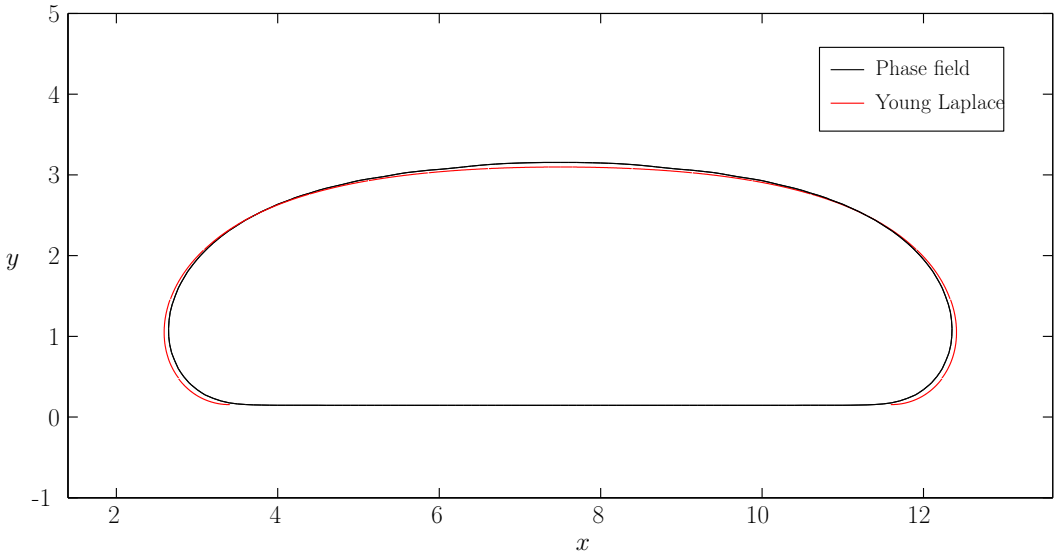

(a) Cross-section of a liquid column resting on a substrate at $y = 0$ subject to gravitation and surface tension. The surface tension parameter $\kappa = 10.4\mathrm{N\,m^{-}1}$ and density $\rho = 0.45\mathrm{kg\,m^{-3}}$.

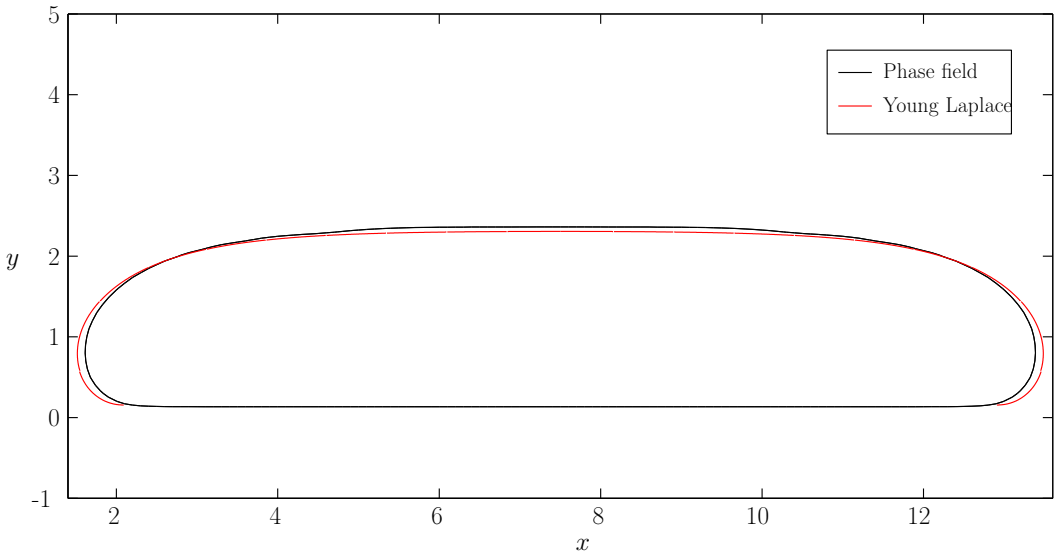

(b) Cross-section of a liquid column resting on a substrate at $y = 0$ subject to gravitation and surface tension. The surface tension parameter $\kappa = 10.4\mathrm{N\,m^{-}1}$ and density $\rho = 9\mathrm{kg\,m^{-3}}$.

Figure 6.7: Cross-sections of a liquid column resting on a substrate at $y = 0$ subject to gravitation and surface tension for 2 different values of ρ. The phase-field solution in black is compared with the solution obtained from the Young-Laplace equation in red.

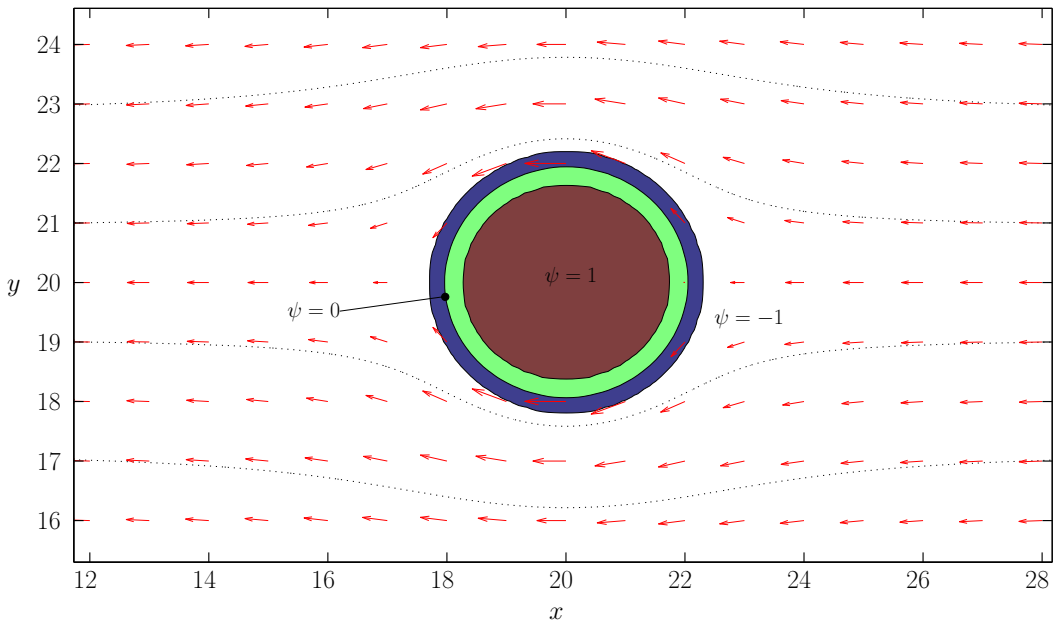

Figure 6.8: Static shape obtained of conductor in a parallel far field. The red arrows plot the direction of the magnetic field. The dotted lines are streamlines corresponding to ξ = constant. Using Allen-Cahn dynamics we find the equilibrium shape of an initial circular conductor of radius 2m. The far field strength is $B_0 = 1.5\text{mT}$, conductivity $\sigma = 50\mho$ and surface tension $\kappa = 10.4\text{N}\,\text{m}^{-}1$.

proximately elliptic with eccentricity $e = 0.92$. Taking the $\psi = 0$ contour as the fluid boundary as before, we measure $e = 0.95$. In the $|\mathbf{B}| = 3 \cdot 10^{-3}\text{T}$, Shercliff predicts $e = 0.77$ and we measure $e = 0.70$.

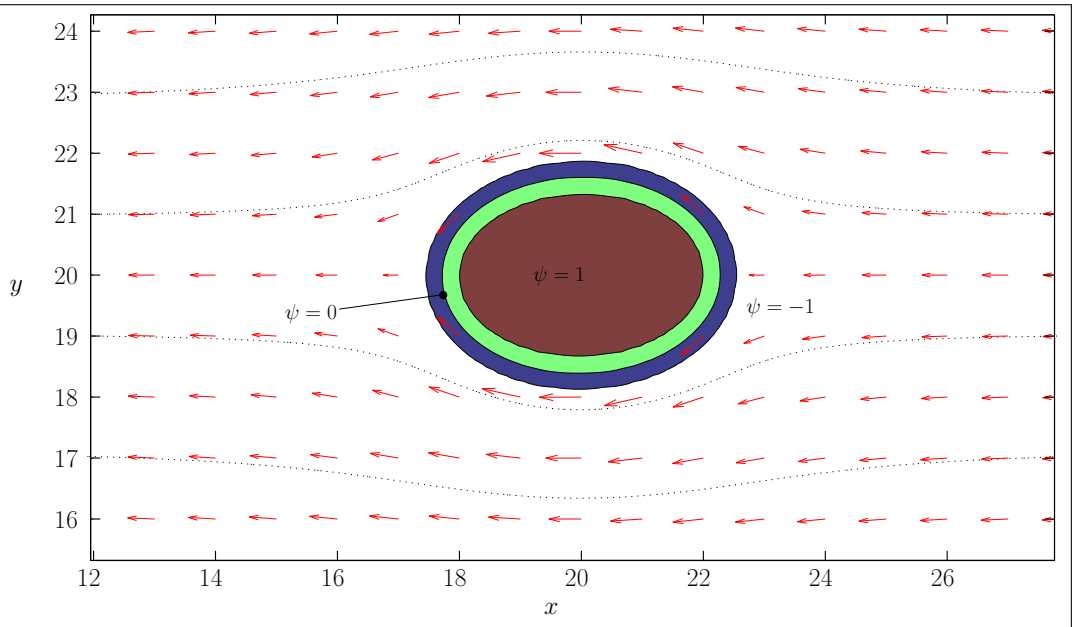

Figure 6.9: Static shape obtained of conductor in a parallel far field. The red arrows plot the direction of the magnetic field. The dotted lines are streamlines corresponding to ξ = constant. Using Allen-Cahn dynamics we find the equilibrium shape of an initial circular conductor of radius 2m. The far field strength is $B_0 = 3\text{mT}$, conductivity $\sigma = 50\mho$ and surface tension $\kappa = 10.4\text{N}\,\text{m}^{-}1$.

6.7 Discussion

We have conducted a preliminary investigation of the use of a novel phase-field method in modelling coupled MHD and free-surface problems.

Concerning the problem of an infinite drop resting on a substrate in a uniform vertical gravitational field, we obtain good agreement with the classic Young-Laplace equation. Modelling a simple field geometry, we obtain results which are in reasonable agreement with Shercliff's analytical results. In general our method produced columns which are more elliptic than Shercliff's but this may be due to the limitations of the numerical finite difference scheme used. Shercliff considers an ideal case where the field is parallel far from the column. This is not really possible with our method, and the closest we can achieve is to have the field parallel on the edges of our computational domain. This will tend to squeeze the field lines together and thus will increase the magnetic pressure on the column resulting in a more elliptic cross-section.

We conclude that further investigation of this method is warranted, particularly the inclusion of fluid flow and extension to 3 dimensions. Our investigation has been somewhat limited by the simple finite difference approach used, namely uniform grid spacing. This limits the size of the computational domain which can be used due to memory constraints. We expect that more sophisticated numerical schemes will improve the speed and flexibility of this method.

Chapter 7

Conclusions

Complicated free surface behaviour is observed in many applications of liquid-metal MHD. Examples include, levitation, cold crucible processing, continuous casting and semi-levitation. The coupled MHD free-surface physics may give rise to instabilities which cause unwanted deformation of the free surface. This in turn limits the efficiency of these processes.

The magnetic field and the free surface geometry of these processes is often complicated and difficult to model. It is thus of interest to study problems whose geometry is simple but which exhibit the complicated behaviour observed in industrial processes.

In this thesis we have investigated a number of problems involving the effect of an AC magnetic field on the free-surface of liquid metals in industrial MHD. In particular in Chapter 2 we developed a Lagrangian MHD theory to model the stability of free-surface azimuthal modes on the perimeter of a circular pool of liquid metal. These modes are observed in the so called "starfish" experiment (see Etay et al. [2003]), in which a circular pool is submitted to a low-frequency magnetic field.

We extended this theory in Chapters 3 and 4 to consider the effect of geometry by examining the behaviour of the free-surface of an elongated "strip-like" pool when it is submitted to a low-frequency magnetic field. In Chapter 3 we have investigated the "strip" problem experimentally. We observed behaviour similar to the "starfish" experiment–in particular the transverse modes we observe behave somewhat like the "starfish" azimuthal modes. In Chapter 4 we analysed the stability of these transverse modes by extending the Lagrangian theory developed in Chapter 2 to this new geometry.

In Chapter 5 we examined the effect of increasing the magnetic field frequency. In contrast to the low-frequency magnetic fields examined previously, we experimentally investigated the effect of higher frequencies on a circular pool of liquid metal. We observed more complicated behaviour than the "starfish" experiment. Since the physics of this problem are significantly more

complicated than the "starfish" and "strip" problems, a description in terms of our previous Lagrangian theory is not possible.

In Chapter 6 we investigated a prospective "phase field" method for modelling the effect of a high-frequency magnetic field on the free-surface of a conductor. Two simple two dimensional problems were initially examined. We obtained numerical solutions which compare well with previous analytic solutions (Paddey [1969] and Shercliff [1981]). The first problem we considered was the equilibrium shape of a strip of liquid metal resting on a substrate subject to a uniform gravitational field; the second was the equilibrium shape of a liquid metal column subject to a high-frequency magnetic field whose field lines are parallel far from the column.

Turning again the the theory of the "starfish" problem (Chapter 2), the stability diagram we obtain from our theory for the "starfish" shares a number of important features with the experimental stability diagram. In particular both have a similar vee shape structure, which is consistent with a Mathieu-type subharmonic instability. Our theory confirms that this is the underlying mechanism which governs the azimuthal "starfish" modes. We observed similar behaviour in the "strip" experiment. Aside from complicated mode coupling not observed in the "starfish" experiment, the experimental stability diagram we obtained for the transverse "strip" modes shares the same vee shape structure as the "starfish". Our theory confirmed that the underlying mechanism is the same as in the "starfish", i.e. a Mathieu-type subharmonic instability. Unfortunately our theory does not take mode interaction into account. One suggestion for further work in this area is that this effect could be taken into account by extending our theory to consider a Fourier series on the pool edge instead of an isolated Fourier mode.

As the magnetic-field frequency is increased the pool behaviour becomes more complicated. At medium frequencies we observed more complicated behaviour than the in the "starfish" experiment, but there does appear to be some systematic structure to the pool behaviour. In particular the pool perimeter

is deformed into regular elliptic, triangular and square shapes.

We examined the effect of a high-frequency magnetic field in our preliminary investigation of the "phase field" method. This method seems to be a promising method for problems such as magnetic levitation and cold crucible processing where large free-surface deformations are observed. We suggest that our basic method be extended to three dimensions and include fluid flow so these types of problems may be modelled.

Appendix A

Ingwiller's experimental results

As the experimental work of Ing has not been widely published we summarise his results here.

Considering a larger range of magnetic field frequencies, Ingwiller examines the same phenomena observed by Daugan, and uses his experimental method with a few changes. Instead of Mercury he uses an alloy of Gallium, Ga-In-Sn in the following proportions by mass: 67% Ga, 20.5% In and 12.5% Sn. This eutectic is a liquid at room temperature as its melting point is 10.5°C. In addition, this liquid metal does not have the toxic properties of mercury, or its low vapour pressure, which makes it easier to handle. However, this eutectic is more prone to oxidation than mercury, a surface exposed to air will completely oxidise almost instantaneously. Ingwiller avoids this by submerging his pool in a solution of HCl and ethyl alcohol. The use of ethyl alcohol necessitates a change of material used for the concave substrate on which the pool rests. Daugan used a plexiglass substrate: ethyl alcohol attacks plexiglass causing any surfaces exposed to crack, thus Ingwiller uses a PVC substrate instead.

Similarly to Daugan, Ingwiller observes the formation of the "starfish" azimuthal waves. Using the same experimental protocol as Daugan, he obtains the stability diagram given in Figure A.1.

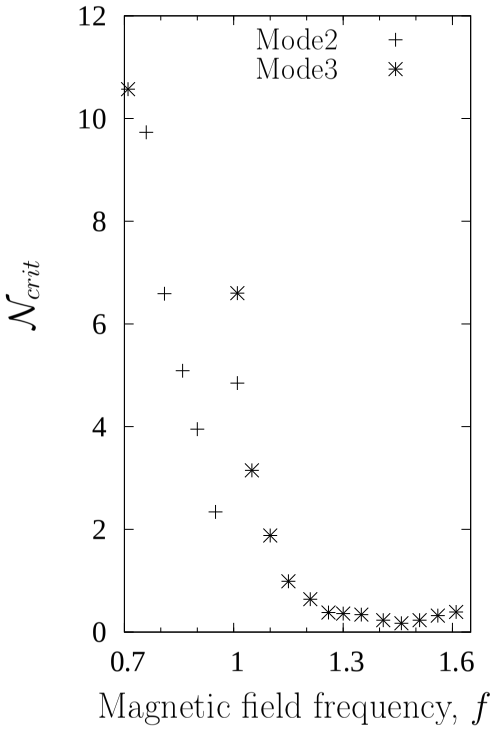

(a) Modes two and three of Ingwiller's experimental stability diagram; these are presented separately due to the larger variation of the critical value of the magnetic interaction parameter $\mathcal{N}_{crit}$ observed.

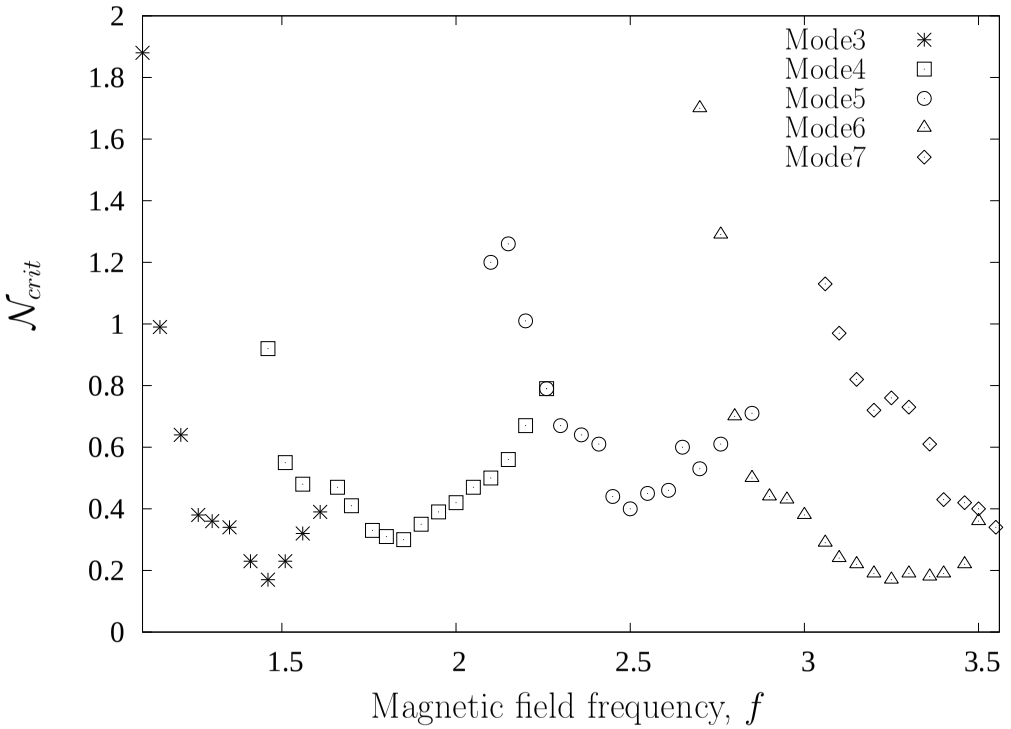

(b) Modes three to seven of Ingwiller's experimental stability diagram.

Figure A.1: The experimental stability diagram of the azimuthal waves observed by Ingwiller on the edge of a pool of Ga-In-Sn of radius 3cm resting on a concave substrate and which are excited by a low-frequency vertical homogeneous magnetic field. The critical value of the magnetic interaction parameter $\mathcal{N}$ is plotted against the frequency f of the exciting magnetic field.

Appendix B

Matlab codes used for processing the experimental footage obtained in the strip experiment

In Chapter 3 we gave a summary of the image processing algorithm that we used to calculate the wavelength λ of the various transverse modes observed.

In this appendix we provide the commented Matlab source code of the algorithms used. The processing is performed by two separate codes. The first takes an avi file containing a video of a transverse mode. This code produces a preprocessed film which is then used by another code - four.m which calculates the wavelength of the transverse mode.

Finally the code four.m calls a function fitsine.m which estimates the wavelength λ of the transverse mode on the pool edge by fitting a sine wave to it.

B.1 Preprocessing of experimental results - "strip-preprocessing.m"

```
%Filename of the experimental footage to be preprocessed.
filename='mode37_1.7hz_34v_c.avi'
pathname='/media/MP3s/film/24.07.2007/'

%Open the video file using MplayerMEX
%(http://cs-people.bu.edu/tvashwin/mplayerMex/)
[av_hdl, av_inf] = mplayerOpen([pathname, filename]);
%get fps of video
fps=av_inf.fps;
%calculate period between subsequent frames
p_frame=1/fps;
% frequency of magnetic field used in experiment
freq=1.7;
% calculte the period of oscillation of the field
period=1/freq;
% number of frames to used to calculate an average
% shape - r_b_sum of the pool
n_frame=ceil(10*period/p_frame)
% define sobel operator
```

```
s=  [1  2  1; 0  0  0; -1 -2 -1];
r_b_sum=0

% make sure that the film is not empty
if length(av_hdl) > 0;

    % read in all the frames from the video one at a time
    % procesing each one in turn
    for frame_num = 1:av_inf.NumFrames;

        %Reads frame frame_num from the video
        pixmap = mplayerReadMex(av_hdl, 1);

        % transforms the fram data into an
        % image format that is easier to manimulate
        im=reshape(pixmap/255,[av_inf.Height,av_inf.Width,3]);

        % calculate an image of the ratio of red to blue
        % in the image
            r_b=(im(:,:,1)+1e-12)./(im(:,:,2)+1e-12);

            % keep adding frames to r_b_sum for 10 periods
            % of  magnetic field oscillation
             if(frame_num <= n_frame)
                 r_b_sum=r_b_sum+(r_b/(sum(r_b(:))/av_inf.Height/...
                     av_inf.Width));
             end

             % rescale r_b (scale factor found by trial and error...
                 )
             tmp=r_b/3;

             % detect edges in the image of the pool using canny ...
                 edge
             %detection
             ed=edge(medfilt2((tmp<0.905)*1,[12,12]),'canny'...
                 ,0.8,4);
```

```
% sometime the detected pool edges have small holes ...
    in them
% this code takes care of that
ed2_1=conv2(double(ed),s');
ed2_2=conv2(double(ed),s);
ed2_tmp=(ed2_2.^2 + ed2_1.^2)>=1;
ed2=ed2_tmp(1:av_inf.Height,1:av_inf.Width);

% write an copy of the unprocessed frame to file
imwrite(im,'orig.png');

%find midpoint of the frame
w_mp=floor((av_inf.Width)/2);

%find a point on the pool edge
h_mp=min(ed2(:,w_mp).*linspace(-(av_inf.Height)...
    /2+1,(av_inf.Height)/2,(av_inf.Height))')+av_inf....
    Height/2;

%select pool edge
bw2=bwselect(ed2,w_mp,h_mp);

% fill pool edge to give a solid white pool on a ...
    black
% background
filled=imfill(bw2,4,'holes');

% write this image to a file
imwrite(filled,'filled.png')


%use linux utility imagemagik to create a montage
% of the origional image and the processed image
% ie create new image consisting of the processed
% image beside the original frame
filename=[int2str(frame_num),'.tga']
```

```
        cmd=['! montage filled.png orig.png -geometry +0+0 '...
            ,filename];
        eval(cmd)
        cmd=['! echo ',filename,' >>list.txt'];
        eval(cmd)
end


        %Cleanup - close video file
        mplayerCloseMex(av_hdl);

        % the floowing code calculates and saves to file av....
            png a
        % average shape of the pool. This is used in the ...
            second
        % code to caculate the pool wavelength
        r_b_sum=r_b_sum/n_frame;
        bw=edge(r_b_sum.*(r_b_sum<0.9),'canny',0.1,20);
        ed2_1=conv2(double(bw),s');
        ed2_2=conv2(double(bw),s);
        ed2_tmp=(ed2_2.^2 + ed2_1.^2)>=1;
        ed2=ed2_tmp(1:av_inf.Height,1:av_inf.Width);
        w_mp=floor((av_inf.Width)/2);
        h_mp=min(ed2(:,w_mp).*linspace(-(av_inf.Height)...
            /2+1,(av_inf.Height)/2,(av_inf.Height))')+av_inf....
            Height/2;
        bw2=bwselect(ed2,w_mp,h_mp);
        bw3=imfill(bw2,4,'holes');
        imwrite(bw3,'av.png')



        % Call linux utility mencoder (part of mplayer
        % http://www.mplayerhq.hu) to combine the processed ...
            frames into
        % one film called processed.avi
        cmd=['! mencoder  mf://@list.txt  -mf fps=',num2str(...
            fps),' -ovc lavc -lavcopts vcodec=ffv1 -o ...
            processed.avi']
```

```
        eval(cmd)

        % now that we have combined the frames into a video,...
            we can
        % delete the images of the frames
        eval('!rm␣*.tga')
end
```

B.2 Calcualtion of transverse mode wavelength λ - "four.m"

```
% code reads in the video processed.avi which
% contains preprocessed experimental footage.
% It then measures the wavelength of the transverse
% mode using a variety of methods.
% results are save to a text file wl.txt

% read in image of average pool shape
avg=imread('av.png');

% open the video (processed.avi) of processed experimental ...
    footage
% using mplayerMex
filename='processed.avi'
pathname='./'
[av_hdl, av_inf] = mplayerOpen([pathname, filename]);

% get the fps of the video
fps=av_inf.fps;
% calcualte the time period
% between sucessive frames
p_frame=1/fps;

% set the frequency of the magnetic field used in
% the experiment
freq_manip=1.7;
```

```
% calculate the period of oscillation of the
% magnetic field
period=1/freq_manip;

% open a figure window
fig=figure;

% turn doublebuffer on to improve display of results in
% the figure window
set(fig,'DoubleBuffer','on');

% caulcualte various properties of the average pool shape,
% the centroid is the most imortant for this code
STATS = regionprops(bwlabel(avg),'Perimeter','Area','Orientation...
    ','Centroid');

% vector y and matrix xmask are used later to remove
% the half of the pool shape (we only use the upper half)
y=linspace(-(av_inf.Height)+STATS.Centroid(2),(av_inf.Height)-...
    STATS.Centroid(2),av_inf.Height)';
xmask=repmat(y,1,av_inf.Width/2);

%IMPORTANT
%ratio is the ratio of pixels to actual length
% i.e. the number of pixels per millimeter.
ratio=7.7078

% loop over the entire video and process each frame
% in turn
    for frame_num = 1:av_inf.NumFrames;

                        %Reads frame number frame_num from the ...
                            video
                        pixmap = mplayerReadMex(av_hdl, 1);
            %transform into a more convienient image format
            im=reshape(pixmap/255,[av_inf.Height,av_inf.Width...
                ,3]);
```

```
% we are only interested in the preprocessed image
%so we discard the orignal image (which in the
% right half of the frame)
imorig=im(1:av_inf.Height,av_inf.Width/2:av_inf....
    Width-1);
imbw=im2bw(im(1:av_inf.Height,1:av_inf.Width/2));

% extract the upper half of pool contour
wave=max(imbw.*xmask);
tmp=size(wave);
N=tmp(2);
lengthvec=linspace(0,1/(ratio/N),N);
% store the pool contour curve in a matrix
wave_mtrx(frame_num,:)=wave/ratio;

% this code plots the contour of the pool
% as we extract it from the
% video
if(frame_num < 2)
   wplot=plot(lengthvec,wave/ratio,'k','erasemode','...
       xor');
   xlim([0,150]);
   set(wplot,'LineWidth',4);
   set(gca,'FontSize',20);

   ylabel('Y (mm)','FontSize',20);
   xlabel('X (mm)','FontSize',20);
   hold
else
   set(wplot,'xdata',lengthvec,'ydata',wave/ratio)
    set(gca,'FontSize',20);

   ylabel('Y (mm)','FontSize',20);
   xlabel('X (mm)','FontSize',20);
```

```
end
drawnow

end
 time=frame_num/fps

 % matrix wave_mtrx(i,j) contains a
 % the contours of the transverse waves
 % traced from the preprocessed video.
 % The contour from frame i say is
 % stored as a vector in wave_mtrx(i,:).

 % Here we filter our results store in wave_mtrx
 % by taking  a fft in time of all the traced ...
     transverse
 % wave contours and only keeping the spectrum which
 % has frequency close to the magnetic field ...
     frequency.
 % Doing this keeps the information pertanant to the...
      transverse
 % wave (which oscillates at the field frequency) ...
     while
 % discarding everhthing else
 freq2=[0:frame_num/2-1]./time;
 fft_mtrx=(fft(wave_mtrx));
 t_point=round(max(((freq2-freq_manip).^2 <=min((...
     freq2-freq_manip).^2)).*linspace(1,frame_num/2,...
     frame_num/2)) );
 pspec=sum(((abs(fft_mtrx(2:floor(frame_num/2),:)')...
     .^2)))/N;
 fpspec=freq2(2:end);
 pspecmtrx=([fpspec',pspec']);
 save fmanip.txt freq_manip -ASCII
 save pspecmtrx.txt pspecmtrx -ASCII
mask=zeros(size(fft_mtrx));
mask(t_point-3:t_point+3,:)=1;
```

```
    % after having filtered our fft spectrum we invert ...
        the
    % result.
    invfft=ifft(fft_mtrx.*mask);
    clear mask fft_mtrx wave_mtrx
    hold off

    % We now loop over the filtered results and estiamte
    % the wavelength of the transverse mode in each ...
        frame
    % by fitting a variety of functions to the
    % filtered contour
for frame_num = 1:av_inf.NumFrames;
    % get the filtered contour from the filtered results
    wave=real(invfft(frame_num,:));

    % fit 3 different functions to the filtered contour
    % fitsoln= a fitted sine wave
    % linfit= a fitted strait line
    % psfit= a fitted polynomial and sine combination
    % of the form : p1*x^2 + p2*x + p3 + a1*sin(b1*x+c1)...
        .
    % Goodness of fit parameters of the sine fit are ...
        given in gf
    % while the goodness of fit paramters of the sine/...
        polynomal
    % combination are given in gf2.
    [fitsoln,xd,wave3,wave4,gf,linfit,psfit,gf2]=fitsine...
        (wave,ratio);


    % Plot the fitted functions
    if(frame_num < 2)
      wplot=plot(xd,wave3,'k','erasemode','xor')
      hold
      fplot=plot(xd,fitsoln(xd),'b','erasemode','xor')
      linplot=plot(xd,linfit(xd),'g','erasemode','xor')
```

```
    mxplot=plot(xd,psfit(xd),'y','erasemode','xor')

    set(wplot,'LineWidth',4);
    set(fplot,'LineWidth',4);
    set(linplot,'LineWidth',4);
    set(mxplot,'LineWidth',4);
    set(gca,'FontSize',20);



    ylabel('Y (mm)','FontSize',20);
    xlabel('X (mm)','FontSize',20);


else
    set(wplot,'xdata',xd,'ydata',wave3)
    set(fplot,'xdata',xd,'ydata',fitsoln(xd))
    set(linplot,'xdata',xd,'ydata',linfit(xd))

    set(mxplot,'xdata',xd,'ydata',psfit(xd))


    set(gca,'FontSize',20);



    ylabel('Y (mm)','FontSize',20);
    xlabel('X (mm)','FontSize',20);


end
drawnow


% Store the estimates of wavelength
```

```
    % obtained from the various fitted funtions
    % in matricies.
    %
    % Matrix lam1 stores the estimates obtained
    % using the sine fit.
    lam1(frame_num)=2*pi/fitsoln.b1;
    magnitude1(frame_num)=fitsoln.a1;
    phase1(frame_num)=fitsoln.c1;
    gof1(frame_num)=gf;
    rsq(frame_num)=gf.rsquare;
    rmse(frame_num)=gf.rmse;

    % Matrix lam2 stores the estimates obtained
    % using the sine+polynomial function fit.
     lam2(frame_num)=2*pi/psfit.b1;
     magnitude2(frame_num)=psfit.a1;
     phase2(frame_num)=psfit.c1;
     gof2(frame_num)=gf2;
     rsq2(frame_num)=gf2.rsquare;
     rmse2(frame_num)=gf2.rmse;

end

%After having computed the estimates
%of the wavelenght of the transverse mode
%in each frame, we bin the results in a histogram.
%The bin are 1mm wide

%We start with the wavelengths estiamed
%using a sine fit
binsize=1
l_lam=floor(min(lam1))-5;
u_lam=ceil(max(lam1))+5;
nbins=(u_lam-l_lam)/binsize;
bins=linspace(l_lam,u_lam,nbins+1)-0.5;
nb=hist(lam1,bins);
```

```
% find the bin with highest frequency
% and take the vaule of this bin
% as the wavelength of the transverse mode
[mx, pos]=max(nb);
wl=bins(pos);



rfact=10;
lp=122


wnt=round((lp*2/wl)*rfact)/rfact;
rsqnorm=sum(rsq)/sum(rsq > -1);

rsqnorm_min=min(rsq)
rsqnorm_max=max(rsq)

%We then continue with the wavelengths estiamed
%using a sine+poly fit
l_lam=floor(min(lam2))-5;
u_lam=ceil(max(lam2))+5;
nbins=(u_lam-l_lam)/binsize;
bins=linspace(l_lam,u_lam,nbins+1)-0.5;
nb=hist(lam2,bins);
[mx, pos]=max(nb);
wl2=bins(pos);
wnt2=round((lp*2/wl2)*rfact)/rfact;

rsqnorm2=sum(rsq2)/sum(rsq > -1);
rsqnorm2_min=min(rsq2)
rsqnorm2_max=max(rsq2)

% finally we write our resuts to a text file
fid=fopen('wl.txt','w+')
fprintf(fid,'sine model\n');
fprintf(fid, '%6.2f\n',wl);
```

```
fprintf(fid, '%6.2f\n',wnt);
fprintf(fid, '%6.2f\n',rsqnorm);
fprintf(fid, '%6.2f\n',rsqnorm_min);
fprintf(fid, '%6.2f\n',rsqnorm_max);
fprintf(fid,'poly + sine model\n');
fprintf(fid, '%6.2f\n',wl2);
fprintf(fid, '%6.2f\n',wnt2);
fprintf(fid, '%6.2f\n',rsqnorm2);
fprintf(fid, '%6.2f\n',rsqnorm2_min);
fprintf(fid, '%6.2f\n',rsqnorm2_max);

fclose(fid)
```

B.3 Fitting of functions to pool contour to calculate λ - "fitsine.m"

```
%Fits 3 different functions to a vector of data points called ...
    wave
%fitsoln = a fitted sine
%cftmp = a fitted strait line
%cftmp2 = a fitted sine + polynomial of the form:
%p1*x^2 + p2*x + p3 + a1*sin(b1*x+c1)
function [fitsoln,xd,wav,wav2,gf,cftmp,cfmtmp2,gf2]=fitsine(wave...
    ,ratio)

% We chop then end of wave off to take care
% of the end effect on the geometry of the pool.
deltal=300;
deltar=300;
lb=deltal;
rb=deltar;
tmp=size(wave);
N=tmp(2) -deltal -deltar+1;
wave2=wave(deltal:end-deltar);
size(wave2);
```

```
xdat=linspace(1,N,N)/ratio;
xd=xdat;

dat(:,1)=xdat;
dat(:,2)=wave2;

% now we try to remove any constant factor
% from the data
cste=sum(wave2)/N
wave3=wave2-cste;

% now we fit a strait line
cftmp=fit(xdat',wave3','poly2')
wave4=wave3-cftmp(xdat)';

% now we fit a sin fuction
[cfun,gof] = fit(xdat',wave3','sin1');
wav=wave3;
wav2=wave4;
gf=gof;
fitsoln=cfun

% here we fit a sin + polynominal funciton of the form:
%p1*x^2 + p2*x + p3 + a1*sin(b1*x+c1)
opts=fitoptions('Method','NonlinearLeastSquares','Startpoint',[...
    cfun.a1,cfun.b1,cfun.c1,cftmp.p1,cftmp.p2,cftmp.p3]);
polysin=fittype('p1*x^2 + p2*x + p3 + a1*sin(b1*x+c1)','options'...
    ,opts);
[cfmtmp2,gf2]=fit(xdat',wave3',polysin)
```

References

SM Allen and JW Cahn. A microscope theory for antiphase boundary motion and its application to antiphase domain coarsening. *Acta Metall.*, 27(6): 1085–1095, 1979.

G. K. Batchelor. *An Introduction to Fluid Dynamics*. Cambridge University Press, February 1967. ISBN 0521663962.

J Canny. A computational approach to edge detection. *IEEE Trans. Pattern Anal. Mach. Intell.*, 8(6):679–698, 1986. ISSN 0162-8828.

L. Collatz and PG Williams. *The Numerical Treatment of Differential Equations*. Springer Berlin, 1960.

M. Conrath and C. Karcher. Shaping of sessile liquid metal drops using high-frequency magnetic fields. *European Journal of Mechanics B/Fluids*, 24: 149–165, 2005.

P.A. Davidson. *An Introduction to Magnetohydrodynamics*. Cambridge, 2001.

F. Debray and Y. Fautrelle. Free surface deformation frequencies of an electromagnetically excited mercury layer. *Experiments in Fluids*, 16(5):316–322, 1994.

Q. Du, C. Liu, R. Ryham, and X. Wang. A phase field formulation of the Willmore problem. *Nonlinearity*, 18(3):1249–1267, 2005.

S. Dufour and G. Vinsard. Search algorithm for free boundary of thin liquid conducting domains. *Magnetics, IEEE Transactions on*, 43(4):1417–1420, 2007.

J. Etay. Formage et guidage des metaux liquides sous l'action de champs magnetiques alternatifs. *Report de DEA de Mécanique des Fluides, Inst. Natn. Polytechnique, Grenoble*, 1980.

J. Etay, Y. Fautrelle, and A.D. Sneyd. The starfish experiment: a Lagrangian approach. *Magnitnaya Gidrodinamika*, 39(3):271–278, 2003.

Y. Fautrelle and A.D. Sneyd. Surface waves created by low-frequency magnetic fields. *European Journal of Mechanics B - Fluids.*, 24:91–112, 2005.

Y. Fautrelle, D. Perrier, and J. Etay. Free surface controlled by magnetic fields. *ISIJ International*, 43(6):801–806, 2003.

Y. Fautrelle, J. Etay, and S. Daugan. Free-surface horizontal waves generated by low-frequency alternating magnetic fields. *J. Fluid Mech.*, 527:285–301, 2005.

T.P. Felici. On the surface stability of liquid conductors in electromagnetic shaping. *Journal of Fluid Mechanics*, 302:1–28, 1995.

A. Gagnoud, J. Etay, and M. Garnier. Le problème de frontière libre en lévitation électromagnétique. *Journal de Mécanique Théorique et Appliquée*, 5(6):911–934, 1986.

J.M. Galpin and Y. Fautrelle. Liquid-metal flows induced by low-frequency alternating magnetic fields. *J. Fluid Mech.*, 239:383–408, 1992.

J.M. Galpin, Y. Fautrelle, and A.D. Sneyd. Parametric resonance in low-frequency magnetic stirring. *J. Fluid Mech.*, 239:409–427, 1992.

M. Hinaje, G. Vinsard, and S. Dufour. Analytical modelling of a thin liquid metal layer submitted to an ac magnetic field. *Journal of Physics-London-D Applied Physics*, 39(13):2641, 2006a.

M. Hinaje, G. Vinsard, and S. Dufour. A computation and a use of the magnetic energy in a thin liquid metal submitted to an ac magnetic field. *Magnetics, IEEE Transactions on*, 42(4):1059–1062, 2006b.

M. Hinaje, G. Vinsard, and S. Dufour. Determination of stable shapes of a thin liquid metal layer using a boundary integral method. *Journal of Physics-London-D Applied Physics*, 39(6):1244, 2006c.

Melika Hinaje. *modelisation de l'action d'un champ electromagnetique variable sur un metal liquide dispose en nappe peu epaisse.* PhD thesis, L'Institut National Polytechnique de Lorraine, 2 avenue de la Forêt de Haye - BP 3 - F-54501 Vandoeuvre - France, 2005.

CW Hirt and BD Nichols. Volume of fluid/VOF/ method for the dynamics of free boundaries. *Journal of Computational Physics*, 39:201–225, 1981.

T. Huang, G. Yang, and G. Tang. A fast two-dimensional median filtering algorithm. *Acoustics, Speech, and Signal Processing [see also IEEE Transactions on Signal Processing], IEEE Transactions on*, 27(1):13–18, 1979.

F Ingwiller. Instabilités paramétriques electromagnétiques en couche mince utisation d'un alliage ga-in-sn, September 2000. Stage effectué au laboratoire EPM.

F. Ingwiller, F. Bonnel, Y. Fautrelle, S. Daugan, and J. Etay. Dynamique d'une goutte de métal liquide soumise à un champ magnétique alternatif. In *Actes du 9ème Colloque Francophone FLUVISU 2001*, pages 18–21, 2001.

D. Jacqmin. Calculation of two-phase navier-stokes flows using phase-field modeling. *Journal of Computational Physics*, 155(1):96–127, 1999.

AJ Mestel. Magnetic levitation of liquid metals. *Journal of Fluid Mechanics*, 117:27–43, 1982.

John Miles. On surface waves with zero contact angle. *Journal of Fluid Mechanics*, 245:485–492, 2006. doi: 10.1017/S0022112092000557. URL `http://journals.cambridge.org/action/displayAbstract?fromPage=online&aid=381003&fulltextType=RA&fileId=S0022112092000557`.

R.J. Moreau. *Magnetohydrodynamics*. Springer, 1990.

O. Muck. German patent 422004, Oct 1923.

EC Okress, DM Wroughton, G. Comenetz, PH Brace, and Kelly JCR. Electromagnetic levitation of solid molton. melts. *J. Appl. Phys*, 23(5):525–529, 1952.

J. F. Paddey. *Surface and Colloid Sciences*, volume 1. J. Wiley., 1969.

M. Patra and M. Karttunen. Stencils with isotropic discretization error for differential operators. *Numerical Methods for Partial Differential equations*, 22(4):936, 2006.

D. Perrier. *Mise en oeuvre et caractérisation d'un nouveau procédé électromagnétique destiné à favoriser les transferts de masse aux interfaces entre un métal liquide et un sel fondu.* PhD thesis, INPG, 46, avenue Félix Viallet - 38031 Grenoble Cedex 1 - France, 2002.

S. Popinet and S. Zaleski. A front-tracking algorithm for accurate representation of surface tension. *International Journal for Numerical Methods in Fluids*, 30(6):775–793, 1999.

William H. Press, Saul A. Teukolsky, William T. Vetterling, and Brian P. Flannery. *Numerical Recipes in FORTRAN (2nd ed.): the art of scientific computing.* Cambridge University Press, New York, NY, USA, 1992. ISBN 0-521-43064-X.

J. Priede and G. Gerbeth. Spin-up instability of electromagnetically levitated spherical bodies. *Magnetics, IEEE Transactions on*, 36(1):349–353, 2000a.

J. Priede and G. Gerbeth. Oscillatory instability of electromagnetically levitated solid bodies. *Magnetics, IEEE Transactions on*, 36(1):354–357, 2000b.

J. Priede and G. Gerbeth. Stability of an electromagnetically levitated spherical sample in a set of coaxial circular loops. *Magnetics, IEEE Transactions on*, 41(6):2089–2101, 2005.

J. Priede and G. Gerbeth. Stability analysis of an electromagnetically levitated sphere. *Journal of Applied Physics*, 100:054911, 2006.

J. Priede, J. Etay, and Y. Fautrelle. Edge pinch instability of liquid metal sheet in a transverse high-frequency ac magnetic field. *Physical Review E*, 73(6):66303, 2006.

Y. Fautrelle S. Daugan and J. Etay. Free surface horizontal waves generated by low frequency alternating Magnetic Fields. In *TMS Symposium on "Fluid-Flow Phenomena in Metals Processing"*, pages 41 – 48, 1999.

GH Schippereit, AF Leatherman, and D. Evers. Cold crucible induction melting of reactive metals. *J. Metals*, 13:140, 1961.

J.A. Sethian. *Level set methods and fast marching methods: evolving interfaces in computational geometry, fluid mechanics, computer vision, and materials science*. Cambridge University Press, 1999.

J. A. Shercliff. Magnetic shaping of molten metal columns. *Proceedings of the Royal Society of London. Series A, Mathematical and Physical Sciences*, 375(1763):455–473, 1981. ISSN 00804630. URL `http://www.jstor.org/stable/2990333`.

AD Sneyd. Fluid flow induced by a rapidly alternating or rotating magnetic field. *Journal of Fluid Mechanics*, 92(01):35–51, 1979.

AD Sneyd and HK Moffatt. Fluid dynamical aspects of the levitation-melting process. *Journal of Fluid Mechanics*, 117:45–70, 1982.